CONFINEMENT EFFECT ON SEMICODUCTOR NANOWIRES PROPERTIES

A Thesis
Presented to
The Academic Faculty

by

Alexis Nduwimana

In Partial Fulfillment
of the Requirements for the Degree
Doctor of Philosophy in the
School of Physics

Georgia Institute of Technology
December 2007

CONFINEMENT EFFECT ON SEMICODUCTOR NANOWIRES PROPERTIES

Approved by:

Professor Mei-Yin Chou, Advisor
School of Physics
Georgia Institute of Technology

Xiao-Qian Wang
School of Art and Sciences
Clark Atlanta University

Professor Uzi Landman
School of Physics
Georgia Institute of Technology

Dr. Jianping Gao
School of Physics
Georgia Institute of Technology

Professor Phillip First
School of Physics
Georgia Institute of Technology

Date Approved: October 16, 2007

To my wife,

Beatrice,

for her support and encouragement.

ACKNOWLEDGEMENTS

I thank God first for the grace he gave me to start and finish this thesis. Second I would like to express my sincere gratitude to my advisor Prof. Mei Yin Chou for her patience, guidance and availability in spite of her many commitments. Her scientific rigor and her gentle character made the research journey enjoyable. I also thank Professor Uzi Landman and his group, in particular David Luedtke and Jianping Gao for their availability and willingness to share their knowledge during my project on molecular dynamics. I would like to express my gratitudes to Professor Wang for his help on my first research project and through my learning process on density functional theory. I acknowledge also the support received from the Center for Theoretical Study of Physical Systems (CTSPS) at Clark Atlanta University during my Masters and the beginning of my Ph.D. program. Thanks also to the many graduate students with whom we spent time discussing physics. They contributed a lot to my understanding of physics reasoning. I also wish to thank the many professors I had class with. You were the best in my whole learning career.

I want to acknowledge the contribution of my parents who sacrificed much in order to have me in school; and in particular my sister Helene who did all to to have me enrolled in the first grade. Thanks to my brothers who financially sponsored my education and all those teachers, who gave themselves to teach in spite of their low pay. I want to thank again Professor Murenzi and his family who recognize this work as the fulfilment of their efforts. Last but not least, I would like to thank my wife and children, whose smiles gave me joy even when my research was not progressing.

TABLE OF CONTENTS

LIST OF TABLES

LIST OF FIGURES

SUMMARY

This thesis studies a whole ranges of nanowires properties. We first study the germanium nanowires oriented in the [110] and [111] directions and passivated with hydrogen atoms. Using density functional theory in the local density approximation, we compute the size dependence and the direction dependence of the band gap. GW corrections are also done for nanowires in the [110] direction. We found that nanowires in the [111] direction have an indirect bandgap while those in the [110] direction have a direct bandgap. It is also found that nanowire in [111] direction have a higher bandgap than those in the [110] direction of equal diameter. By fitting the bandgap as a function of diameter using a power function $E_g = E_0 d^{-\alpha}$, we found an exponent of about 1.2 compared to a coefficient of 1.7 obtained for silicon. We have also computed the imaginary part of the susceptibility for nanowires in both directions. We found that the optical gap is close to the band gap

We proceeded to study the properties of ZnO and AlN nanowires in the [001] direction. In the beginning, we discuss the electronic properties of these piezoelectric materials. We show that, in spite of the ionic character, the nanowires need passivation to avoid surface states. We also computed the piezoelectric constant using the Berry phase method and found that, in agreement with recent experiments, these coefficients are lower than bulk values. We also show that if passivation is not applied, the piezoelectric constant is higher than that in the bulk because of the electronic instability introduced. The effect of contraction on the optical properties of nanowires is also ivestigated. Contrary to what happens to the bulk, where a red shift happens, we observe a mixture of red and blue shift for the nanowires due to surface and confinement effect.

Finally, we study the melting temperature of silicon nanowires using classical molecular dynamics. We locate the melting temperature by looking at the discontinuity of materials parameters. These include the potential energy, the self-diffusion coefficient, the angular distribution and much more. We conclude that the melting temperature of nanowires increases with diameter. Moreover, the melting temperature of nanowires in the [110] direction are higher than those in the [111] direction of similar diameter. Extrapolation of our results puts the bulk silicon melting temperature between 1700K and 1800 K, which is a little bit higher than the 1687 K experimental value.

CHAPTER I

INTRODUCTION

There have been great advances in integrated circuit technology that have resulted in higher device density, fast clock rate and lower consumption [1, 2]. Given the demand for even more compact and powerful sytems, there is a growing interest in nanoscale materials that could enable new functions and enhanced performance [3]. Among the best candidate are the most studied carbon nanotubes, nanocrystals and semiconductor nanowires. Semiconductor nanowires have a lot of qualities that are crucial for future applications. First, they can be fabricated with uniform composition up to a diameter of 3 nm [4]. Moreover, a p or n type doping necessary for most material applications has been demonstrated in many cases. This is true for most important materials such as silicon [5], germanium [6] and GaN [7]. Once doping is done, the next step would be to try to make field-effect transistors. Importantly, it was shown that Si, Ge and GaN based nanowire FETs perform comparably with the best devices made with the same materials.

As a consequence, the device size have been shrinking up to the nanoscale size. Problems arise at this size because this is the atomic size range and physics starts to change. Many properties have been found to change at the nanoscale range. In particular, it has been found that the band gap of semiconducting nanowires decreases with diameter due to quantum confinement. The best model for the phenomenon is a $1/d^n$ with d being the diameter and $1 < n < 2$. For silicon nanowires, n was found to be 1.7 while for for InP, it was found to be 1.45 [8]. The next most interesting property is the mechanical property. One of the most known property is the Hall-Petch effect characteristic of polycrystalline solids. This property shows that the yield strength

and hardness of microstructured polycrystalline increases with decreasing size. It was finally shown that the Hall-Petch effect breaks down at the nanoscale range where the materials soften instead [9]. Other similar properties have been found and others may be on the way. We would just mention also the melting temperature that is known to decrease for nanowires. One experiment has measured the melting temperature of germanium nanowires encased in carbon sheaths. The nanowire started melting 280 K before the bulk melting temperature [10].

Many others properties could be mentioned especially in the areas of lasing, phonon transport, magnetic effects and much more. The major task for physicists is to quantify such properties and detect materials with exotic properties worth using in industry. Since experiments are expensive, the best approach is to use computer simulations that are known to yield properties comparable to experiments. This is what led me to this research and sustained my motivation throughout these years.

In chapter 3, we compute the size and direction dependence of the band gap for germanium nanowires. The confinement effect on optical properties is also studied. In chapter 4, we compute the confinement effect on the piezoelectric coefficients of ZnO and AlN nanowires. Finally, chapter 5 seeks to find the size and direction dependence of the melting temperature of silicon nanowires.

CHAPTER II

BACKGROUND THEORY

2.1 Basics of Density Functional Theory

2.1.1 Introduction

The aim of this section is to summarize the concept of density functional theory (DFT) used to solve the many-electron problem [11]. In general, the total Hamiltonian of a system of N electrons in the presence of nuclei can be written as

$$H_{tot} = \sum_i \frac{p_i^2}{2m} + \sum_I \frac{p_I^2}{2M} + \sum_i V_{nucl}(\mathbf{r}_i) + \frac{1}{2}\sum_{i\neq j} \frac{e^2}{|\mathbf{r}_{ij}|} + \frac{1}{2}\sum_{I\neq J} \frac{Z_I Z_J e^2}{|\mathbf{r}_{IJ}|}, \tag{2.1}$$

with

$$V_{nucl}(\mathbf{r}) = -\sum_I \frac{Z_I e^2}{|\mathbf{r} - \mathbf{R}_I|},$$

where the terms appearing in Eq. (2.1) are respectively the kinetic energy of the electrons, the kinetic energy of the nuclei, the electron-nuclei potential energy, the electron-electron interaction and the nuclei-nuclei potential energy. Using the Born-Oppenheimer approximation, we separate out the ionic degree of freedom. Hence, the electronic Hamiltonian becomes

$$H = \sum_i \frac{p_i^2}{2m} - \sum_i \frac{Ze^2}{|\mathbf{r} - \mathbf{R}_i|} + \frac{1}{2}\sum_{i\neq j} \frac{e^2}{|\mathbf{r}_{ij}|}. \tag{2.2}$$

The main problem in the solution of this equation is the presence of the electron-electron interaction in the Hamiltonian. In this chapter, the concept of the density functional theory is introduced in the model of Thomas and Fermi. The failure of the Thomas- Fermi model gives rise to the DFT using Kohn-Sham equations. The Hohenberg-Kohn theorems will be presented along with different approximations of

the exchange and correlation functionals. The approximations that will be used in this work are the local density approximation (LDA) and the generalized gradient approximation (GGA).

2.1.2 Original Idea

The original idea of DFT came from the model of Thomas-Fermi. This model has the advantage of replacing an N electrons equation by a simple density functional $E[\rho]$ [12]. This can be found in a simple way by assuming a cubic box with side l filled with a fixed number of electrons ΔN. At zero temperature, the energy levels are given by

$$\epsilon(n_x, n_y, n_z) = \frac{h^2}{8ml^2}(n_x^2 + n_x^2 + n_x^2) \tag{2.3}$$

where $n_x, n_y, n_z = 1, 2, 3$. The energy and other properties can be computed for this system. Indeed, the number of energy levels between ϵ and $\epsilon + \delta\epsilon$ is given by

$$g(\epsilon) = \frac{\pi}{4}\ (\frac{8ml^2}{h^2})^{3/2}\epsilon^{1/2}, \tag{2.4}$$

The Fermi-Dirac distribution

$$f(\epsilon) = \frac{1}{1 + \exp\left[\beta(\epsilon - \mu)\right]}\,, \tag{2.5}$$

which reduce as the temperature $T \to 0$ to a step function as

$$f(\epsilon) = \begin{cases} 1, & \text{if } \epsilon < \epsilon_F \\ 0, & \text{if } \epsilon > \epsilon_F \end{cases} \tag{2.6}$$

with ϵ_F being the Fermi energy, is used to get energy. The energy in one cell is given by

$$\Delta E = 2\int \epsilon\ g(\epsilon) f(\epsilon) d\epsilon \tag{2.7}$$

$$= \frac{8\pi}{5}(\frac{2m}{h^2})^{3/2}\ l^3\epsilon_F^{5/2}. \tag{2.8}$$

The number of electrons in the cells is given by

$$\Delta N = 2\int g(\epsilon)f(\epsilon)d\epsilon \tag{2.9}$$

$$= \frac{8\pi}{3}(\frac{2m}{h^2})^{3/2}\ l^3\epsilon_F^{3/2}. \tag{2.10}$$

Eliminating the Fermi energy in equations (2.8) and (2.10) we get

$$\Delta E = \frac{3h^2}{10m}(\frac{3}{8\pi})^{2/3}\ \Delta V(\frac{\Delta N}{\Delta V})^{5/3}. \tag{2.11}$$

If the volume of the cell goes to zero, the expression $\frac{\Delta N}{\Delta V}$ becomes the density ρ which is the number of electrons per unit volume. Therefore, the total energy is a function of the density.

$$T_{TF}[\rho] = C_F\int \rho^{5/3}d\mathbf{r}. \tag{2.12}$$

Taking into account the electron-nucleus interaction and the electron-electron interaction, the Thomas-Fermi total energy for an atomic case becomes

$$E_{TF}[\rho] = C_F\int \rho^{5/3}d\mathbf{r} - z\int \frac{\rho(\mathbf{r})}{r}d\mathbf{r} + \frac{1}{2}\int\int \frac{\rho(\mathbf{r}_1)\rho(\mathbf{r}_2)}{|\mathbf{r}_1-\mathbf{r}_2|}d\mathbf{r}_1 d\mathbf{r}_2. \tag{2.13}$$

It is assumed that the ground state minimizes the energy functional (2.13) under the constraint that

$$N = \int \rho(\mathbf{r})d\mathbf{r}. \tag{2.14}$$

Equation (2.13) can then be solved using the method of Lagrange multipliers to get the ground state energy.

The Thomas-Fermi model was viewed as an oversimplified method of no real importance because of the following reasons:

a) no molecular binding was predicted by the method, and

b) the accuracy for atoms was not as high as the accuracy of other methods available at that time.

Nevertheless, the view of this model has changed since the publication by Hohenberg and Kohn paper [13] which proved that the Thomas-Fermi model is an approximation of an exact theory, the DFT.

2.1.3 The Hohenberg-Kohn Theorems

The DFT was made possible by the publication of two important theorems called the Hohenberg-Kohn theorems. Here is a summary of these theorems for a system of N interacting electrons [12].

Theorem 1:

The external potential is determined, within an additive constant, by the electron density.

From this theorem, it is clear that if one has the electron density, one can get the external potential and, hence, all the properties of the ground state such as the kinetic energy, the potential energy and the total energy. In other words, the ground state energy of an interacting electron gas is a unique functional of the electron density. Though the functional is not known, it is a minimum for the true charge density.

Theorem 2:

For a trial density $\rho'(\mathbf{r})$ *such that* $\rho'(\mathbf{r}) \geq 0$ *and* $\int \rho'(r)dr = N$, $E_0 \leq E(\rho')$ *when* $E(\rho')$ *is the energy functional and* E_0 *the ground state energy.*

The theorem provides a justification for the variational principle used in the Thomas-Fermi model. Using this theorem, one can pick a trial density function and the energy associated with it will be above the ground state energy. Thus any variational method that can converge to the correct ground state can be used to minimize the energy functional.

2.1.4 Density Functional Theory and Hartree Approximation

The Hartree method assumes that the motion of an electron is independent of the motion of other electrons [14]. Each electron can be considered as moving in an effective potential which is the sum of the attractive Coulomb potential due to the nucleus and a repulsive potential which represents the average effect of the Coulomb

interaction between the electron i and the other $Z-1$ electrons.

The electrostatic potential due to the electronic charge density $\rho(\mathbf{r})$ is given by

$$V_H(\mathbf{r}) = \int \frac{\rho(\mathbf{r}')}{4\pi\epsilon_0|\mathbf{r}-\mathbf{r}'|}d\mathbf{r}', \tag{2.15}$$

while the electrostatic potential due to the nuclei is

$$V_N(\mathbf{r}) = \sum_i \frac{Z_i e}{4\pi\epsilon_0|\mathbf{r}-\mathbf{R}_i|}. \tag{2.16}$$

The effective potential is then

$$V_{eff}(\mathbf{r}) = V_H(\mathbf{r}) + V_N(\mathbf{r}). \tag{2.17}$$

The wave function of the j^{th} independent electron is given by the solution of the differential equation

$$-\frac{\hbar^2}{2m} \bigtriangledown^2 \Psi_j(\mathbf{r}) + V_{eff}(\mathbf{r})\Psi_j(\mathbf{r}) = \epsilon_j \Psi_j(\mathbf{r}). \tag{2.18}$$

Once this equation is solved, a new charge density can be calculated using the occupied states as followed

$$\rho(\mathbf{r}) = \sum_{j\in occupied} \Psi_j(\mathbf{r})\Psi_j^*(\mathbf{r}). \tag{2.19}$$

The method described above obtains the ground state density self-consistently. Once this density is known, the ground state energy can be obtained using

$$E[\rho(\mathbf{r})] = T[\rho(\mathbf{r})] + \int \rho(\mathbf{r})V_N(\mathbf{r})d\mathbf{r} + \frac{1}{2}\int \rho(\mathbf{r})V_H(\mathbf{r})d\mathbf{r}, \tag{2.20}$$

where T is the kinetic energy of the electrons.

2.1.5 Kohn-Sham Equations

The problem in solving the previous equation is due to the presence of the kinetic energy functional which is hard to compute for interacting electrons. In order to proceed, Kohn and Sham chose to replace the interacting system Hamiltonian with

a non-interacting system easier to solve. For that purpose, they assumed that the density of the non interacting system is equal to that of the interacting system [17]. This led to independent-particle equations of a non-interacting system with all the many body terms grouped together in the exchange-correlation functional.

With these considerations, the kinetic energy is given by

$$T_0 = \sum_i^N < \Psi_i | \frac{-\hbar^2 \nabla^2}{2m} | \Psi_i > . \tag{2.21}$$

The energy functional can be written as

$$E[\rho(\mathbf{r})] = T_0[\rho(\mathbf{r})] + \int \rho(\mathbf{r}) V_N(\mathbf{r}) d\mathbf{r} + \frac{1}{2} \int \rho(\mathbf{r}) V_H(\mathbf{r}) d\mathbf{r} + E_{xc}[\rho(\mathbf{r})]. \tag{2.22}$$

where the exchange-correlation is given by

$$E_{xc}(\rho) = T(\rho) - T_0(\rho) + V_{ee}(\rho) - V_H(\rho). \tag{2.23}$$

In this expression, we can see that the exchange-correlation energy functional contains the difference between the interacting electron kinetic energy functional and the non-interacting one and the non classical part of the electron-electron interaction. The Kohn-Sham equations are then of the form:

$$-\frac{\hbar^2}{2m} \bigtriangledown^2 \Psi_j(\mathbf{r}) + V_{eff}(\mathbf{r}) \Psi_j(\mathbf{r}) = \epsilon_j^{KS} \Psi_j(\mathbf{r}), \tag{2.24}$$

$$V_{eff}(\mathbf{r}) = V_H(\mathbf{r}) + V_N(\mathbf{r}) + V_{xc}(\mathbf{r}), \tag{2.25}$$

$$\rho(\mathbf{r}) = \sum_{j \in occupied} \Psi_j(\mathbf{r}) \Psi_j^*(\mathbf{r}), \tag{2.26}$$

where the exchange-correlation potential is given by

$$V_{xc}(\mathbf{r}) = \frac{\delta E_{xc}[\rho(\mathbf{r})]}{\delta \rho(\mathbf{r})}. \tag{2.27}$$

The Kohn-Sham equations can be computed self-consistently if one knows the exact exchange-correlation functional. The search of accurate $E_{xc}[\rho]$ is the greatest challenge of the DFT. Nevertheless, some approximations have been proposed. These are the local Density approximation (LDA), the generalized gradient approximation (GGA), etc.

2.1.6 Approximations

2.1.6.1 Local Density Approximation (LDA)

In the LDA, the local exchange-correlation energy is the sum of two terms [11, 16], the exchange term ϵ_x and the correlation term ϵ_c which are respectively the exchange and correlation energy of a uniform electron gas of density $\rho(\mathbf{r})$,

$$\epsilon_{xc} = \epsilon_x + \epsilon_c, \tag{2.28}$$

with

$$\epsilon_x(\rho) = -\frac{3}{4}(\frac{3}{\pi})^{1/3}\rho(r)^{1/3},$$

and

$$\epsilon_c(\rho) = \begin{cases} -0.1423/(1 + 1.0529\sqrt{r_s} + 0.3334r_s), & \text{if } r_s \geq 1 \\ -0.0480 + 0.0311ln(r_s) - 0.116r_s + 0.0020r_s\ ln(r_s), & \text{if } r_s \leq 1. \end{cases} \tag{2.29}$$

The application of the LDA to atoms and molecules is done by assuming that the exchange-correlation energy of a non-uniform system can be obtained by using infinitesimal portions of the uniform gas and summing the energy over the volume. The LDA is the most used method in DFT. It can be used even if the density varies rapidly. The method can be used to get structural properties such as the lattice constant, the bulk modulus, the phonon frequencies, and the surface structures.

2.1.6.2 Generalized Gradient Approximation (GGA)

In the LDA, the exchange and correlation functional is a function of the density. In the GGA, this functional is a function of the density and of its gradient. As an example, the exchange energy proposed by Perdew and Wang is given by[15]

$$E_x[\rho] = A_x \int d^3\mathbf{r} F(s), \tag{2.30}$$

where $s = \frac{|\nabla\rho|}{2K_F\rho}$, $A_x = -\frac{3}{4}(\frac{3}{\pi})^{1/3}$, $K_F = (3\pi^2\rho)^{1/3}$, $F(s) = (1 + 0.0864\frac{s^2}{m} + bs^4 + cs^6)^m$, $m = \frac{1}{15}, b = 14,\ c = 0.2$.

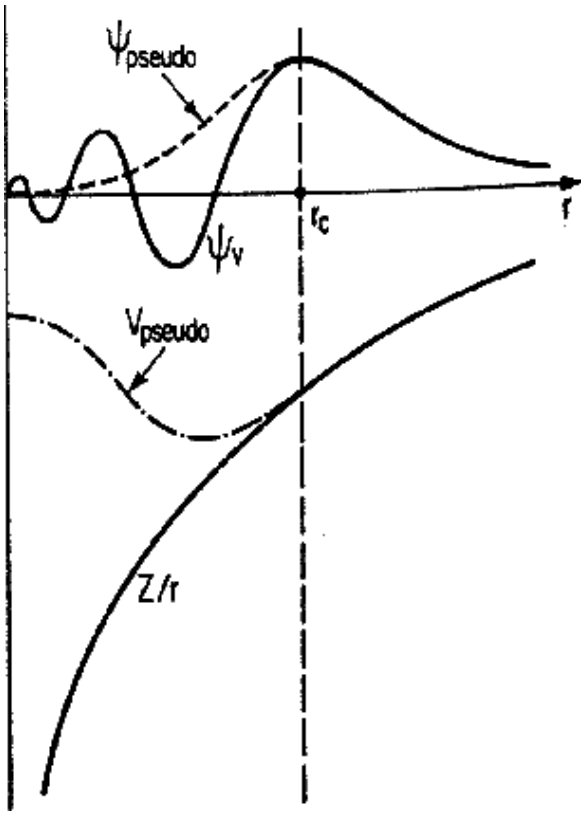

Figure 2.1: Ion-electron potential V and pseudopotential V_{pseudo} (bottom curves with a wavefunction Ψ and its pseudo counterpart Ψ_{pseudo}.

2.1.7 Pseudopotential

Another approximation that needs to be done is on the ion-electron potential. The reason such an approximation is needed is that a very large number of plane waves would be needed to expand the tightly bound core orbitals. As shown on Figure 2.1, a regular wavefunction will have many nodes near the origin while the pseudo wavefunction has only one node. Moreover, we see that the pseudopotential and the true potential are identical beyond the core radius r_c, as it is the case for the wavefunctions. The following discussion shows how a pseudopotential can be constructed, allowing the use of only smooth wavefunctions but getting the same eigenvalues as if one was using the true potential.

The valence electron wavefunction is decomposed into a sharp varying core state

ϕ_{core} and a smooth varying ϕ part as :

$$|\psi >= |\phi > + \sum C_{core}|\phi_{core} > \tag{2.31}$$

Since the core states are orthogonal to the valence states ($< \phi_{core}|\psi >= 0$), $C_{core} = - < \phi_{core}|\phi >$.

Starting from the one particle Schrödinger equation $H|\psi = E|\psi >$, we get

$$H|\phi > + H \sum_{core} C_{core}|\phi_{core} >= E|\phi > + E \sum_{core} C_{core}|\phi_{core} > \tag{2.32}$$

$$\iff H|\phi > + \sum_{core} E_{core} C_{core}|\phi_{core} >= E|\phi > + \sum_{core} E C_{core}|\phi_{core} > \tag{2.33}$$

$$\iff H|\phi > + \sum_{core} (E_{core} - E) C_{core}|\phi_{core} >= E|\phi > \tag{2.34}$$

$$\iff H|\phi > + \sum_{core} (E - E_{core})|\phi_{core} >< \phi_{core}|\phi >= E|\phi > \tag{2.35}$$

$$\iff \{H + \sum_{core} (E - E_{core})|\phi_{core} >< \phi_{core}|\}|\phi >= E|\phi > \tag{2.36}$$

If we assume that

$$V_{ps} = \sum_{core} (E - E_{core})|\phi_{core} >< \phi_{core}| \tag{2.37}$$

We can write our Shrödinger equation in the following more elegant form.

$$(H + V_{ps})|\phi >= E|\phi > \tag{2.38}$$

We see that by adding a new term V_{ps} to the Hamiltonian, We can use the valence state and still get energy eigenvalues as if we were using all the electrons. There are three major forms of pseudopotentials: The first one is the norm conserving pseudopotential [50] . The main characteristic is the fact that when they are constructed, the pseudo wavefunction and the real wavefunction must be identical outside the core region. Moreover, the integral of the squared wavefunctions must be equal inside the core region. Finally, the valence all electron potential and the pseudopotential must have the same eigenvalues. In spite of the introduction of norm conserving

pseudopotentials, their application for highly localized valence orbitals (such as the first row elements and transition metals) were limited because they required a large cutoff radius. That is what led to the introduction of ultrasoft pseudopotentials [48] and the Projector Augmented wave pseudopotentials (PAW) [22].

2.2 Optical properties of materials

In this section, we review how to obtain the transverse dielectric function for a homogeneous or nearly homogeneous material [11, 17]. This function is important since it provides information on a material absorption and other properties. We consider a general case where we have an unperturbed Hamiltonian

$$H_o = -\frac{\hbar^2\nabla^2}{2m} + V(r) \tag{2.39}$$

In the presence of a magnetic field with vector potential $\mathbf{A}(\mathbf{r},t)$ the Hamiltonian becomes

$$H = -\frac{1}{2m}[\mathbf{P} + \frac{e}{c}\mathbf{A}(\mathbf{r},t)]^2 + V(r) = H_o + \frac{e}{mc}\mathbf{A}(\mathbf{r},t)\cdot\mathbf{P} + \frac{e^2}{2mc^2}\mathbf{A^2}(\mathbf{r},t) \tag{2.40}$$

We will assume a transverse magnetic field $\mathbf{A}(\mathbf{r},t)$ with frequency ω, wavevector q and polarization $\mathbf{e}$ such that $\mathbf{e}\perp\mathbf{q}$. We will also work in the coulomb gauge where div $\mathbf{A}$ =0 such that A and P commute. In the dipole approximation, we can neglect the second order term in $\mathbf{A}(\mathbf{r},t)$ and take the linear term as perturbation.

$$H_p(q,\omega) = \frac{eA_o}{mc}\mathbf{e}\cdot\mathbf{p}(e^{i(q\cdot r-\omega t)} + e^{-i(q\cdot r-\omega t)}) \tag{2.41}$$

This perturbation can be generated by applying an electric field given by

$$E(r,t) = E_o\,\mathbf{e}\,e^{i(q\cdot r-\omega t)} + c.c \tag{2.42}$$

with $E_o = i\omega A_o/c$

This perturbation can induce transitions among states of H_o with absorption or emission of energy $\hbar\omega$. Using the Fermi golden rule and assuming a fermi distribution

$f(E)$, the number of transition per unit time is given by :

$$W(q,\omega) = \frac{4\pi}{\hbar}(\frac{eA_o}{mc})^2 \sum_{i,j} | < \psi_i | A_o e^{iq\cdot r} \mathbf{e}\cdot\mathbf{p} | \psi_j >^2 \delta(E_j - E_i - \hbar\omega) \tag{2.43}$$

The power dissipated is therefore

$$P(q,\omega) = \hbar\omega W(q,\omega) = 4\pi\omega(\frac{eA_o}{mc})^2 \sum_{i,j} | < \psi_j | e^{iq\cdot r} \mathbf{e}\cdot\mathbf{p} | \psi_i >^2 \delta(E_j - E_i - \hbar\omega) \tag{2.44}$$

On the other hand, we expect that an electric field applied to an isotropic medium will generate an electric current parallel to the electric field. Using Ohm law, $j(r,t) = \sigma(q,\omega)E(r,t)$ where $\sigma(q,\omega)$ is the conductivity. Moreover, we know that the power dissipated in the volume V is given by

$$P(q,\omega) = \int_V \mathbf{j}\cdot\mathbf{E}dr = 2\sigma_1(q,\omega)\frac{1}{c^2}\omega^2 A_o^2 V \tag{2.45}$$

We can now see that

$$\sigma_1(q,\omega) = \frac{c^2}{2V}\frac{\hbar\omega W(q,\omega)}{\omega^2 A_o^2} \tag{2.46}$$

We know that the dielectric function is related to the conductivity by

$$\epsilon(q,\omega) = 1 + \frac{4\pi i}{\omega}\sigma(q,\omega) \tag{2.47}$$

It follows from this previous expression that

$$\epsilon_2(q,\omega) = \frac{4\pi}{\omega}\sigma_1(q,\omega) = \frac{2\pi\hbar c^2 W(q,\omega)}{\omega^2 V A_o^2} \tag{2.48}$$

Considering $q = 0$ and transitions between occupied states and unoccupied state, we can write the imaginary part of the dielectric function as

$$\epsilon_2(\omega) = \frac{8\pi^2 e^2}{\omega^2 m^2 V} \sum_{i,j} | < \psi_i | \mathbf{e}\cdot\mathbf{p} | \psi_j >^2 \delta(E_j - E_i - \hbar\omega) \tag{2.49}$$

Writing the expression for the Brillouin zone and setting $\hbar\omega_{ij} = E_j - E_i$, we get

$$\epsilon_2(\omega) = \frac{8\pi^2 e^2}{m^2\omega^2}\frac{1}{(2\pi)^3}\int_{BZ} | < \psi_j(k) | \mathbf{e}\cdot\mathbf{p} | \psi_i(k) >^2 \delta(\omega_{ij}(k) - \omega)dk \tag{2.50}$$

This expression will be computed for the next two chapters both for germanium nanowires and for piezoelectric nanowires (ZnO and AlN).

2.3 Berry Phase

The Berry phase is a very important concept that has helped compute material properties outside the traditional quantum mechanic domain. It is sometimes called geometric phase and we will define it in the next sections. In particular, this concept is used in computing the crystal polarization. The reason it had been difficult to compute the crystal polarization before was that it cannot be cast as an expectation value of a certain operator as we are used to see in quantum mechanics. Most of the following discussions follow that done by Resta in his paper and lecture notes [19, 20].

2.3.1 Discrete geometric phase

The concept of geometric phase is important when we have a Hamiltonian that depends on a parameter λ. The Hamiltonian will be written as $H(\lambda)$ and the ground state wavefunction as $\psi(\lambda)$. The phase difference between two ground states can be defined as:

$$e^{-i\Delta\phi_{12}} = \frac{<\psi(\lambda_1)|\psi(\lambda_2)>}{|<\psi(\lambda_1)|\psi(\lambda_2)>|} \tag{2.51}$$

$$\Delta\phi_{12} = -Im\{log <\psi(\lambda_1)|\psi(\lambda_2)>\} \tag{2.52}$$

The value of $\Delta\phi_{12}$ is known modulo 2π. Moreover, it can be seen that this phase cannot have a physical meaning since any quantum mechanics state is arbitrary to a constant phase factor. One way to remove the arbitrariness is to add the phases along a closed path. In Figure 2.2, we show 4 states that depend on the parameter λ. The phase accross the four states would be given by

$$\phi = \Delta\phi_{12} + \Delta\phi_{23} + \Delta\phi_{34} + \Delta\phi_{41} \tag{2.53}$$

$$\phi = -Im\{log <\psi(\lambda_1)|\psi(\lambda_2)><\psi(\lambda_2)|\psi(\lambda_3)><\psi(\lambda_3)|\psi(\lambda_4)><\psi(\lambda_4)|\psi(\lambda_1)>\} \tag{2.54}$$

$$\phi = -Im\{log \prod_{i=1} <\psi(\lambda_i)|\psi(\lambda_{i+1})>\} \tag{2.55}$$

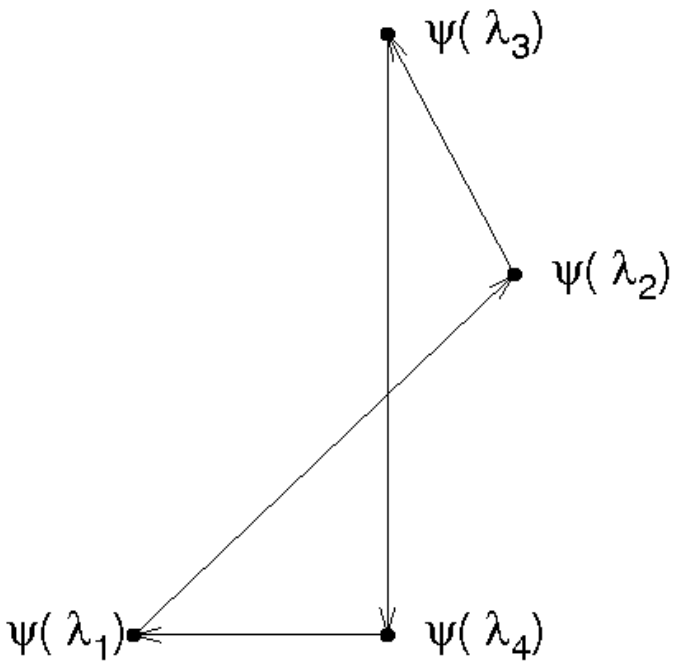

Figure 2.2: Parameter dependent ground states wavefunctions

The gauge-arbitrary phases cancel in pairs so that the overall phase ϕ is a gauge-invariant quantity. Such a gauge invariant can be an observable though the phase depend on the curve followed.

2.3.2 Continuous Berry phase

We showed in the previous paragraph how the phase changes between two ground states of an parameter dependent Hamiltonian. If we were to use very close parameters λ and $\lambda + \Delta\lambda$, the phase would be given by

$$e^{-i\Delta\phi} = \frac{< \psi(\lambda)|\psi(\lambda + \Delta\lambda) >}{| < \psi(\lambda)|\psi(\lambda + \Delta\lambda) > |}. \tag{2.56}$$

We can expand the exponential term and the wavefunction around $\psi(\lambda)$ keeping the first term only and we get

$$-i\Delta\phi =< \psi(\lambda)|\nabla_\lambda \psi(\lambda)\Delta\lambda) > . \tag{2.57}$$

We can then integrate around a curved path and obtain the general formula for the Berry phase which is

$$\phi = i \oint_C < \psi(\lambda) | \nabla_\lambda \psi(\lambda) > d\lambda. \tag{2.58}$$

2.3.3 Berry phase in a solid

In this section, we use previous knowledge in order to deal with the crystalline system. We know that the orbitals have the Bloch form because of the periodic boundary condition. They have the form

$$\psi_{nk}(r + \tau) = e^{ik.\tau} \psi_{nk}(r). \tag{2.59}$$

where τ is the lattice translation and k is the Bloch momentum. We know that the Bloch orbital obeys the Schrödinger equation as

$$[\frac{1}{2m} p^2 + V(r)] \psi_{nk}(r) = \epsilon_n(k) \psi_{nk}(r). \tag{2.60}$$

We can decompose the Bloch function in a plane wave times a function having the periodicity of the lattice as:

$$\psi_{nk}(r) = e^{ik.r} u_{nk}(r). \tag{2.61}$$

The Schödinger equation becomes

$$[\frac{1}{2m} (p + \hbar k)^2 + V(r)] u_{nk}(r) = \epsilon_n(k) u_{nk}(r). \tag{2.62}$$

We started with a non parametric Hamiltonian but now we do have a k dependent Hamiltonian. This means we can get the Berry phase for band n using Eq. (2.55) as:

$$\phi = i \int_C < u_{nk} | \nabla_k u_{nk} > dk. \tag{2.63}$$

In this equation, the integration is done from k_i to a k_f such that their difference is a reciprocal lattice $\vec{G}$. At these two points, the Bloch eigenstates obey the same Schrödinger equation and the same boundary condition. If we want to know the

phase of the whole system, we need to add the phases of all the bands up to the top of the valence band. In case there is band crossing, there is is an arbitrariness in attributing n as a function of k. But, the phase does not change except when there is crossing between an empty state and an occupied state. Therefore, the phase of a semiconductor crystalline solid is unique(modulo 2π). For centro-symmetric material with origin at the center of symmetry, the value of the Berry phase is either 0 or π and therefore uninteresting. The discussion in the next section and in Chapter 4 will be related to non-centro-symmetric materials, especially wurtzite oxides.

2.3.4 Polarization and Berry phase

The ability to compute the polarization of a non-centro symmetric crystal is very important since from them, other properties can be found such as the piezoelectric coefficients, the pyroelectric constants and others. The polarization is induced either by compression or by a temperature change. For the piezoelectric case, the parameter in the Hamiltonian is the the strain ϵ that we keep as λ . At a given value of λ, the electronic part of the polarization is given by

$$P(\lambda) = \frac{-ie}{(2\pi)^3} \sum_n \int_{BZ} d\mathbf{k} < u_{\lambda,nk} | \nabla_{\mathbf{k}} | u_{\lambda,nk} > . \tag{2.64}$$

As we can see, this formula can be written as $P(\lambda) = -e\phi/\Omega$ where Ω is the volume of the Brillouin zone. The equation for the polarization seems beautiful but in reality, it is hard to compute since there is no relationship between phases of u_{nk} obtained through a diagonalization routine. In practice, the components of $P(\lambda)$ are obtained independently along the three reciprocal lattice vectors $\vec{G}_1$, $\vec{G}_2$ and $\vec{G}_3$. As an example, the computation along the vector $\vec{G}_1$ is computed as

$$P_1 = \frac{-ife}{(2\pi)^3} \int_A dk_2 dk_3 \sum_{n=1}^{M} \int_0^{|G1|} dk_1 < u^{\lambda}_{nk} | \frac{\partial}{\partial k_1} | u^{\lambda}_{nk} > \tag{2.65}$$

In this formula, A is given by the area spanned by $\vec{G}_2$ and $\vec{G}_3$ and f is the occupation number. Other components of the polarization are obtained the same way. In order to

remove the random phase introduced during the diagonalization process, King-Smith and Vanderbilt [57] proposed a method that replaced the line integral by a formula similar to Eq. (2.52) as:

$$\phi_J^{\lambda}(K_{\perp}) = Im\{log \prod_{j=0}^{J-1} det(< u_{nk_j}^{\lambda} | u_{nk_{j+1}}^{\lambda} >)\} \tag{2.66}$$

This means that for every k-points in the perpendicular ($\perp$) direction, we evaluate the cell periodic part of the wavefunction at a string of J k-points so that $k_j = K_{\perp} + jG_{\parallel}/J$. The key in removing the random phase is requiring that the wavefunction $u_{nk_j}^{\lambda}$ at each point on the string be obtained from the knowledge of $u_{nk_0}^{\lambda}$ as $u_{nk_j}^{\lambda}(r) = e^{-iG_{\parallel}.r} u_{nk_0}^{\lambda}(r)$. Once the phase for each k-point is obtained, the polarization is computed as

$$(P_e^{\lambda})_i = \frac{feR_i}{2\pi\Omega N_{k_{\perp}}} \sum_{k_{\perp}} \phi_J^{\lambda}(k_{\perp}) \tag{2.67}$$

where Ω is the volume of the unit cell. The change in polarization is nevertheless not unique. It is obtained modulo feR/Ω where f is the occupation number, R the lattice constant in the the given direction. This is not a major problem since we are mostly interested in change far less than this period.

After the electronic part is obtained, we can compute the ionic contribution given by:

$$\Delta P_{ion} = \sum_i \frac{|e| Z_i C_i}{\Omega}. \tag{2.68}$$

where Z is the valence of ion i and C_i is the Z coordinate of ion i.

2.4 Classical Molecular Dynamics

2.4.1 Introduction

We described earlier how to compute the total energy of a solid using quantum mechanics. In the introduction part of this chapter, it was shown how the ionic part of the kinetic energy can be neglected. This assumption does not hold when simulating

a crystal at finite temperature. We need to use molecular dynamics (MD) for this effect. We distinguish classical molecular dynamics and quantum molecular dynamics. The latter is very expensive and has been extensively reviewed by Payne *et al.* [24]. On the contrary, classical molecular dynamics is simple and inexpensive and will be used in Chapter 4 for silicon nanowires. The basic concepts behind this technique are given in the next section.

2.4.2 Particle Interaction

In the classical molecular dynamics, a system is completely determined by its classical Hamiltonian. The total Hamiltonian is given by [25]

$$H = \frac{1}{2}\sum_{i=1}^{N} m_i v_i^2 + \sum_{i<j}^{N} V_{(2)}(r_i, r_j) + \sum_{i<j<k}^{N} V_{(3)}(r_i, r_j, r_k) \tag{2.69}$$

where m_i is the mass of the atoms (there are no electrons in this formalism), v_i their velocity, r_i their positions. $V_{(2)}$ is the two-body potential interaction while the $V_{(3)}$ is the three-body potential if included. Depending on the model, people may want to include only short-range interaction or long-range interactions. In most of our calculations, we are only interested in the short-range interaction. For this purpose, a cutoff distance is chosen beyond which the interaction becomes zero. Many forms of potentials have been described in the literature. We explore in the remaining part of this section, three popular potentials and their benefits and problems. The first one that includes only $V_{(2)}$ is the Lennard-Jones (L-J) potential given by [26]

$$U(r) = 4\epsilon[(\frac{\sigma}{r})^6 - (\frac{\sigma}{r})^{12}] \tag{2.70}$$

where ϵ is the minimum potential energy located at $r = 2^{1/6}\sigma$. It is known that sometimes, L-J potential gives an accurate approximation of the true potential especially in noble gases like argon. Nevertheless, exponential potentials seem to be more accurate. The most known exponential potential is the Stillinger-Weber potential,

usually used for material with tetrahedral coordination. It is given by:

$$V = \sum_{i<j} V_2(i,j) + \sum_{i<j<k} V_3(i,j,k) \tag{2.71}$$

where the two-body potential V_2 is given by

$$V_2(r) = \begin{cases} (Br^{-p} - r^{-q}) \exp[(r-a)^{-1}] & \text{if } r < a \\ 0 & \text{if } r \geq a \end{cases} \tag{2.72}$$

and the three-body term V_3 given by

$$V_3(i,j,k) = h(r_{i,j}, r_{i,k}, \theta_{jik}) + h(r_{j,i}, r_{j,k}, \theta_{ijk}) + h(r_{k,i}, r_{k,j}, \theta_{ikj}) \tag{2.73}$$

where

$$h(r_{i,j}, r_{i,k}, \theta_{jik}) = \lambda \, exp[\gamma(r_{ij} - a)^{-1} + \gamma(r_{ik} - a)^{-1}](cos(\theta_{jik}) + 1/3)^2 \tag{2.74}$$

In these previous formulas, r is the distance between any pair of atoms, a is the cutoff distance for the two-body term and θ is the bond angle between triplet of atoms. The parameters $(A, B, p, q, \lambda, \gamma)$ are positive parameters fitted to reproduce properties of materials. Another popular type of potential is the Tersoff potential which looks like a two-body potential but is rather a three-body potential. The family of potentials developed by Tersoff [28] , are based on the concept of bond order: the strength of a bond between two atoms is not constant, but depends on the local environment. The Tersoff potential has the appearance of a pair potential:

$$V = \frac{1}{2} \sum_{ij} \phi_R(r_{ij}) + \frac{1}{2} \sum_{ij} B_{ij} \phi_A(r_{ij}) \tag{2.75}$$

where R and A stand respectively for repulsive and attractive. However, it is not a pair potential because B_{ij} is not a constant. In fact, it is the bond order for the bond joining i and j, and it is a decreasing function of a "coordination" G_{ij} assigned to the bond: $B_{ij} = B(G_{ij})$. The parameter G_{ij} is in turn defined as

$$G_{ij} = \sum_k f_c(r_{ik}) g(\theta_{jik}) f(r_{ij} - r_{ik}) \tag{2.76}$$

where $f_c(r)$, $f(r)$ and $g(\theta)$ are suitable functions. The basic idea is that the bond ij is weakened by the presence of other bonds ik involving atom i. This scheme is more general than the Stillinger-Weber potential, however it is difficult to find a good fit since there are 6 functions to fit in addition to the angular terms. In our simulation of silicon nanowires, we just used the Stillinger-Weber potential since it is well parameterized [29].

2.4.3 Atom equation of motion

Once the potential is known, the next step is to get the force acting on each atom. We know from The Newtons equation of motion that $\vec{F_i} = m_i\vec{a_i}$ where F_i is the force acting on particle i and a_i is its acceleration. Moreover, we know that these forces are derived from the potential energy as $\vec{F_i} = -\nabla_i V$. We therefore need to obtain the sum of all the forces acting on particle i in order to compute its acceleration. In the computation of forces between particles, the periodic boundary condition plays a major role. This is due to the fact that we want to simulate an extended system while using a limited number of particles. For a given particle in a cell, we look at its nearest neighbors, not only in the same cell but also in the neighboring cells where we have mirrors of all the particles. In Figure 2.3, we are interested in forces acting on particle 1. We could see that the images of particles 2, 3 and 4 are closer to particle 1 than the particle themselves. On the contrary, particle 5 is closer to 1 than any of its mirror images.

Once each particle's acceleration is obtained, we can get the velocity and the position of each particle at time $t + \delta t$ if they are known at time t by :

$$r(t+\delta t) = r(t) + v(t)\delta t + \frac{1}{2}a(t)\delta t^2 + \frac{1}{6}b(t)\delta t^3... \tag{2.77}$$

$$v(t+\delta t) = v(t) + a(t)\delta t + \frac{1}{2}b(t)\delta t^2 + \frac{1}{6}c(t)\delta t^3..., \tag{2.78}$$

where a,b and c are the second, the third and fourth derivatives of the coordinates and δt is the time step of the calculation. A calculation like the one mentioned above

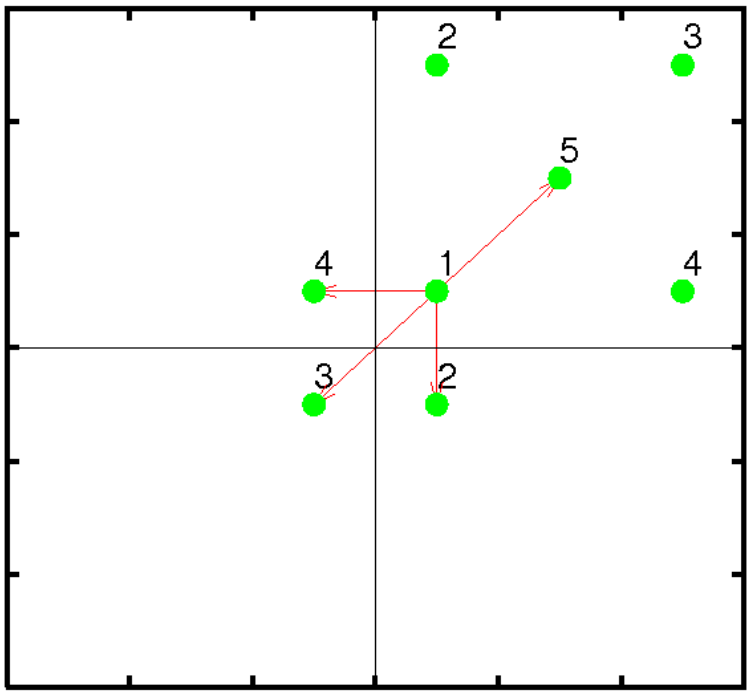

Figure 2.3: Fives particles in a squared cell with their mirror images. Interaction between particle 1 and its nearest neighbors is shown.

would require a lot of computer memory since for each particle, all these derivatives have to be stored. One of the most simple algorithm often used is the Verlet algorithm [30, 31]. This algorithm stems from the previous one by writing

$$r(t+\delta t) = r(t) + v(t)\delta t + \frac{1}{2}a(t)\delta t^2 \tag{2.79}$$

$$r(t-\delta t) = r(t) - v(t)\delta t + \frac{1}{2}a(t)\delta t^2. \tag{2.80}$$

From these two equations, we get

$$r(t+\delta t) = 2r(t) - r(t-\delta t) + a(t)\delta t^2. \tag{2.81}$$

The advantage of this equation is the fact that it does not involve the calculation of velocity. The position at time $t+\delta t$ needs the knowledge of accelerations at time t and positions at time t and $t-\delta t$. It requires modest storage space and it is straightforward. Unfortunately, it is of moderate precision.

Another commonly used method is the Beeman algorithm [32]. The position at time $t + \delta t$ is given by

$$r(t + \delta t) = r(t) + v(t)\delta t + \frac{2}{3}a(t)\delta t^2 - \frac{1}{6}a(t - \delta t)\delta t^2. \tag{2.82}$$

Once the positions are known, new accelerations are computed and the velocities are then calculated as :

$$v(t + \delta t) = v(t) + \frac{1}{3}a(t + \delta t)\delta t - \frac{1}{6}a(t - \delta t)\delta t. \tag{2.83}$$

In this algorithm, the computer has to memorize accelerations at three time steps. This requires more memory but results are generally more accurate than from the Verlet algorithm.

The method that will be used in calculations for this dissertation involves the use of the predictor-corrector method. Many of these methods do exist but a look at the Gear algorithm of fifth order [33] will illustrate how they work. In the beginning, the positions and other derivatives will be predicted like in previous methods. In order to simplify the expression, we will use scaled position derivatives as $r_i = \frac{1}{i}(\frac{\partial^i r}{\partial t^i})\delta t^i$ where r_i is the i^{th} derivative of the position at time t. They are supposed to be known at time t and one is interested in computing their values at time $t + \delta t$. The predicted positions and their derivative is given by

$$\begin{bmatrix} r_0^p(t+\delta t) \\ r_1^p(t+\delta t) \\ r_2^p(t+\delta t) \\ r_3^p(t+\delta t) \\ r_4^p(t+\delta t) \\ r_5^p(t+\delta t) \end{bmatrix} = \begin{bmatrix} 1 & 1 & 1 & 1 & 1 & 1 \\ 0 & 1 & 2 & 3 & 4 & 5 \\ 0 & 0 & 1 & 3 & 6 & 10 \\ 0 & 0 & 0 & 1 & 4 & 10 \\ 0 & 0 & 0 & 0 & 1 & 5 \\ 0 & 0 & 0 & 0 & 0 & 1 \end{bmatrix} \begin{bmatrix} r_0(t) \\ r_1(t) \\ r_2(t) \\ r_3(t) \\ r_4(t) \\ r_5(t) \end{bmatrix} \tag{2.84}$$

Once the new particle position is obtained, we can compute the acceleration $r_2(t+\delta t)$ using again Newton equations of motion. This allows us to make correction since this

acceleration has to match the predicted acceleration. We compute $\delta r_2 = r_2(t+\delta t) - r_2^P(t+\delta t)$ and get the corrected position and derivatives as :

$$\begin{bmatrix} r_0^c(t+\delta t) \\ r_1^c(t+\delta t) \\ r_2^c(t+\delta t) \\ r_3^c(t+\delta t) \\ r_4^c(t+\delta t) \\ r_5^c(t+\delta t) \end{bmatrix} = \begin{bmatrix} r_0^p(t+\delta t) \\ r_1^p(t+\delta t) \\ r_2^p(t+\delta t) \\ r_3^p(t+\delta t) \\ r_4^p(t+\delta t) \\ r_5^p(t+\delta t) \end{bmatrix} + \begin{bmatrix} 3/16 \\ 251/360 \\ 1 \\ 11/18 \\ 1/6 \\ 1/60 \end{bmatrix} \begin{bmatrix} \delta r_2(t) \\ \delta r_2(t) \\ \delta r_2(t) \\ \delta r_2(t) \\ \delta r_2(t) \\ \delta r_2(t) \end{bmatrix} \tag{2.85}$$

The choice of the method depend on many parameters. In particular, one has to make sure the simulation is stable for a long interval of time. Moreover, it is preferable if the method does not require a large computer memory since this reduces the number of particles users can handle.

2.4.4 Different ensembles

The obtained position and derivatives from the previous steps save to abide by the ensemble requirement. The ensemble used in the simulation is either the microcanonical (constant N, V, E) or the canonical ensemble (constant N, V, T). The easy way would be to compute these constants and force them to remain constant. However, this is not how it is done since these properties are thermodynamic quantities. They are only true when considering averages. Therefore, the total energy or the temperature will be allowed to oscillate around an equilibrium value.

The microcanonical ensemble is considered the natural ensemble for molecular dynamics simulations. Since there are no external forces acting on our systems, the total energy should be conserved . But in reality, the conservation of the total energy is violated due to round-off errors and in the accuracy of the integration of the equation of motion. The error increases significantly when using a big time step. The choice of the time step is then chosen in a such way that the total energy fluctuation

be far smaller than the average kinetic energy.

Most sophisticated is the simulation of a canonical ensemble. The easy way to control the temperature is to scale the velocities such that V_i is replaced by $V_i\sqrt{T_0/T}$ where T is the current temperature and T_0 is the temperature we want to keep constant [34]. In this formula, $\sum_i \frac{1}{2}m_i v_i^2 = \frac{3}{2}NKT$ assuming N to be the total number of particles. In most simulations such as the one that will be used in Chapter 4, the scaling of velocities is done in such a way that the system would reach the desired temperature after many time steps. The velocities are then scaled by a factor λ given by $[1 + \frac{\delta t}{\tau_T}(\frac{T_0}{T} - 1)]^{\frac{1}{2}}$, where the constant τ_T called the coupling time depends on how fast we want to reach the ideal temperature.

2.5 Conclusion

We have shown how from the original idea of Thomas Fermi, the ground state of a material can be computed using the density as the building block. We showed what assumptions are made on the Hamiltonian especially for the exchange-correlation term and how the ion-electron interaction is replaced by a pseudopotential. Once the wavefunctions and eigenstates are obtained, we showed how optical properties can be computed. This theory was important in order to understand how these properties are computed in the next two chapters. In Chapter 4 , we will use the concept of Berry phase and polarization as discussed briefly in this Chapter. Finally, we included a quick review of classical molecular dynamics, from setting the potential to the integration of the equations of motion. This is important in order to understand the last Chapter of this dissertation dealing with the melting of silicon nanowires.

CHAPTER III

ELECTRONIC AND OPTICAL PROPERTIES OF GERMANIUM NANOWIRES

3.1 Introduction

Nanoscale materials have attracted a great deal of attention because of their unique properties not found in the bulk. In particular, semiconductor nanowires offer many potential applications in electronics and optoelectronic devices [35, 36]. Indeed, the band gap increases with the decrease of nanowire diameter due to the quantum confinement effect, which allows the control of photoluminescence effects over a wide range of wavelengths [37, 38]. While most of the studies in this area have focused on silicon nanowires, interest in studying other materials such as germanium nanowires is growing. Interestingly, germanium nanowires are known to make high quality field effect transistors (FET) due to their high electron and hole mobility [39, 40].

Although there exists a wealth of experiments on the fabrication of germanium nanowires [41, 42, 43], few of their properties are well understood.This is due to the fact that accurate measurements are challenging at this size range. Therefore, a theoretical work is important in exploring the interesting features in these systems.

On the theoretical front, the band gap and the dielectric function of germanium nanowires along [111], [110], and [100] were calculated up to 1.2 nm diameter [44]. The self-energy was not considered in the calculation of the energy gaps. Bruno *et al.* [45] studied the electronic and optical properties for Ge nanowires up to 0.8nm in diameter including the excitonic effect. In this study, we extend the calculation of the electronic properties to nanowires of diameter up to 4nm and examine the diameter dependence in detail.In particular, we present results of a systematic calculation of

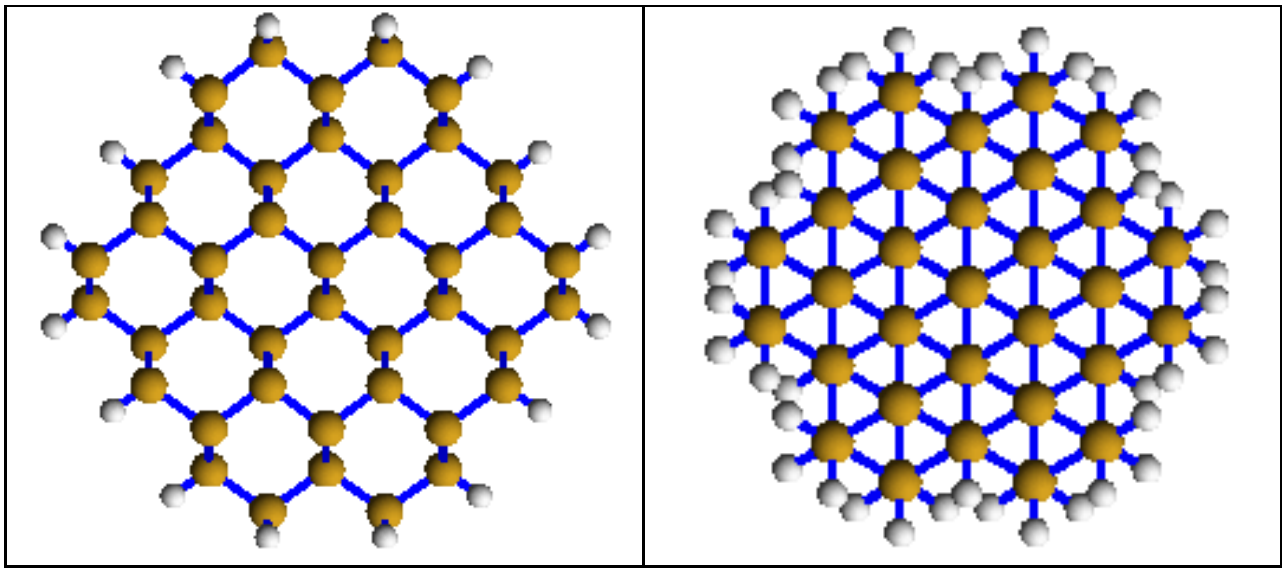

Figure 3.1: (Color online) Top view of the ball-and-stick model for Ge nanowires along [110] (left panel) and [111] (right panel), respectively.

the band gap of nanowires of different diameters along different orientations. The two primary orientations considered are [111] and [110]. The choice of these two directions is dictated by experimental observations that found the [111]-oriented nanowires to be more predominant in synthesis, and the fabricated nanowire in the [110] to be more stable at smaller diameters [46]. The calculated dielectric functions for these nanowires are compared with the corresponding bulk spectrum.

3.2 Calculational methods

The calculation was carried out for germanium nanowires of various diameters. Starting from a diamond bulk structure, the [110] and [111] oriented nanowires were constructed with dangling bonds saturated with hydrogen atoms [37]. The choice of diameters was made in such a way that the number of dangling bonds are minimized. The diameter, the number of Ge atoms as well as the number of H atoms are summarized in Table 3.1 The radius of a nanowire was given by the distance between the nanowire center and the middle of the peripheral germanium atom and its saturating hydrogen. The periodic boundary condition in the radial direction is maintained by

Table 3.1: Diameter (d)and the number of Ge and H atoms used in the present calculation.

[110]	d (nm)	Ge	H	[111]	d (nm)	Ge	H
	1.25	16	12		1.08	38	30
	1.67	42	20		1.35	62	42
	2.29	72	28		1.81	110	54
	2.71	94	44		2.26	170	66
	3.43	148	52		2.59	218	78
	4.18	234	60		3.03	302	90
	4.37	250	72		3.47	398	102

introducing enough vacuum to remove the interaction among neighboring nanowires. The calculation is based on the density functional theory (DFT) in the local density approximation (LDA). Projector augmented wave (PAW) potentials are used to account for the electron-ion interactions within the the Vienna ab-initio simulation package (VASP)[49]. The energy cutoff for the plane waves is set to 250 eV. The Monkhorst-Pack k-points mesh of $1 \times 1 \times 6$ is used in the geometry optimization. The k-points sampling is increased for the optical property calculations. The optimized lattice constant for germanium is found to be 5.65 Å, in good agreement with the experimental value of 5.64 Å. Quasiparticle energy gaps are computed on the two thinnest nanowires and the bulk using Troullier and Martin norm conserving pseudopotential [50].

3.3 Results and discussion

The band gap energy for germanium nanowires is shown in Fig. 2. Nanowires are studied up to an diameter of 4.4 nm in the [110] direction and 3.5 nm in the [111] direction, respectively. As expected, the gaps decrease as the diameter increases.

The relation between the energy gap and the diameter was fitted with the function $E_g = E_g^{bulk} + ad^{-\alpha}$. Such a fit is naturally suggested by the idea that the change in the gap is induced by the confinement effect. By solving the Schrödinger equation of an electron in an cylindrical infinite potential, the eigenvalues are given by $E_{nl} =$

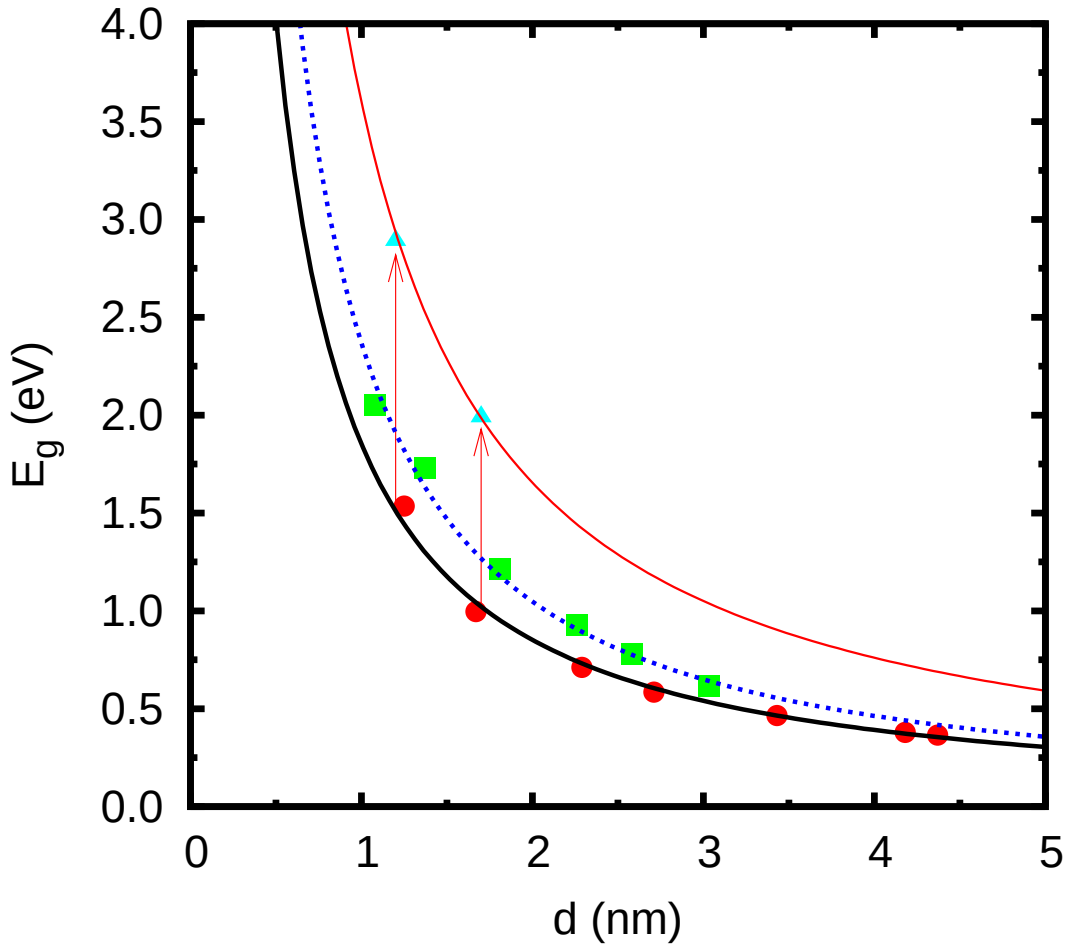

Figure 3.2: The calculated band gaps for the [110] and [111] directions, respectively. The bottom line is for the [110] direction, the middle one is for the [111] direction, while the top one is the quasiparticle results for the [110] direction. The circles, diamonds and rectangles are the computed values. The curves are the best fits using $E_g = E_0 + ad^{-\alpha}$. The fit for the top graph uses the same value of α as the two other curves but with a different value of a.

$\hbar^2\beta_{nl}^2/2m^*r^2$, where β_{nl} are zeros of the Bessel function J_n, m^* the effective mass, and r the diameter of the nanowire. Based on the effective-mass model one expects α to be close to two. However, the best fits result in a value of α to be 1.2 for both directions. This is to be compared with the results for Si nanowires, where α was found to be 1.7 [47]. It is worth noting that for both silicon and germanium, the value is orientation independent. Though these two materials are in the same IV group, germanium nanowires gaps increase slower than silicon nanowire gaps as the diamter decreases.

The qualitative behavior for the quantum size dependence was also observed by Kholod and co-workers [44]. In particular, it was found that the gap is direct in the [110] direction while it is indirect for the [111] direction [44]. This can be interpreted by band folding in the effective mass model. The bulk Ge is an indirect band gap material with its valence band maximum located at the Γ points while the conduction band minimum (CBM) is at the L point. Using band folding in the [111] direction, the Γ point folds to Γ while the L points folds to the nanowire Brillouin zone edge. On the contrary, both the Γ and the L points fold to Γ in the [110] direction. It can also be seen that the gaps for the [110] direction are always lower than those in the [111] direction as observed in Ref. [44].

Since the LDA underestimates the gap, we have performed the GW correction for the bulk and the two thinnest nanowires in the [110] direction. As can be seem from Fig. 2, the GW correction is size dependent. Our calculation shows the GW correction is 0.61 eV for the bulk, 1.31 eV for the thinnest nanowire of diameter 1.25 Å, and 0.89 eV for the nanowire of diameter 1.67 Å. This, along with the observation of the strong size dependence of the GW correction in Si nanowires, indicates that quantum confinement plays an important role in the quasiparticle spectrum.

To describe the absorption spectra of the germanium nanowires, the imaginary part of the dielectric function as a function of frequency is evaluated. To properly

represent the nanowire situation and to eliminate the effect of supercell size, we consider the polarizability per nanowire in units of nm^2. This can be obtained by multiplying the imaginary part of the dielectric susceptibility, $\kappa = (\epsilon - 1)/4\pi$, by the cross-sectional area of the supercell. Therefore,

$$\kappa_2(\omega) = \frac{\pi e^2 \hbar}{m^2 \omega^2} \sum_{ij} \frac{2}{2\pi^3} \int_{BZ} d\mathbf{k} |M_{ij}(\mathbf{k})|^2 \delta[\omega - \omega_{ij}], \tag{3.1}$$

where $M_{ij} =< \psi_j | \hat{\mathbf{e}} \cdot \mathbf{p} | \psi_i >$.

The index i runs over all valence bands while the index j run over all conduction bands for a given value of $\mathbf{k}$. The symbols $\hat{\mathbf{e}}$ and $\mathbf{p}$ stand for the polarization vector and the momentum operator, respectively. The dielectric function for the nanowires along the [111] and [110] directions are calculated using the LDA wavefunctions. The GW correction is then employed to calculate the quasiparticle frequencies. For nanowires along the [111] direction and large [110]-oriented nanowires, we have estimated the GW correction through extrapolating the known results and assumed the same size dependence. The GW correction for [111]-oriented nanowires are thus estimated to be 1.6, 1.2, and 0.8 eV for the three thinnest nanowires along the [111] direction, respectively.

The results are smoothed using a Gaussian broadening of 0.2 eV. Comparing the trend obtained from Figure 3.3 and 3.4 with that in Ref [44], the main features are found to be similar. Some of the differences can be attributed to different broadening used. It is worth noting, however that a larger broadening is necessary in order to avoid unphysical peaks stemming from using discrete k-points.

From the results of the calculated dielectric functions, we realize that the main features of bulk germanium absorptions are present. The four major peaks E_1, $E_1 + \delta$, E_2 and $E_0^{'}$ can be observed, but are shifted towards high energies as expected. Moreover, the spectrum looks bulklike gradually as one moves from the thinnest to the largest nanowire in both directions.

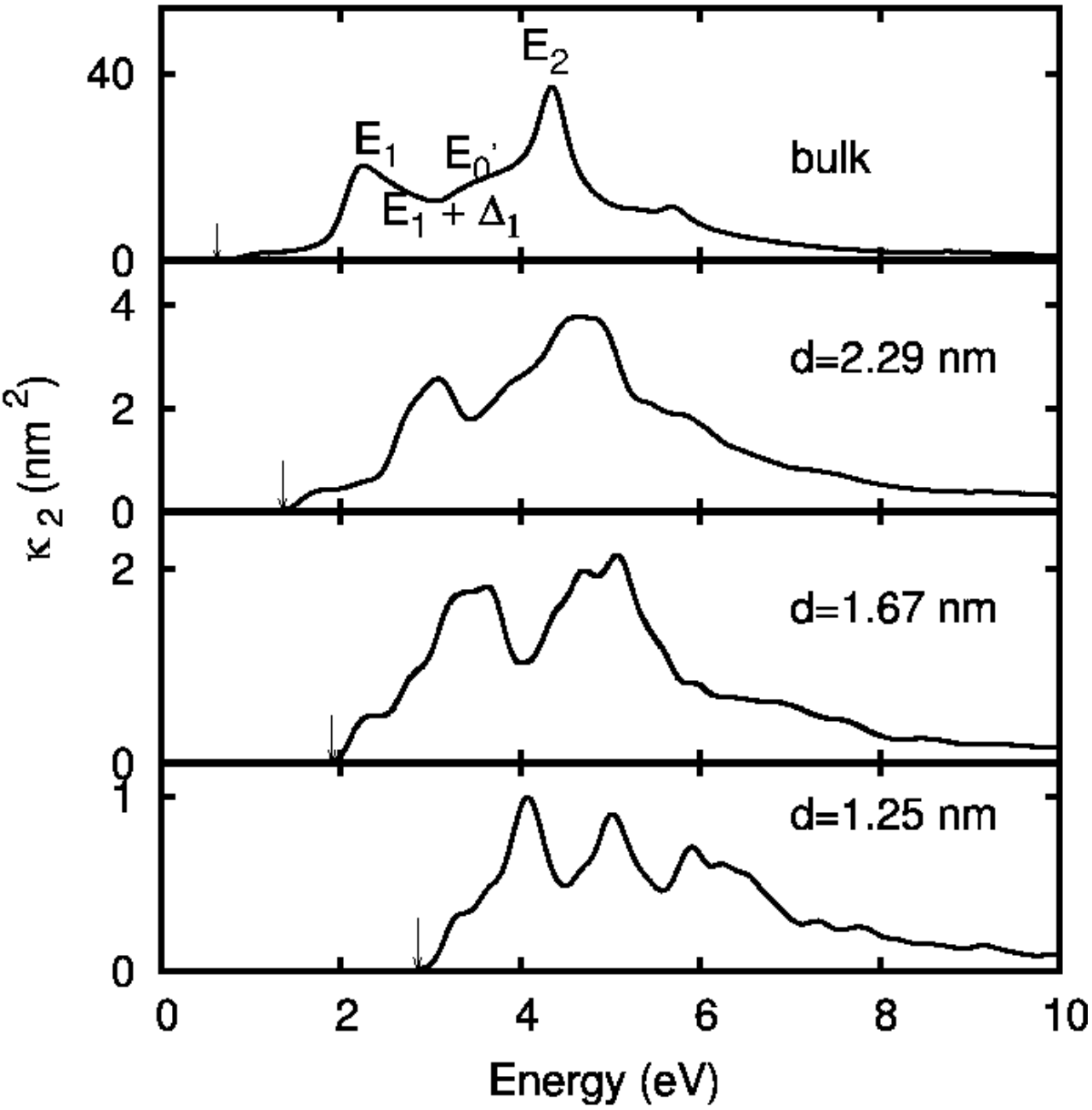

Figure 3.3: Imaginary part of the susceptibility function $\kappa_2(\omega)$ along the nanowire direction for the three thinnest Ge nanowires in the [110] direction and for the bulk (where we present the imaginary part of the dielectric function) . The arrows mark the E_g^{GW} results. On the bulk optical transition, there are four special points known, as $E_1, E_2, E_{0\prime}$ and $E_1 + \Delta_1$. E_1 and E_2 are the two major peak while $E_1 + \delta_1$ is the minimum between E_1 and E_2. $E_{0\prime}$ is a point of inflection found between $E_1 + \Delta_1$ and E_2.

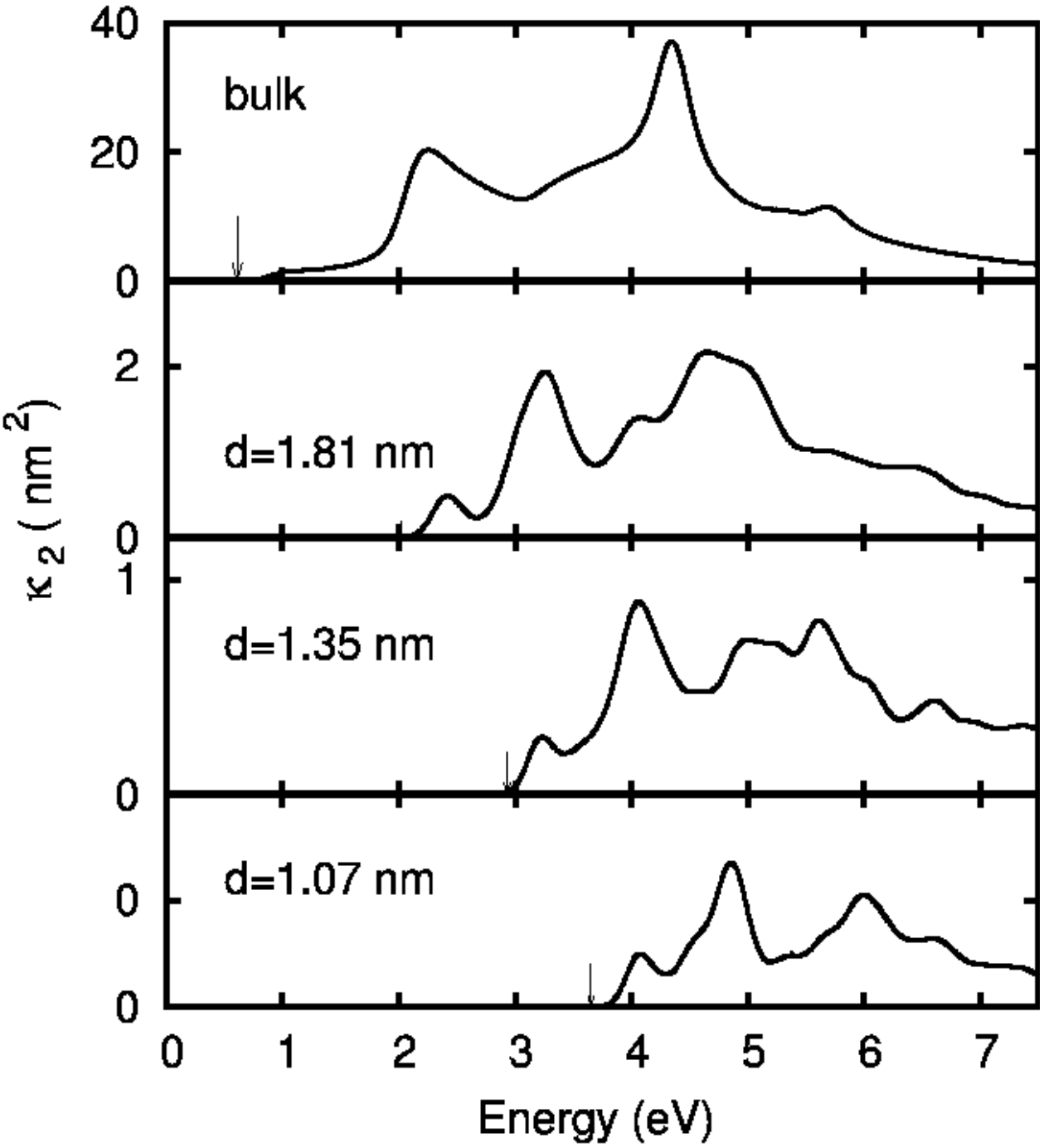

Figure 3.4: Imaginary part of the susceptibility function $\kappa_2(\omega)$ along the nanowire direction for the three thinnest Ge nanowires in the [111] direction (where we present the imaginary part of the dielectric function). The arrows mark the E_g^{GW} results as in the Figure 3.3.

A peculiar feature found in germanium nanowires is the fact that the optical gaps are direct for the germanium nanowire in the [110] direction. For the nanowires in the [111] direction, the difference between the quasiparticle band gaps and the optical transition energies is smaller than 0.2 eV. In contrast, this difference is greater than 1 eV for silicon nanowires in both directions. This shows an unique property of germanium nanowires that the dipole matrix has large amplitude even for transitions at the Γ point responsible for the LDA and quasiparticle direct gap. This result is not intuitive for the [111] nanowires since their electronic gaps are indirect.

Another conclusion from these results is the present of a new peak for the thinnest nanowire in the [110] direction. This peak does not appear for the [111] direction. It is worth mentioning that such new a peak was also observed in a silicon nanowire [47].

3.4 Conclusions

Optical and electronic properties of Ge nanowires have been investigated using the density functional theory in the LDA approximation with GW corrections. Our attention is directed towards a systematic study of the size and directional dependence of the gap. Nanowires in the [110] direction show a direct gap while those in the [111] maintain an indirect gap. A distinctive absorption peak appears for the wire with a diameter of 1.2 nm.

CHAPTER IV

CONFINEMENT AND SURFACE EFFECTS ON ZINC OXIDE AND ALUMINUM NITRIDE NANOWIRES

4.1 Introduction

The formation of surfaces on a crystal can alter physical and chemical properties. In the case of semiconductors, this can be due to the creation of new states in or near the energy gap. When nanowires are created, the surface effect becomes more important as the surface-volume ratio increases. Hence, the confinement effect coupled with the surface effect brings new properties not present in the bulk or in films. In the particular case of semiconducting nanowires, we observe an increase in the bandgap and a shift in the optical spectrum to higher frequencies. One important property that has not been fully checked is the effect of confinement on the polarization and the piezoelectric effect of polar materials on the nanoscale. A recent calculation reported an enhancement of the ZnO piezoelectric constant when compared to three-dimensional materials [51]. Two experiments however have been published showing a decrease of these coefficients for ZnO nanowires [52, 53]. We then decided to compute the piezoelectric coefficients of ZnO and AlN nanowires.

Several reasons motivated the choice of ZnO and AlN as the cases to study. First we wanted nanowires from groups II-VI and III-V since in these groups many materials exhibit the non-centro-symmetric character needed for the piezoelectric effect. In the first group, ZnO is one of the most extensively studied. It is interesting because of its favorable optical, electrical and piezoelectrical properties. It has potential usage in optoelectronics such as photodetectors, light emitting diode, electroluminescence devices, solar cells, and flat cathode ray tubes. Other applications include transparent

UV protection films, chemical sensors varistors, and short wavelength nanolasers [54, 55]. From the III-V group, AlN is also a very interesting material to study. Among the oxides and nitrides, AlN has the highest piezoelectric constant. It also have many potential applications such as in ultraviolet optoelectronic devices, field effect transistors, and electrical packaging materials [56].

In this work, we first review the methods used throughout this project. As a test for the accuracy of the methods and as a foundation for nanowire calculations, we report bulk values such as the lattice parameters or the band structure. We then explain how the construction of the nanowires was carried out. After looking at the charge density of the nanowires, we compute the piezoelectric constant e_{33} for the two smallest nanowires for both materials. Finally, we look at the effect of the piezoelectric field on the nanowire optical properties .

4.2 Methods

Calculations were done using the density functional theory (DFT) in the local density approximation. The interaction between the ions and the electrons was modeled by the projector augmented wave (PAW) method [49]. The calculation of the piezoelectric constants was conducted using the Berry phase technique [57, 58] as discussed in the introduction. The piezoelectric constant e_{33} was given as the slope of the polarization (P_3) as a function of the strain ($\epsilon_{33} = (c - c_0)/c_0$). For Zn, the valence electrons included the ten d electrons and two s electrons. Oxygen had two s and four p electrons while nitrogen has two s and three p electrons. Finally, aluminum had two s electrons and one p electron. Calculations were done using the Vienna Ab -Initio Simulation Package (VASP) [59]. The energy cutoff was set to 400 eV and a k-point mesh of $1 \times 1 \times 6$ was used to relax ions to their ground state. Afterwards a $1 \times 1 \times 10$ mesh was used to get the charge density. Finally the polarization was computed using a $1 \times 1 \times 40$ mesh. For optical properties, we used a $3 \times 3 \times 16$ k-point

mesh and all the meshes included the Γ point.

4.3 Bulk properties

ZnO and AlN are piezoelectric and pyroelectric materials. They belong to the crystal class of C_{6v} with a wurtzite structure. They can be found in high pressure phases in the zincblende or rocksalt structure. The wurtzite lattice vectors in units of the lattice constant a are $\vec{a}_1 = (\frac{1}{2}, \frac{-\sqrt{3}}{2}, 0)$, $\vec{a}_2 = (\frac{1}{2}, \frac{\sqrt{3}}{2}, 0)$ and $\vec{a}_3 = (0, 0, \frac{c}{a})$.The atomic positions given in direct coordinates are $\tau_1 = (\frac{1}{3}, \frac{2}{3}, 0)$, $\vec{\tau}_2 = (\frac{2}{3}, \frac{1}{3}, \frac{1}{2})$, $\vec{\tau}_3 = (\frac{1}{3}, \frac{2}{3}, u)$, $\vec{\tau}_4 = (\frac{2}{3}, \frac{1}{3}, \frac{1}{2} + u)$ where the first two coordinates are of one atomic type and the last two coordinates of another type. The u parameter, which is the distance (in units of c) between the two embedded hexagonal structures is called the internal parameter. It has the information about the separation between two consecutive layers of different atoms. For an ideal wurtzite structure, u is 0.375 and c/a is 1.633. The lattice parameters of these materials are summarized in Table 4.1.

As can be seen from Table 4.1, the value of the internal parameter is always greater than the ideal one . In case of ZnO this parameter is smaller than the experimental result while it is slightly greater in the AlN case. The value of c/a is always lower than the ideal case. As in the case of the internal parameter, the c/a parameter is higher than the experimental value for ZnO and slightly lower for AlN. As expected, LDA underestimates the lattice constants a. The difference between the experimental results and the calculated lattice constant varies between 1.1 % and 1.7 %, which is acceptable in this kind of calculations. Compared to other recent studies on these materials, the bulk parameters are similar to previously reported values. Figure 4.1 shows the band structure of bulk AlN and ZnO . This band structure compares well with previous results [60, 61] computed using other codes. In the low energy range, we observe the two s bands (from oxygen or nitrogen) for both ZnO and AlN. For ZnO, above the s bands are the flat three d bands from Zn. Above them, we see two

Table 4.1: Lattice parameters for ZnO and AlN. First we report the present results and then the experimental values and the previous calculation as found in Refs [63, 64].

	ZnO			AlN		
	Present	*Expt*	*Previous*	*Present*	*Expt*	*Previous*
a	3.20	3.25	3.19	3.08	3.11	3.07
c/a	1.62	1.60	1.62	1.60	1.60	1.60
u	0.38	0.38	0.38	0.38	3.82	0.38

p states filled up to the Fermi energy. The lowest conduction bands are s states. As previously reported [60], we see a small energy difference between the p states and the d bands in ZnO, signaling a strong $p - d$ interaction.

4.4 Passivation of ZnO and AlN nanowires

In this study, we are interested in ZnO and AlN nanowires which are quite ionic compared to other II-VI and III-V materials [62]. When the nanowires are constructed as discussed in the next section, the (100) surfaces are exposed. We review in this section what other researchers have treated this surface in films or in nanowires for both ZnO and AlN.

Many calculation have done on the (100) surface of ZnO. The surface is characterized by Zn-O dimers. Initially, Wander and Harrison [75] computed the surface energy to be 1.16 Jm^{-2}. In the calculation using local basis sets, no passivation was used for the surface and a reconstruction did happen. Similar calculations on the reconstruction of the surface [65, 66] have been done with no passivation.

Filippetti *et al.* did similar calculations for both ZnO and AlN using no passivation [62]. They concluded that AlN and ZnO are highly ionic with cation charge being transfered to the anion. We should note however that a study of the AlN (001) surface with the dangling bonds saturated with fictitious H atoms with charges of 5/4 and 3/4 in order to avoid unphysical charge transfer between the two ends of the surface [67]. The use of fictitious H has also been reported in quantum dot simulations for

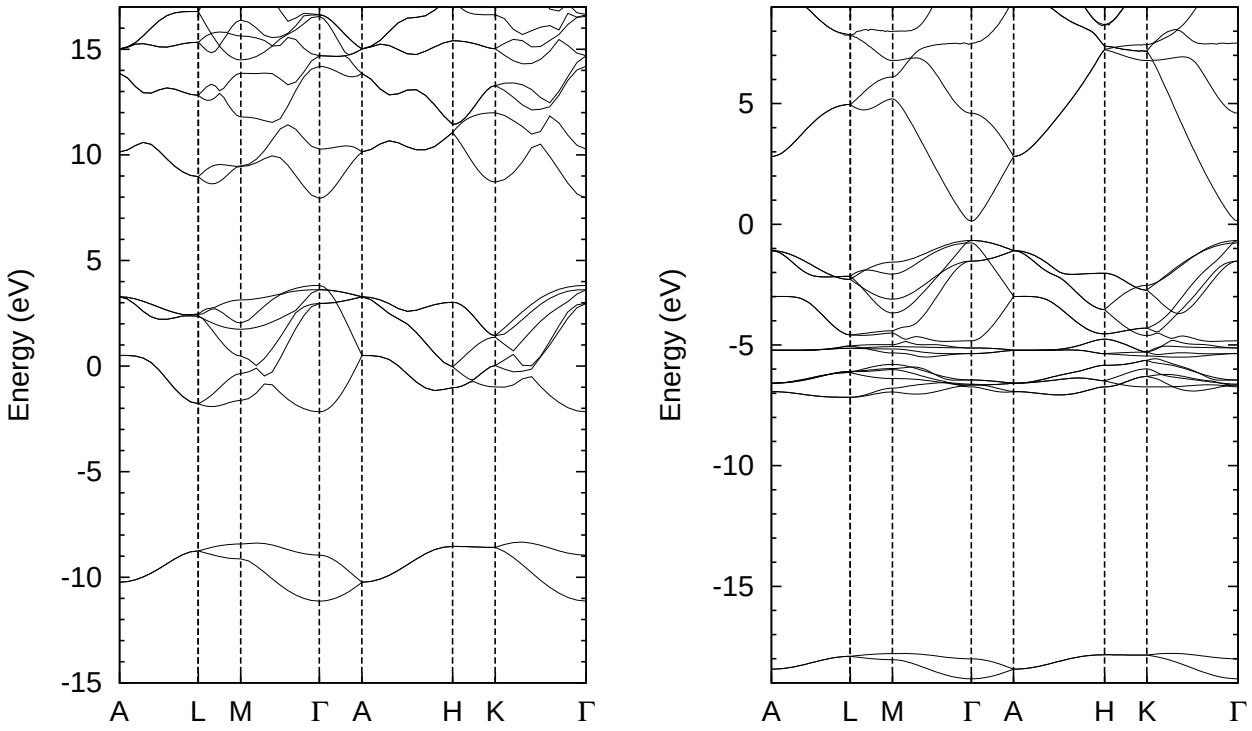

Figure 4.1: The band structure of bulk AlN (left panel) and ZnO (right panel) along the main symmetry points.

AlN and ZnO semiconductors [54]. The charges of 1/2, 3/4, 1, 5/4 and 3/2 were considered to be the ideal passivation. Nevertheless another paper discussing the elastic piezoelectric and optical properties of GaN/AlN quantum dots did not include any passivation [68]. Even in nanowire calculations, no general rule is being followed. Some studies on III-V nanowires were performed with passivation by atomic hydrogen on both Al and N [69]. A paper by Kentero and others [70] discusses the electronic structure of GaN and AlN nanowires. In that paper, no passivation is considered.

Because of the lack of consistency in the literature, we will do our calculation using both passivated and unpassivated nanowires. In the following calculations we will conclude that passivation is very important if we want to get the electronic properties of these nanowires.

4.5 Nanowire structure

The nanowires were constructed by creating a truncated bulk wurtzite structure along the (001) direction with a chosen diameter. The center of the nanowire was chosen in two ways. The first choice was to the take it at the center of the triangles that makes these hexagonal type structures (Type I nanowire). The other way (which is more natural) was to set it at an atom site (Type II nanowire). The configuration of the smallest nanowire for each type is shown on Figure 4.2. The coordinates of the cross section of the nanowire in Figure 4.2 (Type 1) in unit the lattice constant a are (0,0), (1,0), (0, $\sqrt{}$(3)/3),(1, $\sqrt{}$(3)/3), (1/2, $\sqrt{}$(3)/2) and (1/2, -$\sqrt{}$(3)/6). The diameter of the nanowire was chosen in a such a way that no more than one "dangling bond " was created.

When nanowires were allowed to relax to their energy minimum configuration, there is a change in their nearest neighbor's distance. We found that the nearest neighbor for bulk AlN and ZnO is 1.87 $\mathring{A}$ and 1.94 $\mathring{A}$, respectively. When passivation was applied, this values does not change much; it becomes 1.86 $\mathring{A}$ and 1.93 $\mathring{A}$. The

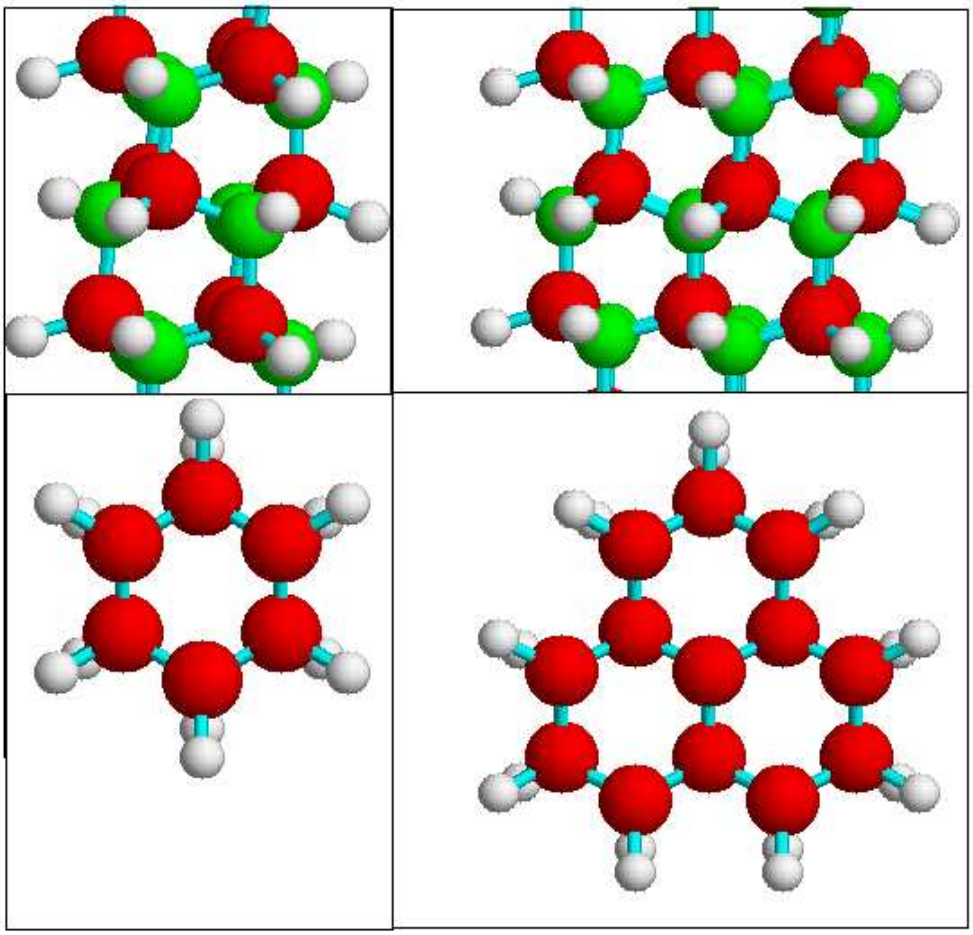

Figure 4.2: The ball-and-stick model of the ZnO and AlN nanowires. The top graphs are the side view while the bottom graphs are the top view. The graphs on the left is the smallest NW of Type I while the one on the right is the smallest nanowire of Type II. The red (dark) atoms are the metals (Zn or Al) while the green (light) ones are the non-metal (O or N).
These nanowires are passivated by hydrogen (small spheres).

Al-H distance was found to be 1.59 $\mathring{A}$ while the N-H was 1.08 $\mathring{A}$. For the ZnO case, the situation is almost identical. The Zn-H length was found to be 1.60 $\mathring{A}$ and the O-H length is 1.07 $\mathring{A}$. This O-H distance is close to the water bond length which is about 0.96 $\mathring{A}$. The reason our value is a little bit higher may be due to the fact that we do not have a perfect hydrogen (the charge is different from the atomic hydrogen). Moreover, the passivating hydrogen atoms in the nanowires have only one nearest neighbor. The unpassivated nanowires undergo reconstructions with a shortening of their nearest neighbors distance. For the nanowire of Type I previously discussed, every atom has a coordination number of three. One of the three atoms is directly above or below the atom with the same x and y coordinates. After relaxation, we realize that the distance from that special atom is the most shortened. In particular, this distance is 1.80 $\mathring{A}$ for AlN while its is 1.86 $\mathring{A}$ for ZnO nanowires. The distance with the other two neighbors is 1.83 $\mathring{A}$ for AlN and 1.90 $\mathring{A}$ for ZnO respectively. On the other hand, we realize that the reconstruction causes the atoms to shift towards the center of the nanowire. Though all the atoms shift towards the center, the metal atoms move more (9.7 - 12.1 % of the bulk lattice constant) while the non-metal atoms barely move (1.0-1.3 %), the first number being for AlN and the second number for ZnO. This change in diameter causes the internal parameter to adjust accordingly. The largest adjustment happens for ZnO where u decreases about 6 %. The change for AlN is negligible. These changes seem to increase as the ionicity increases.

4.6 Band gap

We computed the band gaps in the ZnO and AlN nanowires and compared them with bulk values. As seen in Figure 4.1, bulk ZnO and AlN display a direct band gap at the Γ point. Due to band folding, the gap of nanowires is expected to remain direct. The band gap results are summarized in Table 4.2. The gaps were computed as the difference between the eigenvalues (at the Γ point) of the last occupied orbital and

Table 4.2: Band gaps for ZnO and AlN nanowires and bulk. NP and P stand respectively for non-passivated and passivated nanowires. The second column provides the number of Zn(Al) and O(N) used for each type of nanowires. The fourth column is the number of hydrogen atoms used to passivate the wire per supercell. An estimate of the diameter of the nanowire is also provided (the first number is for ZnO nanowires while the second is for AlN nanowires). Finally, the band gap is given for each type of nanowires.

	# Zn(Al)	# O(N)	# H	d(nm)	ZnO gap		AlN gap	
					NP	P	NP	P
Type I	6	6	12	0.35/0.37	1.98 eV	4.32 eV	2.27 eV	5.59 eV
Type II	13	13	18	0.70/0.73	1.67eV	3.03 eV	2.37 eV	5.59 eV
Bulk					0.8eV	—	4.52 eV	—

the first unoccupied orbital. We did not take into consideration the fact that some were surface or dangling bond states.

Many conclusions can be inferred from the results in Table 4.2. First, we see that passivated as well as unpassivated nanowires are all semiconductors as were the bulk materials. This contrasts with the results of Si nanowires where unpassivated nanowires along the (100) direction show metallic and semi-metallic characteristics [73]. This characteristic is very useful for many technological applications. Second, the band gap of passivated nanowires is greater than the bulk gap as expected. This is due to the quantum confinement effect that shifts the energies. Since passivation removes the surface states in the gap, the opening of the gap becomes an intrinsic property. We normally expect the gap to increase as the diameter decreases. This could be seen in case of ZnO where the small nanowire of Type I has a higher band gap than the Type II nanowire. Though it is not the case for AlN nanowires, this can be understood since the two types of nanowires are structurely different. The case of reconstructed nanowires is more interesting. Though we know that surface states are most likely going to appear in these results, ZnO nanowires gap are still higher than the small bulk value. And again, the gaps increases as the diameter decreases. This is interesting since we can see that confinement effect on the gap is

still visible even without any passivation. The case of AlN is different and behaves as Si nanowires where the gaps are lower than the bulk values. The difference between the two semiconductors may be due to the difference in ionicity. We know indeed that ZnO, which is a II-VI material, is more ionic than AlN from the III-V group. The more ionic a material is, the less it forms dangling bonds.

In order to analyze the states that are in presence, we plotted the band structure of the AlN nanowire and the projected bandstructure of the bulk. In order to do so, we first computed the energy eigenstates for the bulk with a dense k-point mesh without any symmetry included. We obtained a $20 \times 20 \times 10$ grid for which energy eigenstates were obtained. We then plotted for each k_z all the energies from the lowest to the highest. They formed an almost continuous function for some energy range with jumps at some particular points. This gave us the projection of the bulk states in the (001) direction. Afterwards, we plotted the energy eigenvalues of the AlN nanowire both with H passivation and without. Results are reported in Figures 4.3 and 4.4. The eigenvalues are shifted so that the projected bulk energies coincide with those of the nanowire at the lowest end of the spectrum. By looking at Figures 4.3 and 4.4, we see that nanowire energies fall within the bulk band projection for occupied states whether nanowire are passivated or not. The situation changes for unoccupied states. We see that only passivated nanowire states fall within the band projection while the bottom of the conduction bands for unpassivated nanowires falls outside the bulk projection. This is a good indication that passivation makes a significant difference in these nanowires.

We tried to align eigenvalues for passivated and unpassivated nanowire. This is possible because we can set zero energies at the vacuum level. For that purpose, we computed the local potential for the nanowire and shifted the energies by the vacuum local potential. Looking at the energies, we realize that the energies are shifted to lower values when passivation is applied. At the Γ point, the lowest energy state for

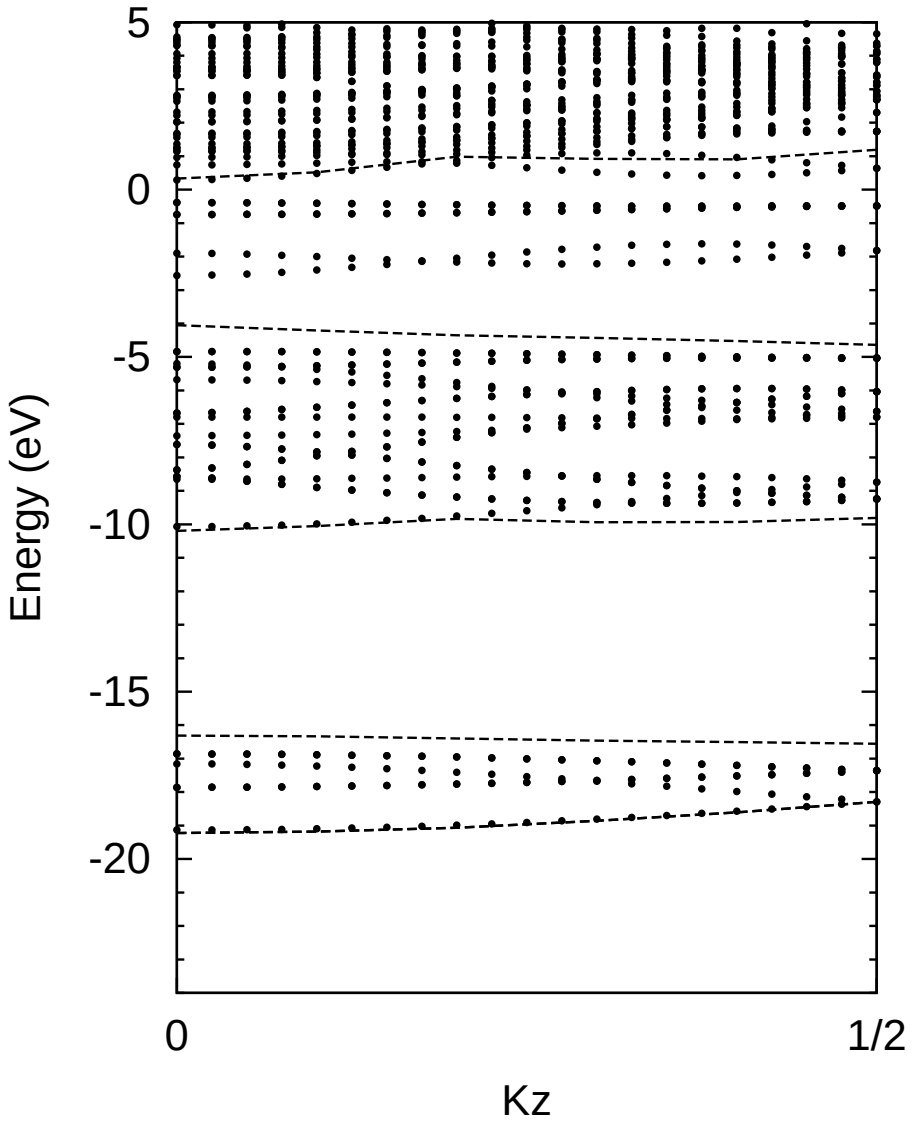

Figure 4.3: The AlN bulk band structure projected on the (001) nanowire direction compared with the AlN Type I unpassivated nanowire band structure. The nanowire eigenvalues were shifted so as to match the bulk and the nanowire at the energy minimum at the Γ point. The eigenstates outside the bulk projection are surface states.

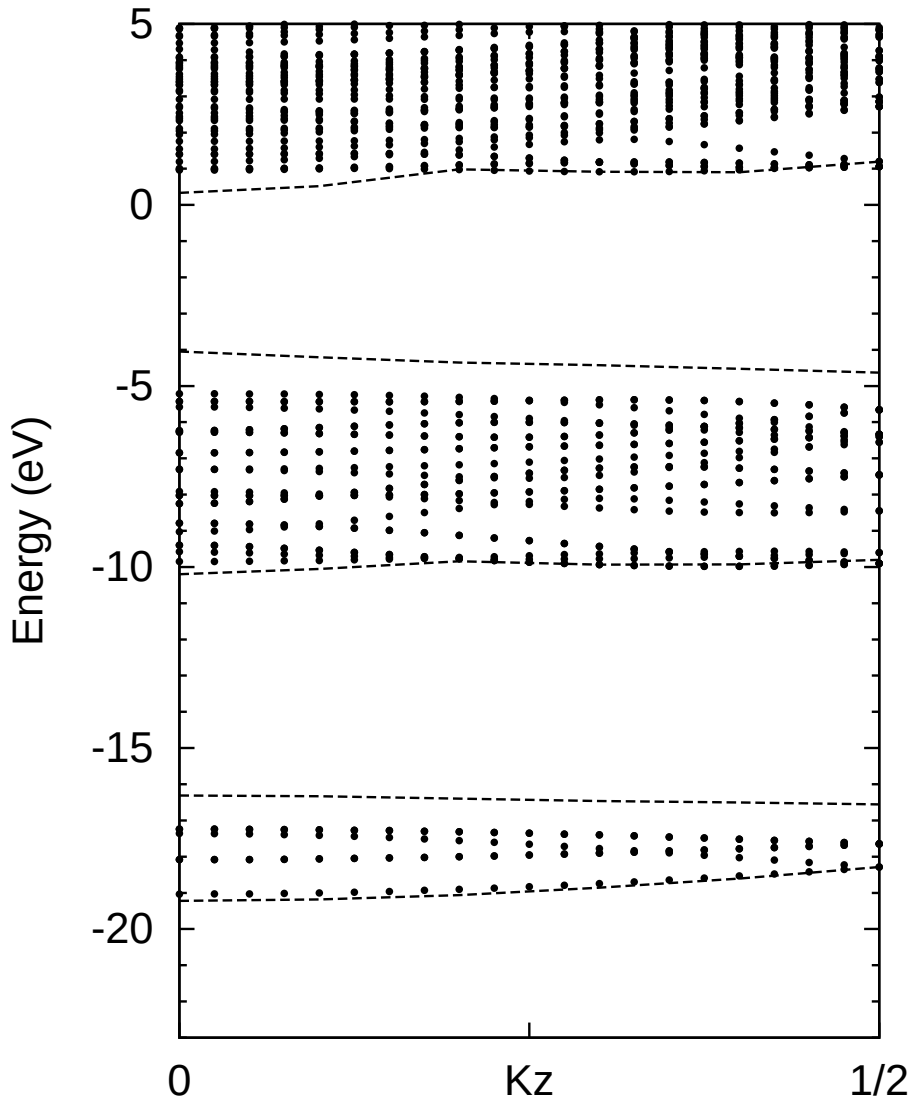

Figure 4.4: The AlN bulk band structure projected on the (001) nanowire direction compared with the AlN Type I passivated nanowire band structure. The nanowire eigenvalues were shifted so as to match the bulk and the nanowire at the energy minimum at the Γ point.

the passivated nanowire is 0.8 eV lower than the unpassivated counterpart. Moreover, the work function for the passivated nanowire is 6.9 eV compared to 5.7 eV for the unpassivated counterpart. These values are of course higher than bulk work function which varies between 3.9 ev to 5.35 eV [71].

4.7 Charge density

We know that ZnO and AlN are ionic materials. Since ZnO is more ionic that AlN, we show in Figure 4.6 the charge density. In order to get these charge densities, we used a conventional unit cell so that the axis can be perpendicular. As mentioned, the lattice vectors in units of the lattice constant a are given by $\vec{a}_1 = (1, 0, 0)$, $\vec{a}_2 = (0, \sqrt{3}, 0)$,$\vec{a}_3 = (0, 0, \frac{c}{a})$. The coordinates of the Al atoms are given by $\tau_1 = (0, 0, 0)$, $\tau_2 = (1/2, 1/2, 0)$, $\tau_3 = (0, 1/3, 1/2)$, $\tau_3 = (1/2, 5/6, 1/2)$. The anion coordinates are the same, except that there is a (0,0,u) translation where u is is around 0.380 for AlN and ZnO. Looking at this unit cell, we see that any plane perpendicular to c axis that passes through a cation atom will also contain an anion. For that purpose, we plotted a cross section plane given by x = 0. Such a plane passes through τ_1 and τ_3 and their anions counterparts. We plotted the charge density at the Γ point for all bands but only reported a few of graphs. The first few bands are nitrogen s states followed by p states up to the top of the valence band. The first unoccupied state is also a nitrogen s state. Another important fact is how there is no charge around the Al atom. This confirms the fact that AlN and ZnO are very ionic materials.

We used the same concept to plot the charge density for AlN nanowire with 12 atoms (6 Al and 6 N). For this reason we do have 24 occupied bands for the unpassivated nanowire and 30 bands for the passivated one. For the unpassivated nanowire, we first get 6 s states followed by 18 nitrogen p states. We paid attention to the last 5 occupied orbitals for the unpassivated nanowire and found out that they were very asymmetric. They look like p states but with the charge density being

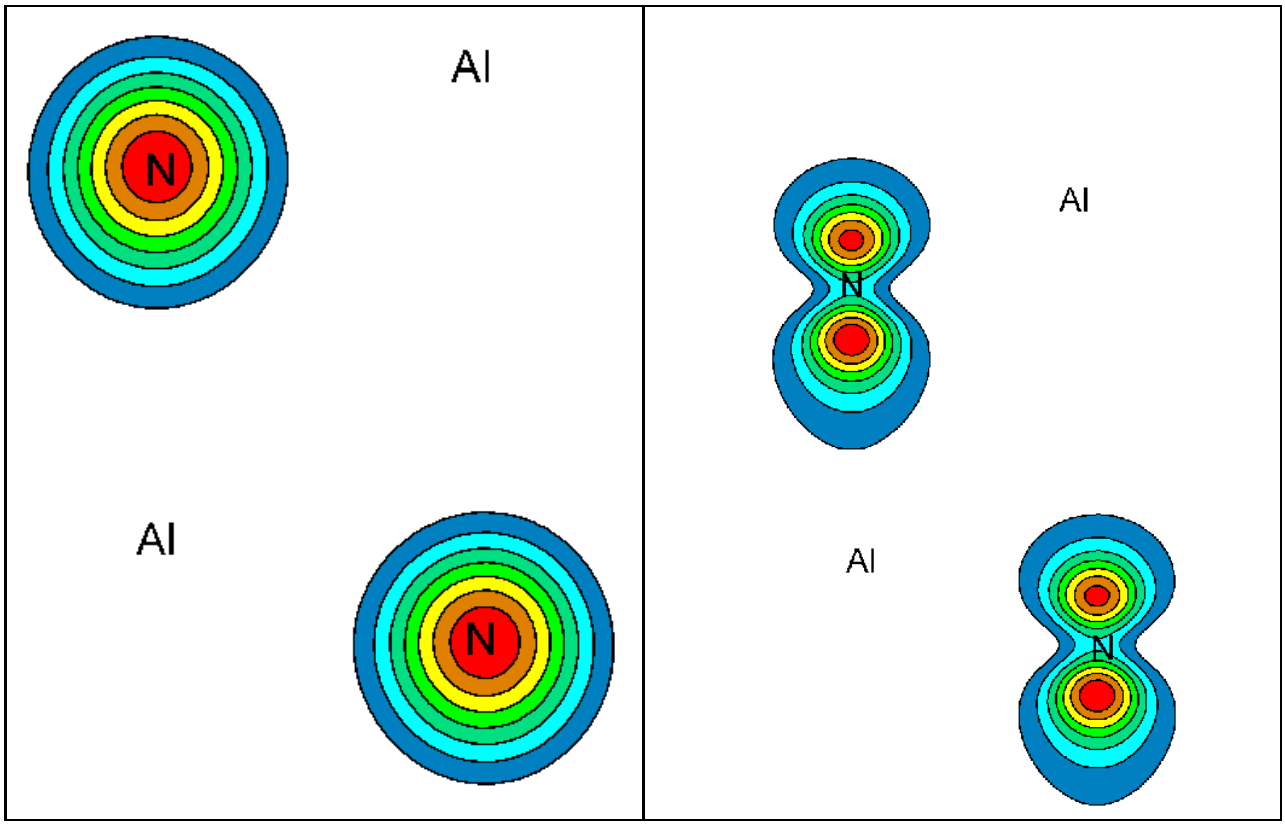

Figure 4.5: Bulk charge density for AlN first band(left panel), and the top of the valence band (right panel) The View is along the (010) plane with no shift. We used a conventional cell with $\vec{a}_1 = (1, 0, 0)$, $\vec{a}_2 = (0, \sqrt{3}, 0)$,$\vec{a}_3 = (0, 0, \frac{c}{a})$ with 4 Al and 4 N atom per unit cell.

concentrated in one part of the state. We showed in Figure 4.7 the difference between the last occupied orbital for passivated and unpassivated nanowire. We realize that the asymmetry is the same for AlN and ZnO orbitals. This shows how not passivating nanowire changes dramatically the occupied states. We also tried to locate states for the passivated nanowire. We first saw nitrogen s states as in case of unpassivated nanowire. Afterwards came H states and nitrogen p states until the the 20^{th} band and then only nitrogen p states are present until the top of the valence band. All the H states are nitrogen neighbors(H with 1.25 electrons).

In conclusion, we saw first how passivation for AlN and ZnO nanowires or films is often neglected. By analyzing the band gap, the charge density and the band structure, we can tell that passivation is necessary and should be used if one want to get accurate electronic structure of this ionic material.

4.8 Piezoelectric constant results

One of the major property of ZnO and AlN is their big piezoelectric constant compared to other wurtzite materials. In particular, ZnO nanowires are of great interest in fabricating nanogenerators able to power nanomaterials. As discussed in the theory chapter, the piezoelectric constant is defined as the ratio between the polarization and the strain or stress in the linear regime(small strain or tress). Figure 4.7 shows how the polarization is linear as a function of stress. The slope was considered to be the piezoelectric constant e_{33}. In the calculation, the change in the polarization is defined by two terms: a electronic part and an ionic part given by:

$$P_{el}(\lambda) = \frac{-ie}{(2\pi)^3} \sum_n \int_{BZ} d\mathbf{k} < u_{\lambda,nk} | \nabla_{\mathbf{k}} | u_{\lambda,nk} > \tag{4.1}$$

$$\Delta P_{ion} = \sum_i \frac{|e| Z_i C_i}{\Omega} \tag{4.2}$$

where $u_{\lambda,nk}$ is the periodic part of the Bloch wave function, z is the valence of ion i, C_i is the z coordinate of ion i, and Ω the volume of the unit cell. In our case, λ is

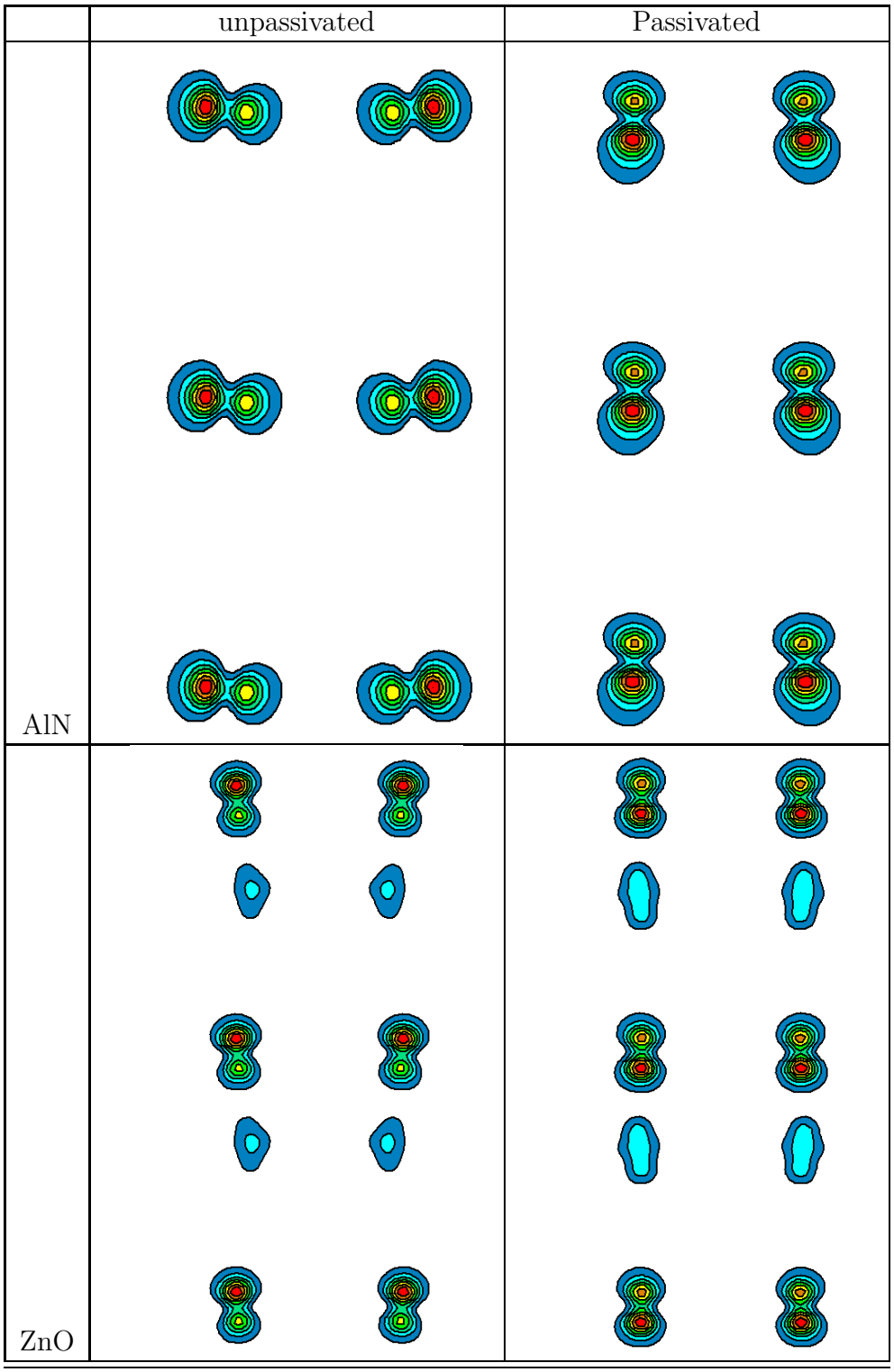

Figure 4.6: Side view of the charge density (using only the Γ point) at the highest occupied molecular orbital (HOMO) for the passivated and unpassivated smallest nanowire. The plotted plane is parallel to the nanowire and passes through the atoms with (0,0,0) and (0,1,0) coordinates.

the same as the stress or strain ϵ_{33}.

We use this technique to compute the piezoelectric properties of ZnO and AlN bulk as reported in Table 4.3. Because a nanowire is a one dimension object, we computed the polarization (which is usually the dipole moment per unit volume) as the dipole moment per ion pair. For the bulk material, a value of 2.9 means a piezoelectric constant of 1.33 C/m^2 and for AlN the coefficient is equal to 1.74 C/m^2. These results are close to experimental results. From experiment, zinc oxide bulk piezoelectric constant is $1.32C/m^2$ while the film piezoelectric e_{33} constant is $1.22C/m^2$ [67]. For aluminum nitride, the experimental value is $1.57C/m^2$ for bulk while the film value is $1.55C/m^2$. Previous DFT calculations using ultrasoft pseudopotentials also give close results. For ZnO, and AlN, $0.89C/m^2$ and $1.46C/m^2$ were computed respectively as the bulk piezoelectric constants. [77]. As the same concept was used for the nanowires, we expect comparable accuracy. Passivated and unpassivated nanowires were relaxed and the polarization was computed at different stresses or strains up to 1%. The piezoelectric constant was computed for both the passivated and the unpassivated nanowires.

The results summarized in Table 4.3 show how passivated nanowires have a lower piezoelectric constant than the bulk while free standing nanowires have a higher coefficient. Apart from this general trend, a breakdown for this contribution is also given . We know that indeed the polarization has an ionic and an electronic component. From these results, we realize that the two contributions have opposite signs with the positive term being always dominant. From the table, it is obvious that for ZnO, the ionic term dominates while the electronic term is dominant in AlN. It is also interesting to see that though the confinement effect changes the values of different contributions, it does not change their signs (except for AlN where the value is close to zero but positive). This is also true for passivation which does not change the dominant term for any nanowire.

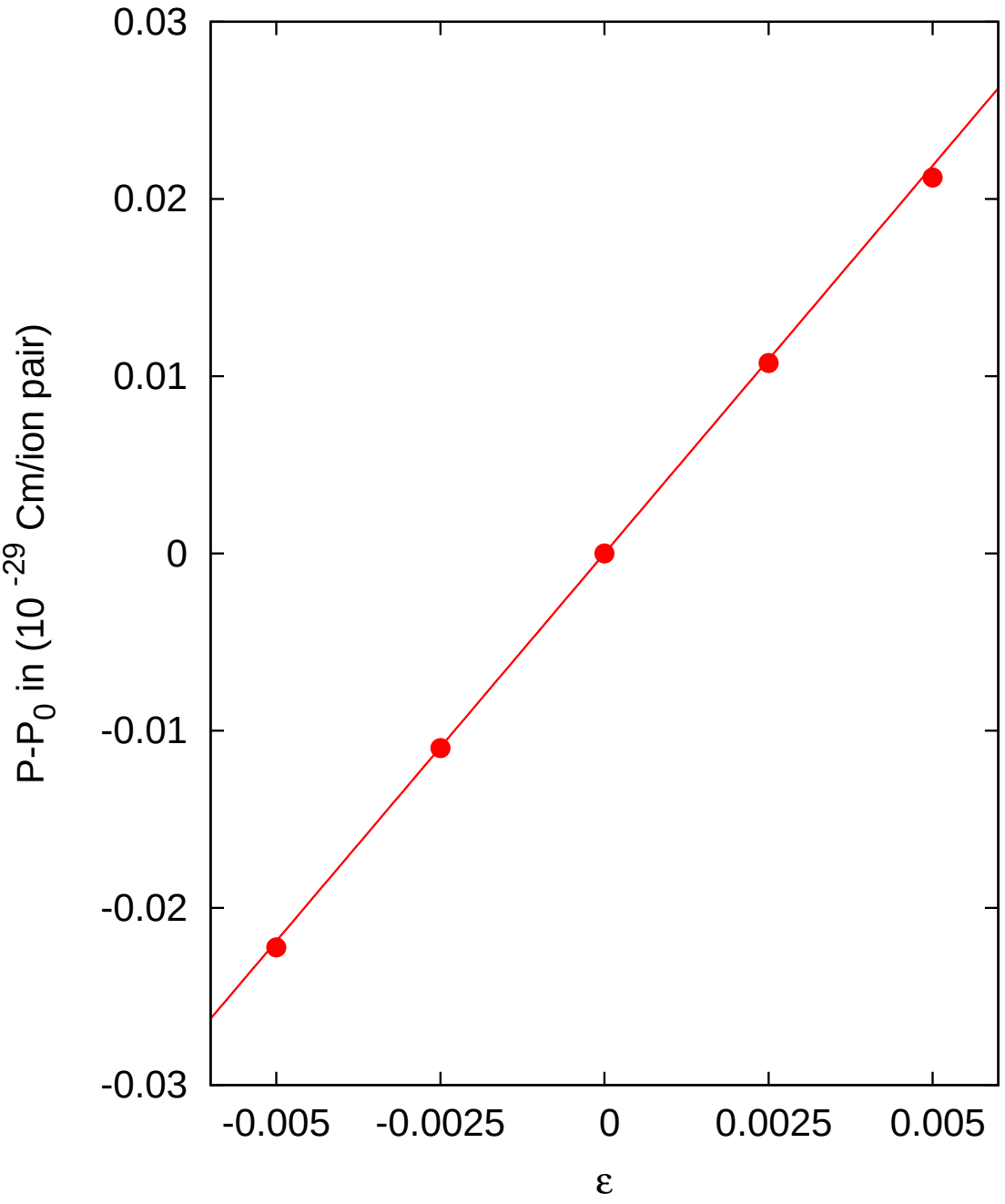

Figure 4.7: Change in polarization as a function of the strain ϵ for the unpassivated ZnO nanowire of Type II The slope give the piezoelectric constant.

Table 4.3: Calculated piezoelectric coefficient e_{33}^* for ZnO and AlN nanowires in units of 10^{-29} C m/ionic pair. It's electronic and ionic contributions are also given. As before P and NP stand for passivated and non-passivated. NP* is the non passivated nanowire but using the atomic coordinates of the passivated nanowires. . H* is the "nanotube" made of the passivating hydrogen. The ionic contribution of NP* and H* gives the contribution of passivated nanowires.

		ZnO			AlN		
		Electronic	Ionic	Total	Electronic	Ionic	Total
	Bulk	-3.3	6.2	**2.9**	5.1	-1.6	**3.5**
Type II	NP	-4.3	8.7	**4.4**	8.3	-2.4	**5.9**
	P	-8.5	10.6	**2.1**	2.7	0.1	**2.8**
	NP*	-4.4	9.1	4.7	6.6	-0.3	6.3
	H*	-6.1	1.6	-4.5	-7.7	0.5	-7.2
Type I	NP	-4.4	9.1	**4.7**	9.2	-2.6	**6.6**
	P	-9.2	10.3	**1.1**	2.3	0.3	**2.6**
	NP*	-2.4	6.7	4.3	7.7	-0.6	7.1
	H*	-8.2	3.5	-4.7	-11.7	1.0	-10.7

When we monitor the change that comes from passivation, we realize that passivating nanowires increase the ionic term while decreasing the electronic term. Another major conclusion from this Table 4.4 is the low value of the ionic contribution for AlN nanowires and bulk. This fact implies that when AlN is under stress, it does not modify much of its internal parameter u. On the other hand, ZnO reacts to a change of its lattice constant by changing its internal parameter. This is also true for the effect of confinement in the lateral direction. ZnO reacts by decreasing its internal parameter when the lattice constant in the direction of the wire is maintained at its bulk value.

In order to determine if reconstruction is responsible of these changes, we computed the piezoelectric constant of ZnO and AlN in the unreconstructed structure (NP*). This means that we took the coordinates of ZnO (AlN) from the structure of the relaxed and passivated ZnO(AlN) and removed the fictitious Hydrogens. Comparing unpassivated (and reconstructed) nanowires results and this NP* structure

results, we conclude that reconstruction has a little effect on the piezoelectric coefficients. The differences between the two columns varies between 0.3 and 0.5 $10^{-29}C/m$ per ion pair. This is obviously insignificant and can not be the cause of the change induced by passivation.

The only remaining cause of the change of piezoelectric constant due to passivation is the presence of fictitious hydrogen atoms. Even if these hydrogen atoms would give up their electrons to the nanowire, their ions arranged in a non centro-symmetric have a significant ionic polarization. That is why we computed the values of e_{33} using the hydrogen coordinates only obtained from the passived structures. Table 4.3 shows how their electronic contribution are negative while their ionic contribution is positive. As we see, the total hydrogen contribution is negative and lower than the unpassivated nanowire coefficients. This tells us that the small value of the passivated nanowire coefficients is due to the presence of these surface impurities.

In conclusion, we realize that non-passivated nanowires have a higher piezoelectric values while the passivated nanowire have low coefficients. We found out that the fictitious hydrogen atoms are the most responsible of the low piezoelectric coefficient. Therefore, pure nanowire should have a high piezoelectric response while contaminated nanowire could have a low piezoelectric coefficient (compared to bulk values).

4.9 Discussion on piezoelectric results

In the previous paragraph, we obtained the piezoelectric constants as obtained from the calculation. It is worth comparing them with recent experiments especially for ZnO nanowires. Before reporting these experimental results, we would mention that experiments do not generally report the value of e_{33}. Instead, they measure d_{33} which is also a piezoelectric constant but Which is the ratio of the electric field as a function of strain or stress. But as suggested by Bernardini *et al.* [64], it is possible

to compute d_{ij} coefficients from the knowledge of the e piezoelectric constants and of the elastic stiffness constants at constant electric fields C_{ij}. The relation is given by $e_{ij} = \sum_k d_{ik}C_{kj}$. The d_{33} value for ZnO bulk in the [001] direction has been measured to be 12.4 pm/V [78] or 9.93 pm/V [79].

Two recent experiments were done to find the piezoelectric constant d_{33} for ZnO nanorods. The first one was done on ZnO nanorods of 300 nm of diameter and $2\mu m$ of length [52]. The nanorods direction was confirmed to be in the [001] direction. The average piezoelectric constant was found to be 7.5 pm/V which is lower than bulk values. A second experiment had even a lower piezoelectric constant [53]. The group measured the coefficient for 198 nanorods and recorded their average coefficient.It was found to be 4.41 pm/V with a standard deviation of 1.73 pm/V.

As it can be seen from these experiments, we realize that the piezoelectric constant is lower than the bulks as nanorods will have impurities on the surface either through fabrication or through exposure to air. After our calculations were ended, we learned of an independent calculation of the piezoelectric constant of free standing ZnO nanowires [51]. Their coefficients were higher than the bulk as it is for our calculations. We, therefore, conclude that if there was a way to keep these nanowires free of impurity, their coefficients would be higher than the bulk; otherwise, their coefficient will be lower and the voltage expected from these nanogenerators would be low.

4.10 Effect of piezoelectric field on optical properties

It has been observed that optical transitions of piezoelectric materials shift when they are under stress or strain. Specifically, when under stress, these materials manifest a shift towards higher frequencies [80]. While this phenomenon has been observed for bulk materials, it has been reported more on quantum dots. We then became interested in finding out the role of dimension in this optical shift.

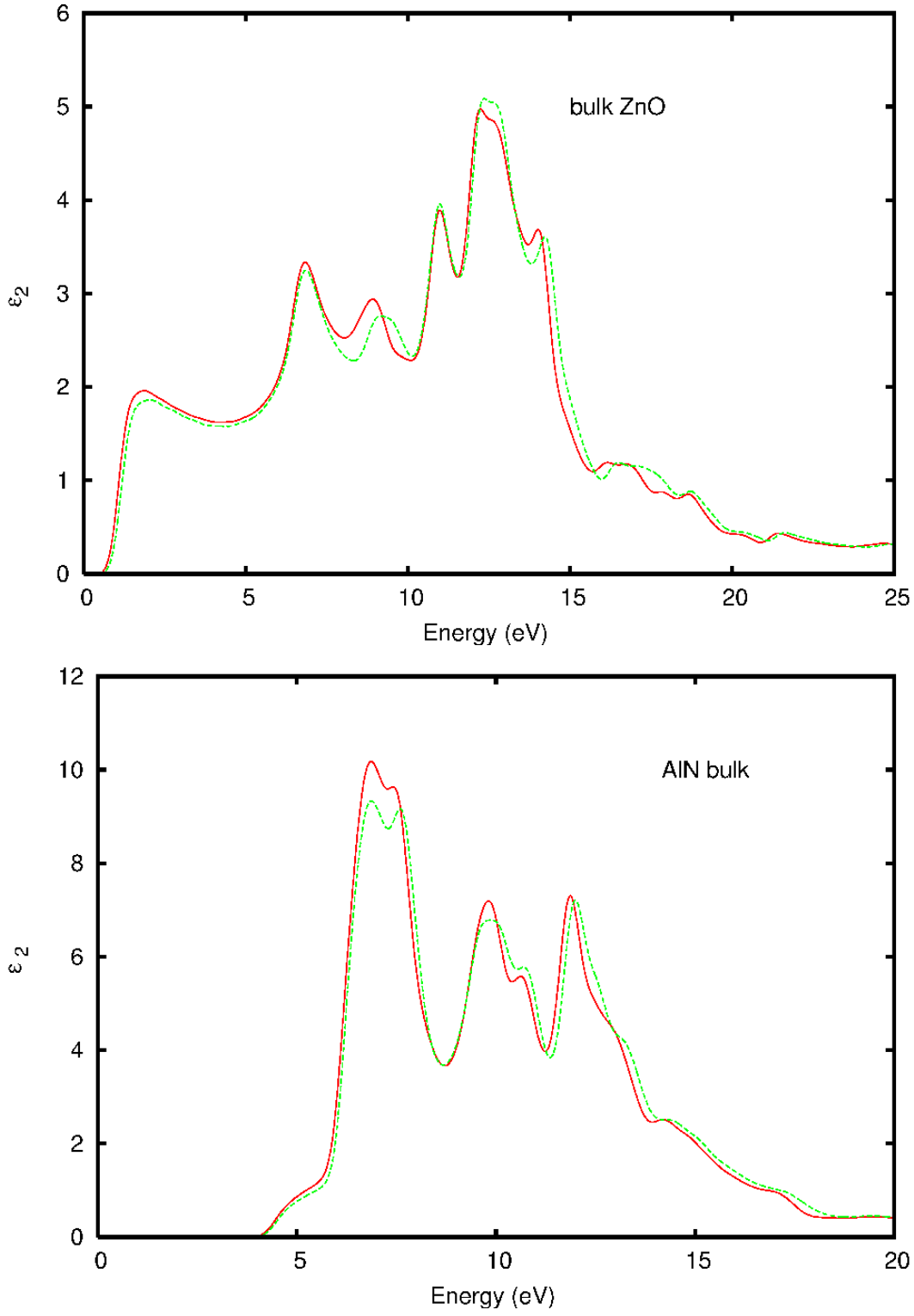

Figure 4.8: Imaginary part of the dielectric function for Zno and AlN bulk. The solid line is for the unstrained structure while the dashed line is for the structure under 2 % strain.

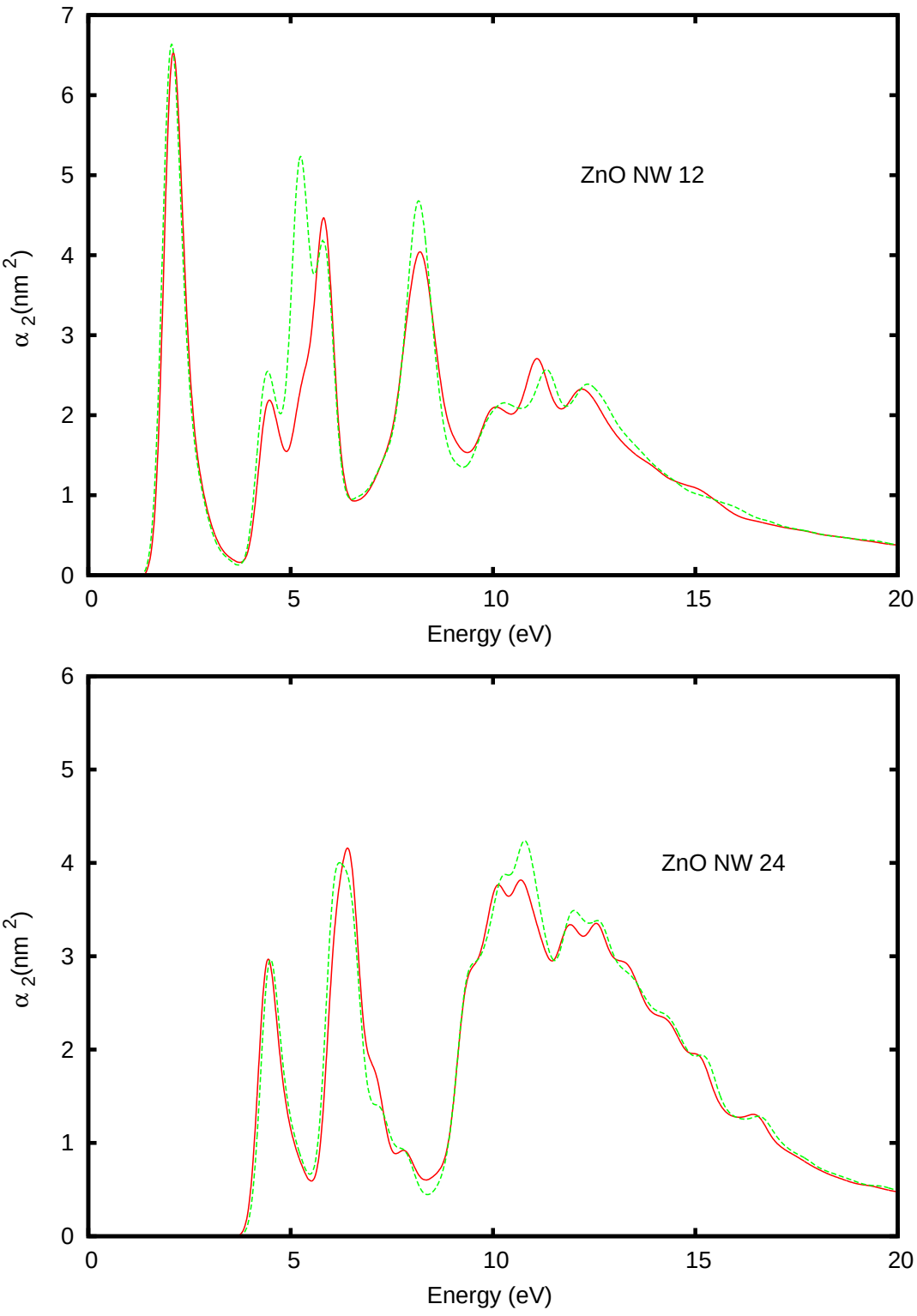

Figure 4.9: Imaginary part of the polarizability function for the smallest ZnO nanowire Type I. The top graph is for the unpassivated nanowire while the bottom graph is for the passivated nanowire. The solid curve is for the unstrained structure while the dashed curve is for the structure under 2 % strain.

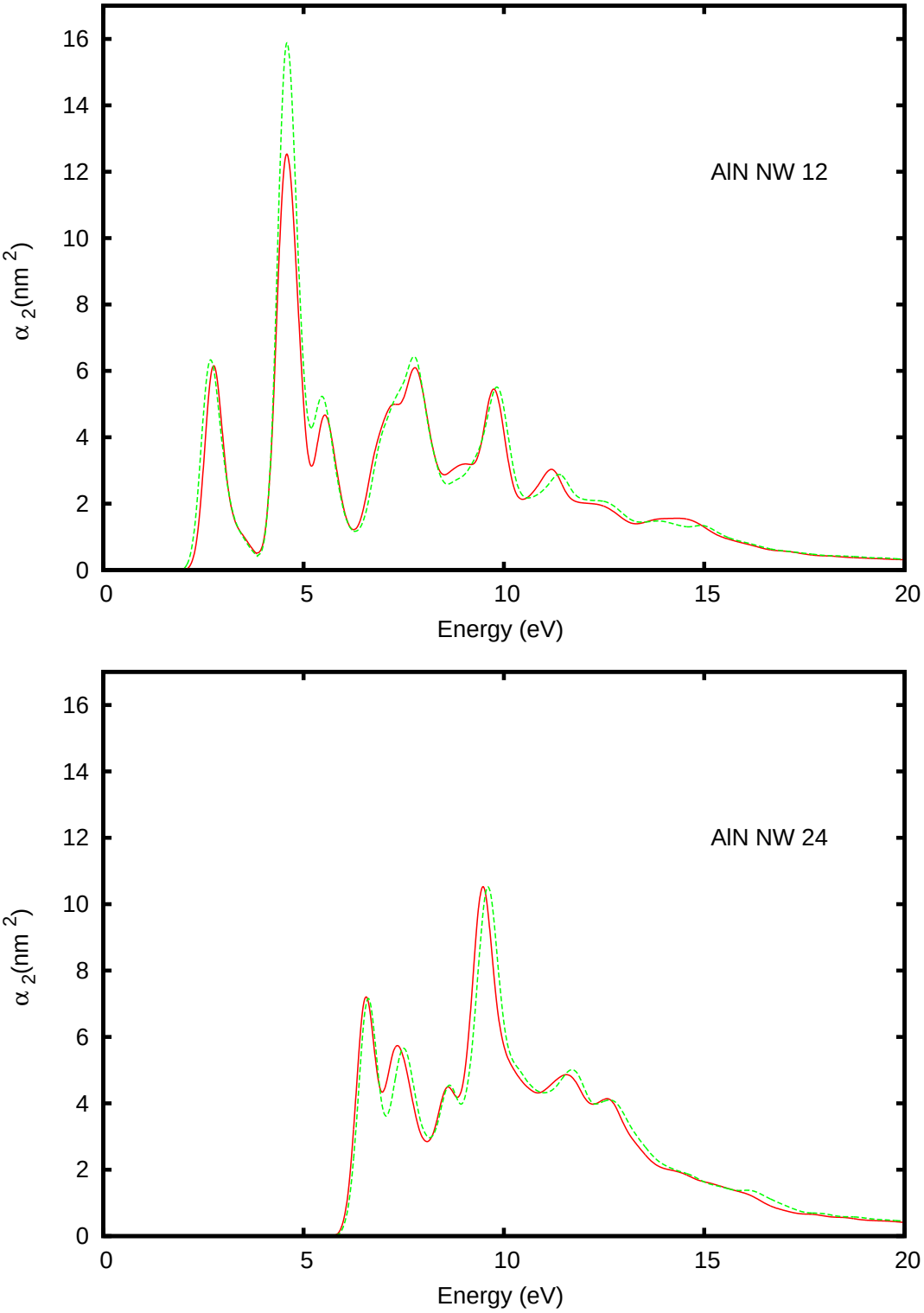

Figure 4.10: Imaginary part of the polarizability function for the smallest AlN nanowire of Type I. The top graph is for the unpassivated nanowire while the bottom graph is for the passivated nanowire. The solid curve is for the unstrained structure while the dashed one is for the structure under 2 % strain.

Since some of our nanowires are passivated and others are unpassivated, we explored both the surface effect and the dimension effect of ZnO and AlN nanowires. First, we computed the imaginary part of the dielectric function for the relaxed structure of Type I nanowires. Afterwards, we compressed them by 2 % along the wire direction, relaxed the structure and computed again the imaginary part of the dielectric function. The results are summarized in Figures 4.9-11. On these graphs, the first one is for the bulk while the other two are the passivated and the unpassivated nanowires. In order to get a meaningful quantity for nanowires, we computed the imaginary part of the polarizability . This was obtained first by computing the dielectric constant ϵ and the dielectric susceptibility $\kappa = (\epsilon - 1)/4\pi$. We then multiplied the susceptibility by the cross-sectional area of the supercell perpendicular to the nanowire axis. The quantity obtained is the polarizability $\alpha(\omega)$ in nm^2.

Some observations can be deduced from these results. First, the optical structure of the passivated nanowires is closer to the bulk structure than that of the unpassivated structure. This confirms our analysis that ionic nanowiress should be passivated in order to get meaningful electronic and optical properties. In particular, we see that unpassivated nanowires are characterized by extra absorption peaks. We can now consider the effect of compression on the optical spectrum. A general trend is that, for the most part, passivated nanowires behave as bulk. The shift towards higher frequencies is maintained. On the contrary, unpassivated nanowires show a shift towards lower frequencies. The reversal is more pronounced for ZnO where it covers all the energy region up to 7 eV. For AlN, the reversal is only seen for the first peak.

4.11 Conclusion

Different properties have been computed for ZnO and AlN nanowires using DFT in the LDA approximation. On one hand, when nanowires are passivated, they show

an increased band gap. When they are not passivated, a reconstruction takes place resulting in a decrease in the nanowire diameter. For ZnO, a small increase in the band gap appears. For AlN nanowires, the band gaps decrease and the change in diameter is not as big as in ZnO case. Polarization results show an enhancement of the piezoelectric constant e_{33} when nanowires are not passivated and a decrease when they are passivated with fictitious hydrogen atoms. Depending on the impurity found on the nanowires, the piezoelectric effect can be enhanced or decreased. We observed also a big impact of the piezoelectric field on the unpassivated ZnO nanowires with a hexagonal shape (the smallest one). Since this effect was not seen on other nanowires, we suspect that this is due to the special structure of the nanowire since all the atoms are surface atoms.

CHAPTER V

MELTING TEMPERATURE OF SILICON NANOWIRES

5.1 Introduction

Nanoscale materials are very promising because of their potential applications. They are interesting because their properties dramatically change when the size drops to the nanometer scale. At this scale, quantum confinement and the surface effect dominate and will alter the material properties. As nanowires are built to be used in circuits with the Joule effect, it is important to check whether their melting temperature is still high enough to sustain currents at ordinary temperatures without melting. This is even more important since it was shown that the melting temperature of nanowires is lower than the bulk value. Many simulations have been done in order to compute the melting temperature of metallic and semiconductor nanowires [83, 84, 85, 86, 87, 88]. In some of these calculations of metallic nanowires mentioned above, the size dependence was studied. Nevertheless, such studies have not been done on the most used semiconductor which is silicon. It is important though to mention some studies that have been previously done on silicon in this regard. In particular, the melting temperature of silicon nanowires of one diameter and different crystalline structures recently was studied [89]. It was found that the polycrystalline nanowire is unstable and melts at 1250 K while the tetrahedral nanowire melted at 1500 K. The nanowires considered were of 4.5 nm in diameter and for the tetrahedral structure; the [111] direction was considered. The Stillinger-Weber (SW) potential was used in this study. To the best of our knowledge, there has not been any study on the size dependence of the melting temperature of silicon nanowires. The melting temperature of silicon clusters with various diameters was recently studied. A particular study by

Fang, *et al.* [90], computed the melting temperature of various silicon nanoclusters up to 9041 atoms using the SW potential. By plotting the melting temperature as a function of $N^{-1/3}$,they found a linear relationship for nanoclusters with a number of atoms (N) greater than 357. By doing an extrapolation to infinity, Fang, *et al.*, concluded that the bulk melting temperature is 1821 K well beyond the experimental 1683 K value. For smaller clusters, the melting temperature was almost constant with values around 1400 K. In this work, we compute the melting temperature of silicon nanowire in the [111] and [110] directions and examine the size dependence of the melting temperature. We also analyze the local structure of such nanowires around their melting temperature.

5.2 Interaction potential

The calculation uses the Stillinger-Weber potential [91]. This potential is given by

$$V = \sum_{i<j} V_2(i,j) + \sum_{i<j<k} V_3(i,j,k), \tag{5.1}$$

where the two-body potential V_2 is given by

$$V_2(r) = A(Br^{-p} - 1)\, e^{(r-a)^{-1}}, \tag{5.2}$$

and the three-body term V_3 given by

$$V_3(i,j,k) = h(r_{i,j}, r_{i,k}, \theta_{jik}) + h(r_{j,i}, r_{j,k}, \theta_{ijk}) + h(r_{k,i}, r_{k,j}, \theta_{ikj}), \tag{5.3}$$

with

$$h(r_{i,j}, r_{i,k}, \theta_{jik}) = \lambda\, e^{\gamma(r_{ij}-a)^{-1}+\gamma(r_{ik}-a)^{-1}} (cos(\theta_{jik}) + 1/3)^2. \tag{5.4}$$

In the above equations, r is the distance between any pair of atoms, a is the cut-off distance for the two-body term (and the three-body term) and θ is the bond angle between triplets of atoms. The other parameters are set as $A = 7.049556277$, $B = 0.6022245584$, $p = 4$, $a = 1.8$, $\lambda = 21$, and $\gamma = 1.20$. The lengths and energies

in the formula are in reduced units. We get the true value by multiplying any length by 0.20951 nm and energy $3.4723 \times 10^{-19} J$. In other words, the two-body-potential will be computed only if the separation between the two particles is smaller than 1.8 reduced units (3.77 Å) and the three- body potential is computed if the distance between any of the two atoms in the triplet is within the cut-off distance.

Figure 5.1 shows the shape of the two-body and the three-body terms for the Stillinger Weber potential as a function of the interatomic distance. For the three-body term, we assumed an angle of 132^o and the values of r_{ij} and r_{ik} to be equal. This distance assumption is true for the crystalline phase since tetrahedrally coordinated atoms are at equal distance one from another.

It can be seen that the two-body term reaches its minimum at r = 1.12 (reduced units) which is about 2.35 Å, the known nearest-neighbor distance for the silicon bulk. We can also say that the major contribution in the potential energy comes from nearest neighbors. Any increase or decrease of this value would greatly affect the total atomic potential energy. Since all the parameters in the three-body term are positive, its contribution is always positive. Moreover, its magnitude is always smaller than the two-body term in areas of interest but significantly can change energy especially when the number of nearest neighbors increases. This term is zero for $\theta = 109.5^\circ$ and is maximum for $\theta = 131.8^\circ$.

We know that many potentials have been used to simulate bulk silicon. The most popular ones are the Stillinger-Weber and the Tersoff potentials. The question we want to answer is whether the SW potential should be used to simulate nanowires since they were parameterized for bulk. The question arises because nanowires are dominated by surfaces and potentials used have to be tested to see if they give basic surface properties known experimentally. A paper by Xie [104] and others used the SW and the TS potentials on the (001) surface of silicon. Their simulations, done at 300 K and 1000 K shows that SW result confirms a (2×1) reconstruction of the

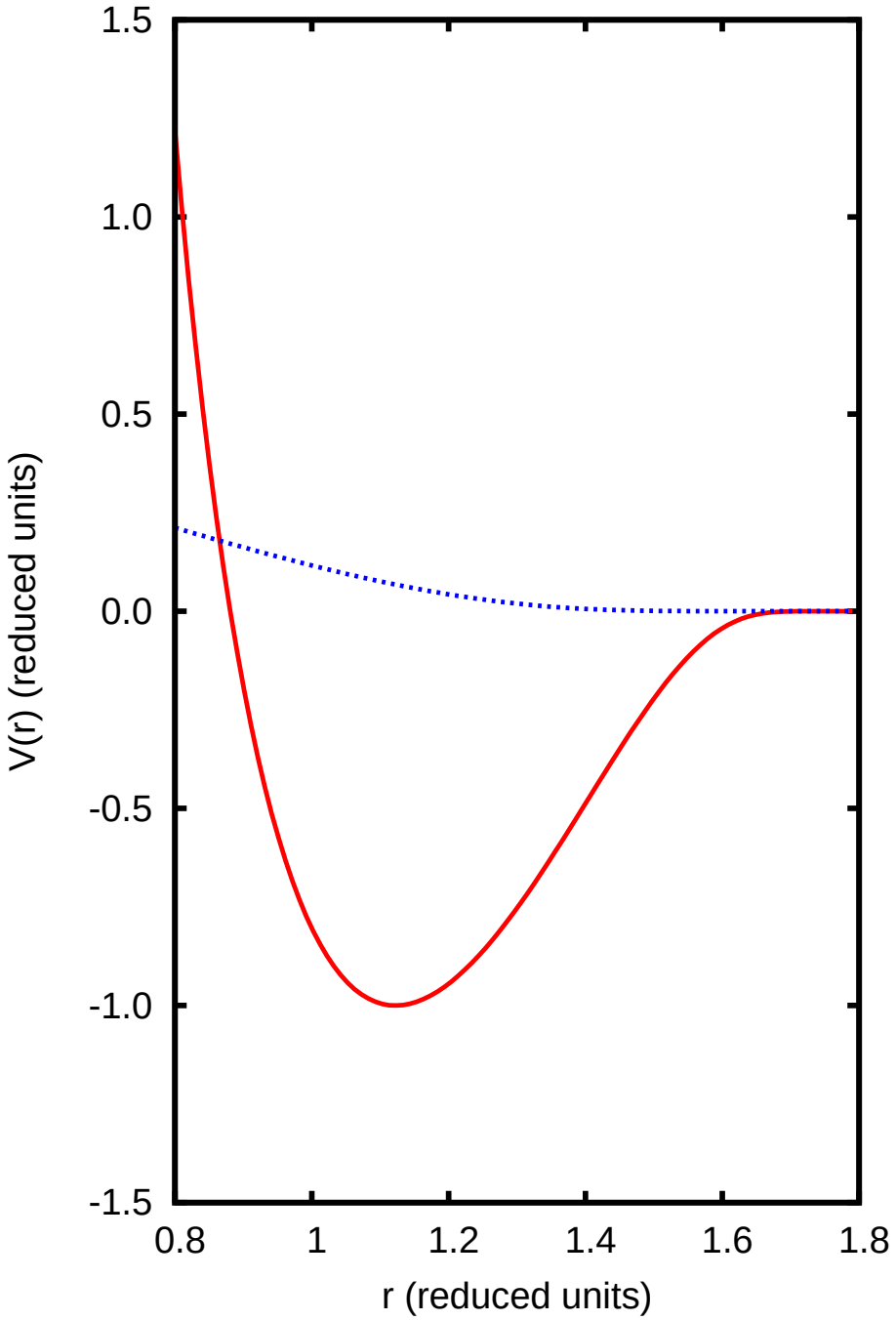

Figure 5.1: The two-body potential (filled curve) as a function of the distance between two silicon atoms and the three-body potential (dotted curve) for equally spaced triplets. Distances and energies are in reduced units as discussed in the text.

surface as observed in experiment. Moreover, a paper by Abraham, *et al.*, computed the triple point characteristics of (100) and (111) surfaces using the SW potential [98]. The melting point obtained was close to the bulk melting temperature. From this point of view, SW is the best choice for silicon nanowire calculation. We would mention though that at zero temperature the TS potential was found to give better reconstructions for the silicon nanowire than SW [102]. We know nevertheless, that the TS potential gives poor melting temperature even for bulk silicon . For all of these reasons, we chose the SW potential.

5.3 Calculational methods

Computations were done using a popular free software called XMD, developed by Jon Rifkin at the University of Connecticut. The Stillinger-Weber potential was used. The Gear algorithm used to integrate Newton's equations of motion employs up to the 5^{th} derivative of the particle motion. The program's output energies (potential and kinetic) and particle coordinates. From the output, we computed other local structural properties by writing different fortran codes. These codes allowed for computing the two- or three-body components of the potential energy, the pair correlation, the diffusion coefficients and much more.

Computing the melting temperature can be very challenging. Many methods have been developed through the years and most of them rely on the discontinuity that happens when a semiconductor or metal undergoes a phase transition. In a study on the melting of amorphous silicon by W. D. Luedtke and U. Landman [94], many parameters abruptly changed during the solid to liquid phase transition. This includes the potential energy $E_p(T)$, the system density ρ, the coordination number and root mean squared displacement given by

$$R^2(t) = \frac{1}{N}\sum_{i=1}^{N}[r_i(t) - r_i(0)]^2. \tag{5.5}$$

This is the method employed in this calculation. The potential energy as a function

of temperature is plotted. The graphs obtained for all nanowires were similar and one example is shown in Figure 5.2, where the melting temperature can be determined easily.

A more rigorous calculation can be used to get the melting temperature. It is obtained as the temperature at which the chemical potential of the liquid phase is equal to the chemical potential of the solid phase. This method was successful in getting the melting temperature of bulk silicon with a 1% error [97]. The Stillinger Weber potential was used in the calculation. The same concept was used with less success in Car-Parinello molecular dynamics simulation with the density functional theory in the local density approximation [96]. The large error in the calculation was blamed on the accuracy required in such calculation. Indeed it is known that the chemical potential varies very slowly with temperature. Therefore in order to acheive good melting temperature, extremely high accuracy is required. For this reason, such method was not attempted.

Another method often used in order to locate the melting temperature of a solid is the Lindermann criterion. This rule states that the solid will melt when the root-mean-squared displacement is approximatively 13% of the bond length. This criterion was introduced in 1910 and measures the atomic vibrational amplitude $< \Delta r^2 >^{1/2}$. For irregular finite systems such as clusters, an alternative criterion called the distance-fluctuation criterion [92] is often used. It is based on the Berry parameter Δ_B given by

$$\Delta_B = \frac{2}{N(N-1)} \sum_{i<j} \frac{\sqrt{< \Delta r_{ij}^2 >}}{r_{ij}}. \tag{5.6}$$

Another similar parameter is called the Etters-Kaelberer parameter Δ_{EK} and is given by

$$\Delta_{EK} = \frac{1}{NP} \sum_{i=1}^{NP} \frac{\sqrt{< \Delta r_{ij}^2 >}}{r_{ij}}, \tag{5.7}$$

where N is the number of particles and NP is the number of neighbor pairs where

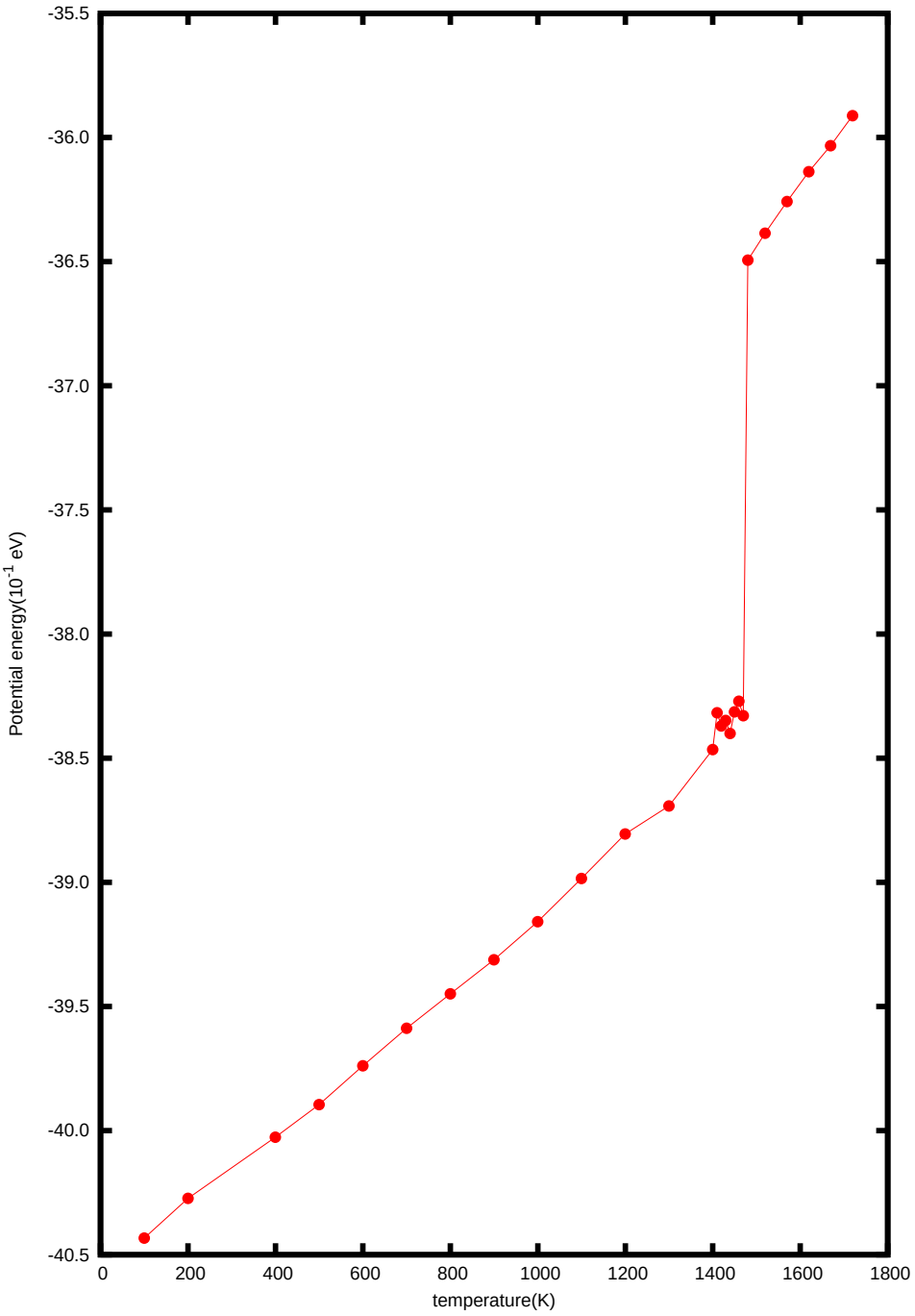

Figure 5.2: Average potential energy per atom for the nanowire in the [110] direction with 2.5 nm diameter.

members of each pair are separated by a cutoff distance r_{nm}. The value of this parameter has been suggested to be 0.1. By experience, the critical values obtained from the distance-fluctuation criterion are smaller than those obtained from the root mean squared fluctuation. This method could not be used in our calculation because first the Lindermann criterion was introduced to help get bulk melting temperature in case of superheating. Moreover, the calculation of the mean squared displacement or similar assumes that these quantities are constant for a given temperature. Such an assumption does not work for nanowire since surface atoms start to diffuse (the root mean squared displacement varies with time) long before the melting. That is why such parameters are not considered in this study.

The nanowires were prepared by carving out a cylinder of a desired diameter out of bulk silicon along the (110) or (111) direction. The cylinder center was chosen to coincide with a particle position and the diameter was chosen so as to minimize the number of dangling bonds. The periodic boundary condition is used only in the z direction with a cell dimension up to 2.3 nm. We used a supercell that consists of six times of the primitive cell in the z direction. This was done in order to minimize the energy error bar in the kinetic energy term. The structure was then optimized following the "simulated annealing" suggested by Gülseren, *et al.* [100], for thin nanowires. The structure was prepared in the following sequences: thermal annealing cycles were simulated with the temperature rising in steps of 100 K up to 1200K and decreasing back to T = 0 at the same rate. During the annealing, a time step of 1 fs was used for 80 ps at each temperature. Once back at zero Kelvin, the nanowire length finally was allowed to adjust. The energy of the the final structure was found to be lower than that of the initial structure by about 0.1 eV/atom. The annealing process was repeated but the energy at 0 K did not improve. As it can be seen in Figure 5.3, facets look more pronounced than the unoptimized structure.

Once the nanowire was optimized, the temperature was increased at steps of 100K

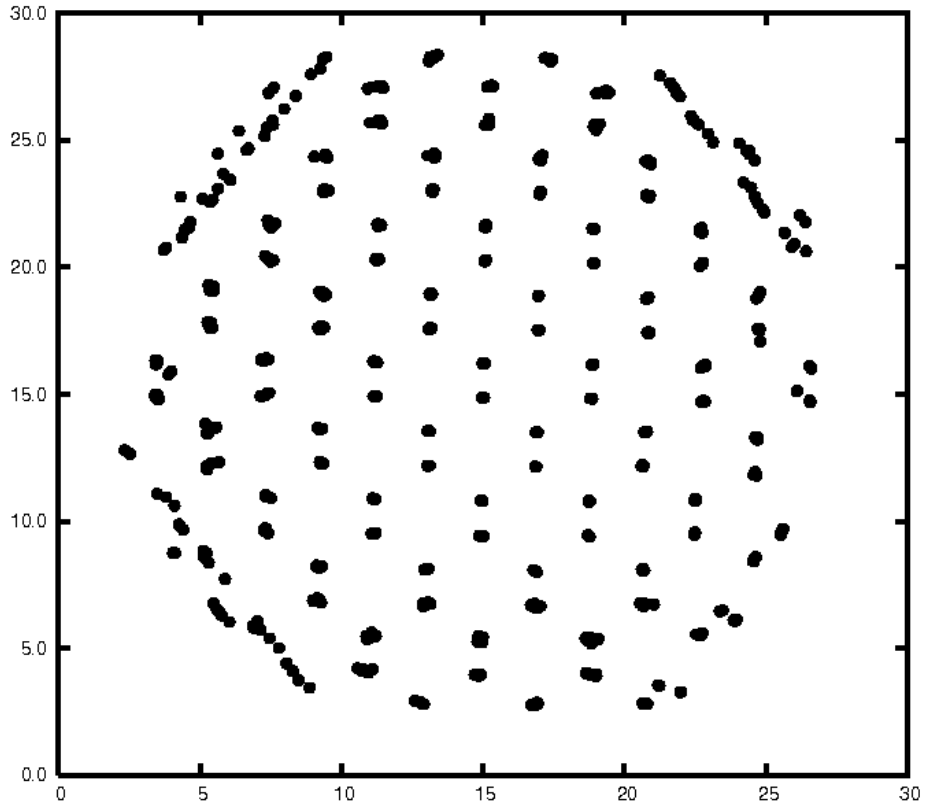

Figure 5.3: Top view of the lowest energy structure of the 2.5 nm nanowire in the [110] direction after annealing cycles.

with a 0.5 fs time step for 200 ps at each temperature. Near the melting temperature, the temperature was reduced by steps of 10 K, while keeping the same 200 ps running time. At each temperature, the structure configuration was stored for a possible continuation run if we estimate that the run time was not enough. The potential energy was then plotted as a function of temperature in order to see the point where the phase transition occurs. Once the point was located, we walked backwards and did a continuation run for the temperatures near that transition point. For each temperature, a run time of to 2 ns was used and if the energy stayed the same, calculations was stopped and and the new value was recorded as the melting temperature. For example, when looking the melting temperature of the model wire with 2.5 nm diameter in the (110) direction (Figure 5.2), we found a melting temperature of 1520K. After revisiting the calculation with longer run time, it was found that at 1510K, 1500K, 1490 K, and 1480 K, the nanowire was already in the liquid phase. Other properties such as the self-diffusion, the angular distribution, and others were calculated in order to confirm the structure change.

5.4 Pair correlation function of nanowires

The pair correlation function (PCF) is one of the parameters that help explain why the potential energy jumps at the melting temperature. This parameter allows us to confirm also whether the jump is really due to melting or to something else. The PCF is defined as

$$g(r) = \Omega < n_i(r, r + \Delta r) > /(4\pi r^2 \Delta r N), \tag{5.8}$$

where $< n_i(r, r + \Delta r) >$ is the average number of atoms surrounding the i^{th} atom between r and $r+\Delta r$. N is the total number of atoms involved, and Ω is the volume of the supercell. If the center of one particle is fixed at the origin, then the probability of finding a second particle in a region **dr** is given by $\rho g(r)\mathbf{dr}$. Therefore, g(r) contains the information about the system's density fluctuation. A value of 1 means a uniform

density while a value of zero means that there is no possibility of finding any particle within this radius. There are bounds for g(r). When $r \to 0$, $g(r) \to 0$ because particles can not penetrate each other. When $r \to \infty$ then $g(r) \to 1$ because the system looks uniform as we recede further and further from the origin. Between these boundaries, we have peaks that normally are centered at nearest neigbors distances [93]. This is specially true for a crystalline structure because particles are confined except for small oscillations around an equilibrium position. As temperature increases towards melting, particles become less localized and peaks further from zero start to merge. The first peak does not normally disappear even for gas. Since the volume of a nanowire is not very well defined, parameters that did not change in the Equation 8, such as the volume and other constants were ignored. The PCF of the 2.5 nm diameter nanowire is shown on Figure 5.4.

From this graph, we realize that the pair correlation function of the nanowire at T = 1480 K differs from that of T = 1470 K. At T = 1470 K, many peaks up to 10 Åcan be seen. Looking at the peaks at this temperature, one sees that peaks are at the first, second, third, forth .. neighbors that are 2.25 Å, 3.89 Å, 4.5 Åand 5.91 Å. At T = 1480 K, the peaks flatten after the two initial peaks. This is a sign that the nanowire has reached a liquid state as it's pair correlation looks bulklike. [93, 94]. The reason it is not completely horizontal is because of surface atoms, which have less coordination. Moreover, we realize that the first peak (which is the lowest energy peak for the Stillinger Weber potential) shifts a little bit. This shift has also been observed before and can change the total potential energy [95]. From this graph we deduce the average bond length that is defined as the distance up to the first minimum of the pair correlation. In our case, the value was set to be $3.0\mathring{A}$ near melting, which is higher than the bulk value (around 2.55 Å). The coordination number was then derived; and as we know, it is 4 for atoms inside the nanowire and 2 or 3 for the surface atoms. In the sample nanowire, the average coordination number at zero temperature was

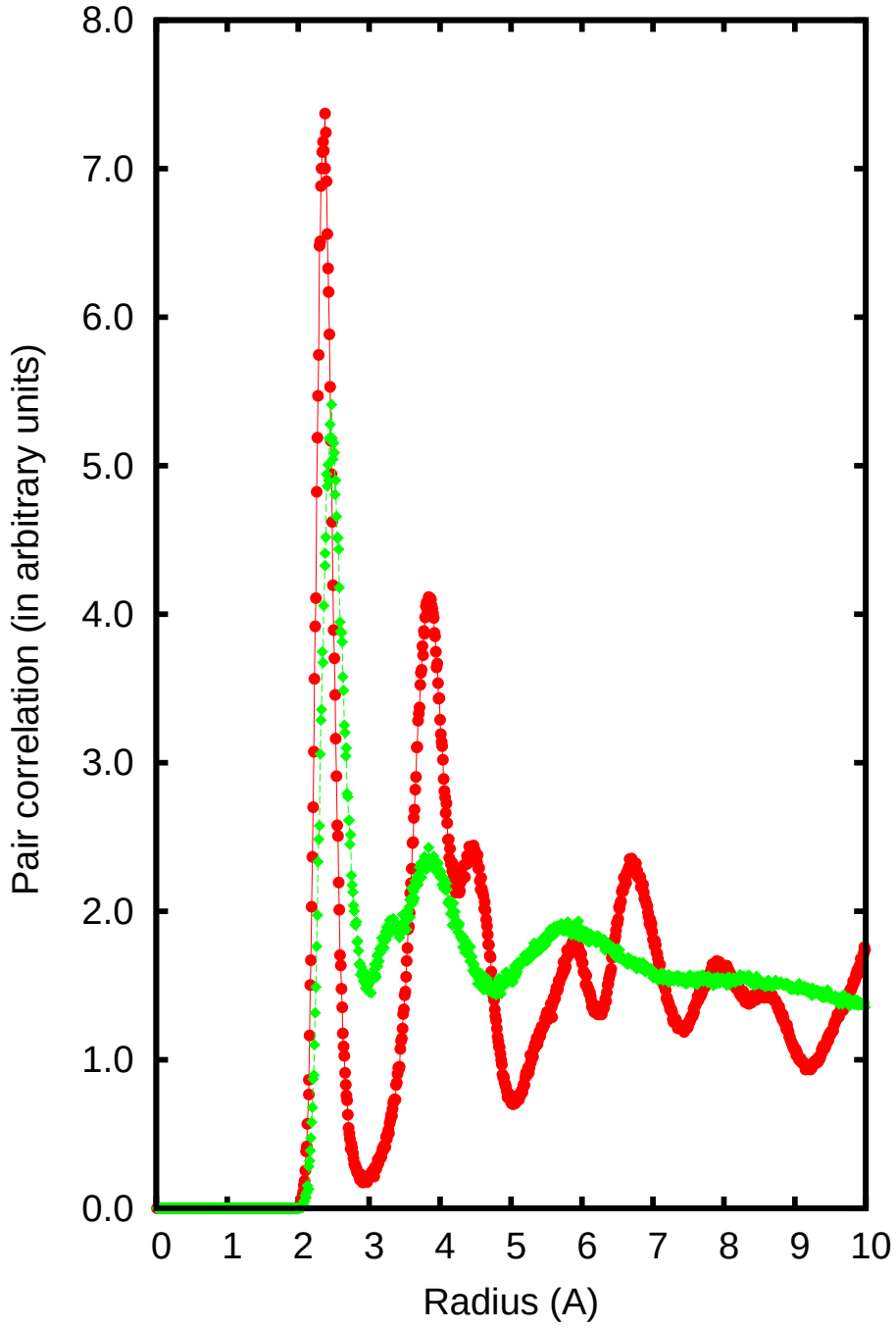

Figure 5.4: The pair correlation function for the 2.5 nm diameter nanowire. The diamonds stand for results at T = 1480 K, and the circles are for T = 1470 K.

3.84. The value increased very slowly until it was 3.94 before melting. At the melting temperature, the value jumped to 4.77 because of the large number of atoms with 5 nearest neighbors in the liquid phase. The average coordination number continues to increase slowly and is around 4.86 for T = 1700K. This increase in the coordination number has been shown for bulk silicon [94] by Luedtke and Landman. In their paper, they showed that in the liquid phase, 29% of particles are threefold coordinated, 48 % are five fold coordinated, and 19% are six fold coordinated and an average of 4.89. It is therefore clear the majority of atoms are five fold coordinated, and the nanowire in the liquid phase is very close to silicon liquid.

5.5 Potential energy components

We defined the melting temperature as the temperature at which the potential energy increases abruptly. Looking at the potential used, this increase can come from the two-body potential or the three-body term. The latter term is dominated by the angular dependence. If the angle between a triplet is 109.5°, the three-body term becomes zero. A deviation from this special angle increases the three-body term. In Figure 5 (top panel), the angle distribution of triplets for the 2.5 nm diameter nanowire is plotted. We looked only at triplets separated by a distance less than or equal to 3 Å , which is the first lowest minimum. At T = 1470 K, the angular distribution is largely concentrated around the 109.5°. When the nanowire melts, angular distributions spread out more. Moreover, the 1480 K angular distribution has a peak shifted to a lower angle compared to the 1470 K result where the center of symmetry is at 109.5°. Therefore, it is easy to understand why the potential energy increases. It is a combination of the change in the nearest neighbor's distance and a spread in the angular distribution that create an increase in the three body term. In Figure 5 (bottom panel), the two-body term and the three-body term are decoupled before and after melting. It can be seen that the two-body term decreases during

melting, while the three-body term increases even more. The decrease in the two-body term is due to the increase in the coordination number. We showed indeed that the liquid phase is dominated by a coordination number of five, while particle pairs within the nearest neighbor's distance interact with the lowest potential energy. The increase in the three-body term is due to the deviation from the tetrahedral structure. Luedtke and Landman reached the same conclusion for bulk silicon [94].

Finally, we computed the latent heat of fusion that we defined as the difference between the liquid potential energy and the solid potential energy. Normally, the latent heat of fusion is this difference if the simulation is done at constant pressure. Here, the simulation is done at constant temperature and pressure term should have been added in the latent heat of fusion value. Since the concept of pressure is not defined in one dimension, the correction was assumed to be zero. For nanowires in the [110] direction, the value was found to range between 1.29×10^4 J/mole and 2.47×10^4 J/mole for nanowires ranging from 1.6 nm to 5 nm of diameter. The trend seems to go in the right direction since the bulk latent heat using Stillinger-Weber is 3.0×10^4 J/moles.

5.6 Self-diffusion

We computed the self-diffusion coefficient for temperatures near the melting temperature. The self-diffusion is defined as

$$2Dt = \frac{1}{N} \sum_{i=1}^{N} [z_i(t) - z_i(0)]^2, \tag{5.9}$$

where D is the self-diffusion coefficient, t is the run time and z_i are the coordinates of atoms in the nanowire direction. The factor of two on the left hand side of the equation comes from the fact that we do calculations only for the z direction. In our computation, a run time of 100 ps was used in which a graph of the mean squared displacement was plotted as a function of time. A least squared fit was then applied to the graph and the slope of that least squared line was divided by two in order to get

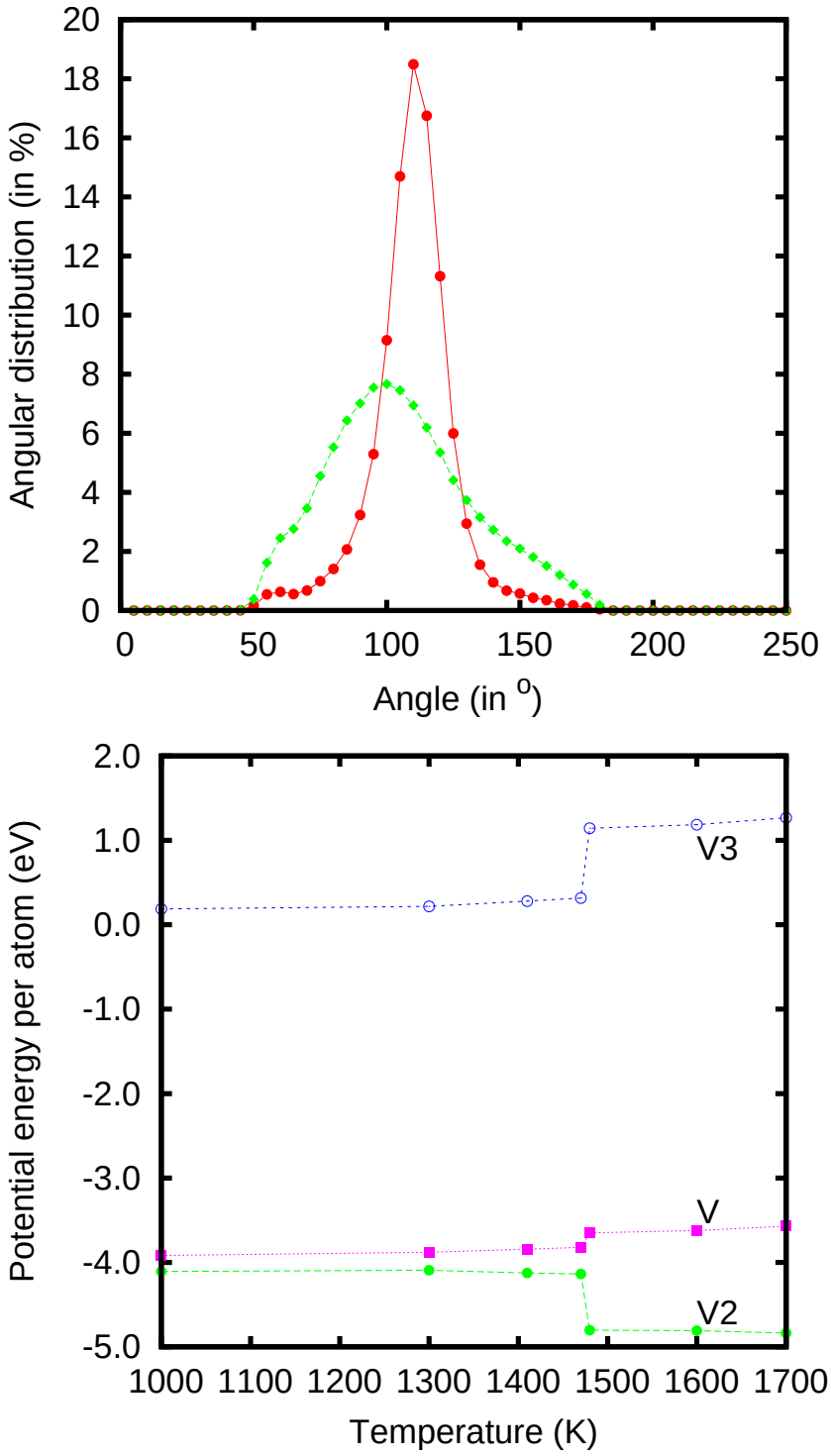

Figure 5.5: The top panel is the angular distribution between triplets (in %) as a function of temperature . The curve with circles is for T = 1470K, while the one with diamonds is for T = 1480K (in liquid phase). The bottom panel is the contribution of the two-body term (V2) in the potential, the three-body part (V3) and the total potential energy as a function of temperature for our 2.5 nm model nanowire.

the self-diffusion. This process was repeated 100 times and an average of the diffusion coefficient was obtained. It was checked to see whether this values oscillated around the same value before taking averages. Moreover, computation was done when it was established that the equilibrium has been reached for the particular temperature. For temperatures below the melting temperature, the mean square displacement is not increasing as the time increases. That is why we did not plot anything below 1200K. Results show that just below the melting temperature, the self-diffusion increases abruptly.

Apart from the clear jump at the phase transition, we realize that the self-diffusion coefficient obtained is close to the known results for bulk silicon. From previous calculations on the silicon self-diffusion using the Stillinger Weber potential [97], the reported values at bulk melting were $6.4-6.9\times10^{-9}m^2/s$ and ours was $6.7\times10^{-9}m^2/s$. Calculations made with silicon spherical clusters give a self-diffusion coefficient to be around $1.0 \times 10^{-9}m^2/s$ which is 6.7 times lower than our coefficients. This result is easy to understand since clusters are zero dimension. Atoms move a very short distance before meeting the boundary.

Just before completing melting, the diffusion of surface atoms in the z direction was also computed. We realize that their mean squared displacement can be linear before the average mean squared displacement becomes linear. As an example, for T=1470 K, one could get a diffusion of $2.5 \times 10^{-10}m^2/s$ for atoms lying at 1.5 Å within the nanowire surface. Therefore, we could conclude that melting starts from the surface and proceeds to inside. Another thing that was tried is to verify whether during melting, the liquid phase still contains clusters of atoms. For that purpose, we recorded the nearest neighbor list for each atom as the simulation proceeds. As a conclusion, the list keeps on changing after some few ps. We conclude that at T = 1480 K, there is complete melting. Atoms diffuse in the z direction while they move in and out of the center of the nanowire.

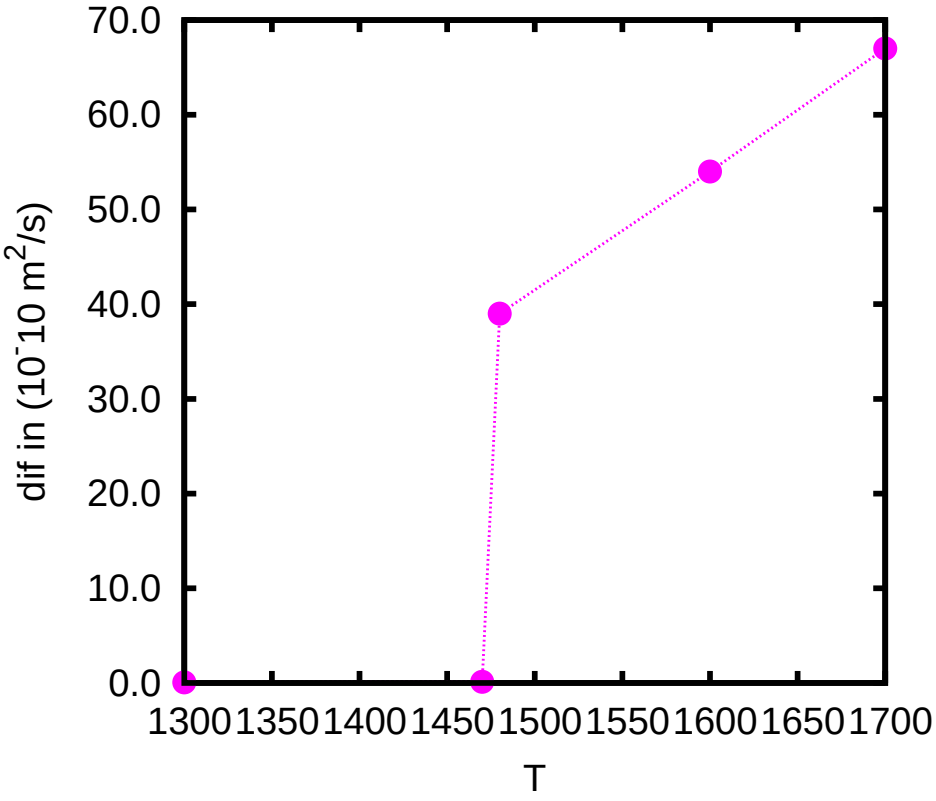

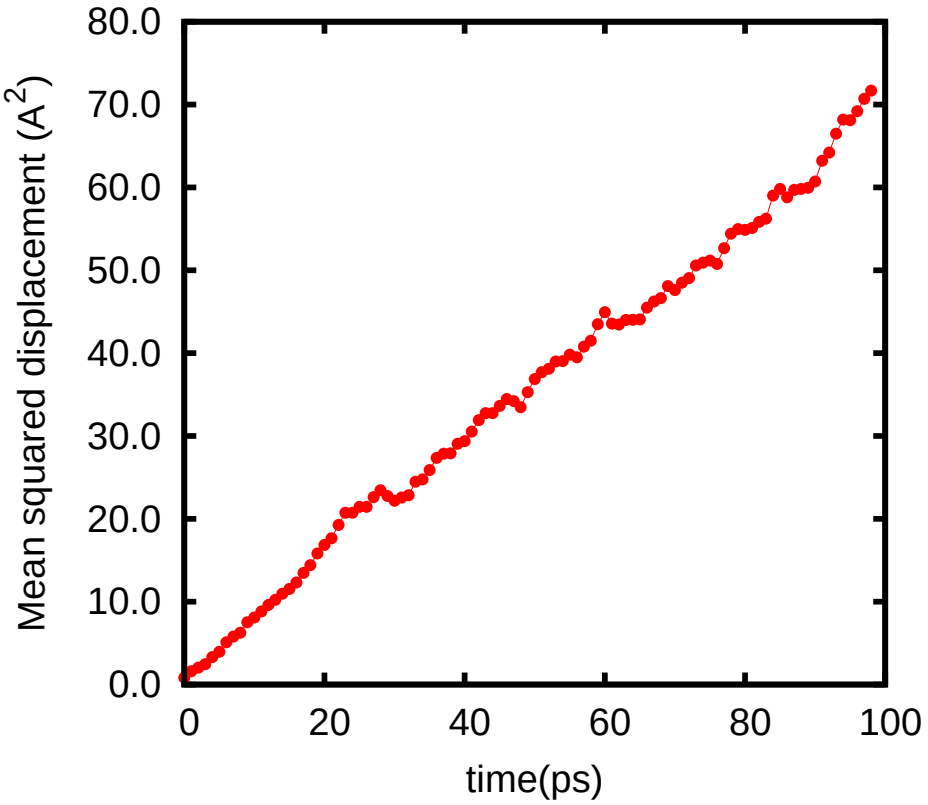

Figure 5.6: The top panel is the self diffusion coefficient as a function of temperature for the 2.5 nm diameter, while the bottom panel is a typical mean squared displacement along the Z direction in the liquid phase.

5.7 Density

When computing the melting of nanowires, so many things happen. In some instances, these nanowires break into two pieces before melting. In order to verify that the increase in potential energy is not due to breaking, we decided to plot the number of particles per unit length in the nanowire direction. This process was done for 1000 configurations and an average was done when the nanowire energy patterm showed convergence. Figure 5.7 shows the results obtained for the 2.5 nm diameter nanowire in the [110] direction. The density in the z direction was computed as the number of atoms per unit length, while the one in the radial direction was the number of particle per unit area. Finally the values obtained were divided by the total average density in each direction. In both directions, we divided the axis in 100 equal parts so as to obtain smooth curves. Moreover, we used an average of 500 configurations obtained after the system had reached an equilibrium state. At T = 1470 K, the Figure 5. 7 (top panel) shows 12 major peaks that are the 12 layers of atoms initially in the supercell. In Figure 7 (bottom panel), five peaks can be identified by using the top view of Figure 3. After melting, one can observe a smooth horizontal curve showing an uniform distribution in both directions. Nevertheless, in the radial direction, there is still a small peak at the nanowire boundary. This is due to the motion of atoms at the surface jumping in and out of the surface. We can conclude then that nanowires melt without breaking.

5.8 Trajectories

One way of looking at what happens during melting is to observe the atom's motions. In Figure 5.8, we show the trajectory of atoms on just one layer among the 12 layers being simulated for the same nanowire described earlier. For the nanowire at 1470K, we show trajectories during 250 ps to be sure that results are not due to the shortness of time. As it can be seen on the top panel of Figure 5.8, surface atoms only are

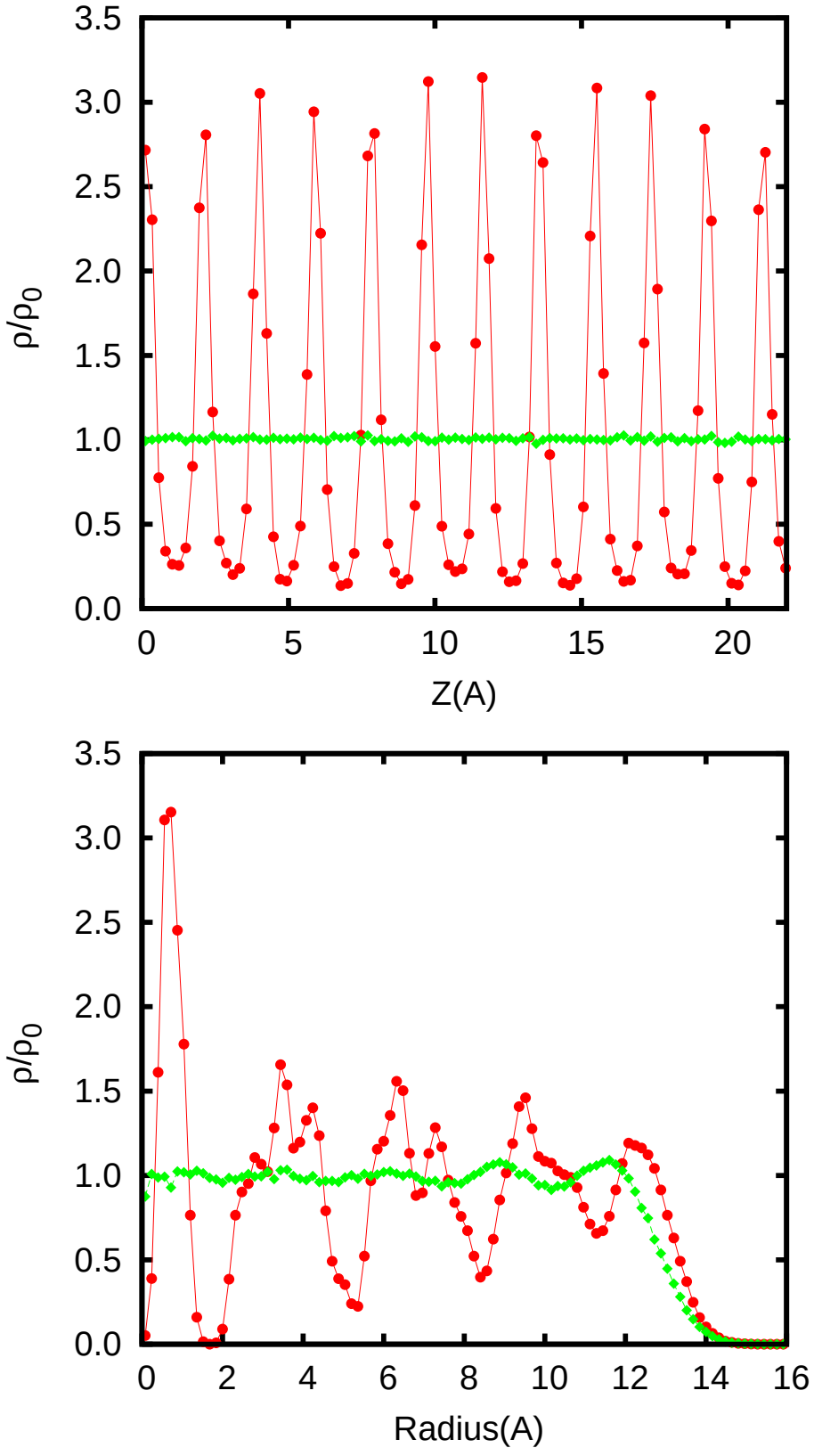

Figure 5.7: The nanowire density of atoms along the nanowire direction (top panel) and in the radial direction (bottom panel).The density for each direction is divided by the total average density. The curve with circles is for T = 1470 K while the one with diamonds is for T = 1480 K.

moving away from their equilibrium configuration. For the melting temperature curve (bottom panel of Figure 5.8), only 50 ps were enough to see how all the atoms move away from their initial positions.

In order to see what exactly happens around the time the melting occurs, we made some trajectorie's curves of the first layer 60 ps before the structure collapses into liquid form. This was done at T = 1480 K, which is the nanowire melting temperature. As can be seen from Figure 5.9, round 800ps are required in order to observe melting. This is normally far larger than the time of run used in most nanowire simulations reported in the literature. A question arises - what is what prompts us to increase the run time? As Figure 5.9 shows, the potential energy curve is not converging; so we have to wait until the system does finally settle around a certain value.

We report then what happens around this time (800 ps) using trajectories. It is obvious that it takes around 60 ps to reach equilibrium. Figure 5.10 (top panel) shows the top view of atoms of the first layer between 740 ps to 800 ps just before the potential energy starts to skyrocket. From the figure, we realize that only atoms on the surface moves away from their equilibrium configuration as at T = 1470 K. Moreover, the motion is not symmetric all around the surface. Maybe, melting initiates at a weak point and propagates from that point. From T = 800 ps to 860 ps, the interval of time when the potential energy increases fast, we observe a collective motion of atoms moving all around the nanowire section as seen in Figure 5.10 (bottom panel).

A similar set of graphs is showing the XZ plane's projection of atoms trajectories having a Y initial position between -2 Åand 2 Å. In Figure 5.11 (top panel), we see that between 740 ps and 800 ps, atoms on the surface are the only ones involved in long range motions. The motion is especially visible in the z direction where we realize that at the surface there are no more layers of atoms. Atoms are already diffusing in the z direction while inside, a crystalline structure is still visible. Between 800 ps and 860 ps, we observe "random motion" both in the Z direction and in the radial

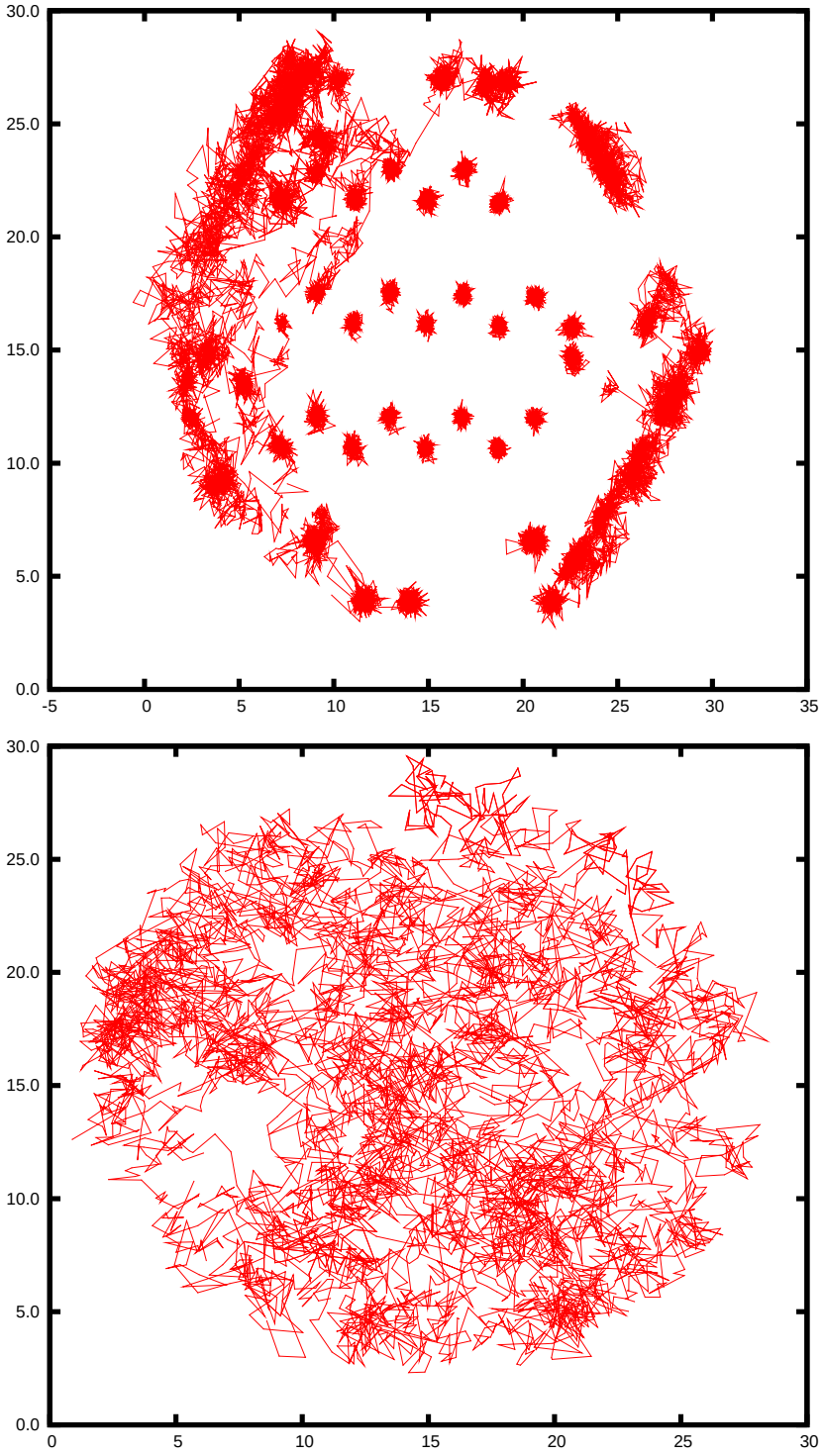

Figure 5.8: Top view of particle trajectories of one layer of nanowire at T = 1470 K, (top panel) and at T = 1480 K (lower panel). The top panel is done using a 250 ps time step while the lower panel is found using only 50 ps. This is done since we can already see that the structure is liquid.

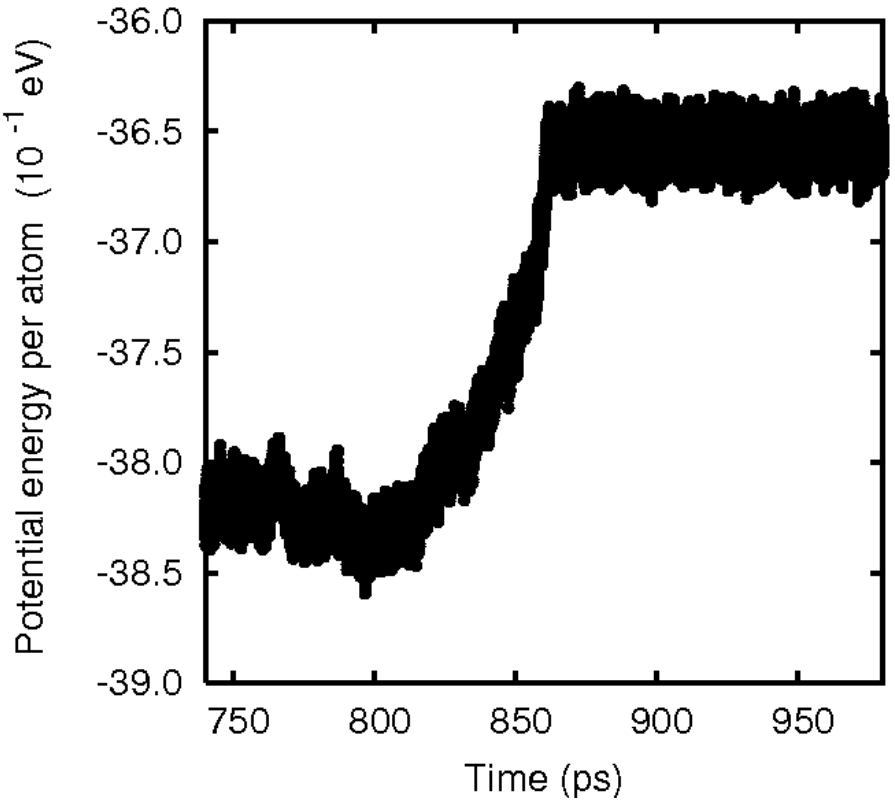

Figure 5.9: Potential energy curve for the 2.5 nm diameter nanowire in the [110] direction at T = 1480 K (the melting temperature).

direction.

5.9 Size and direction dependence of the melting temperature

The first objective of this chapter is to explore the size dependence of the melting point of silicon nanowires with various diameters and different orientations. Two models have been suggested in the past for nanowires and clusters. The first theory was used by Fang, *et al.*, who studied the melting point of silicon clusters using the SW potential. They conclude that the melting point scales linearly with $N^{-1/3}$ or with the diameter. A similar conclusion was reached by Hui, *et al.*, who studied the melting point of nickel nanowires. A linear relationship between the melting temperature and the inverse of the diameter was suggested [86]. For this purpose, results obtained for

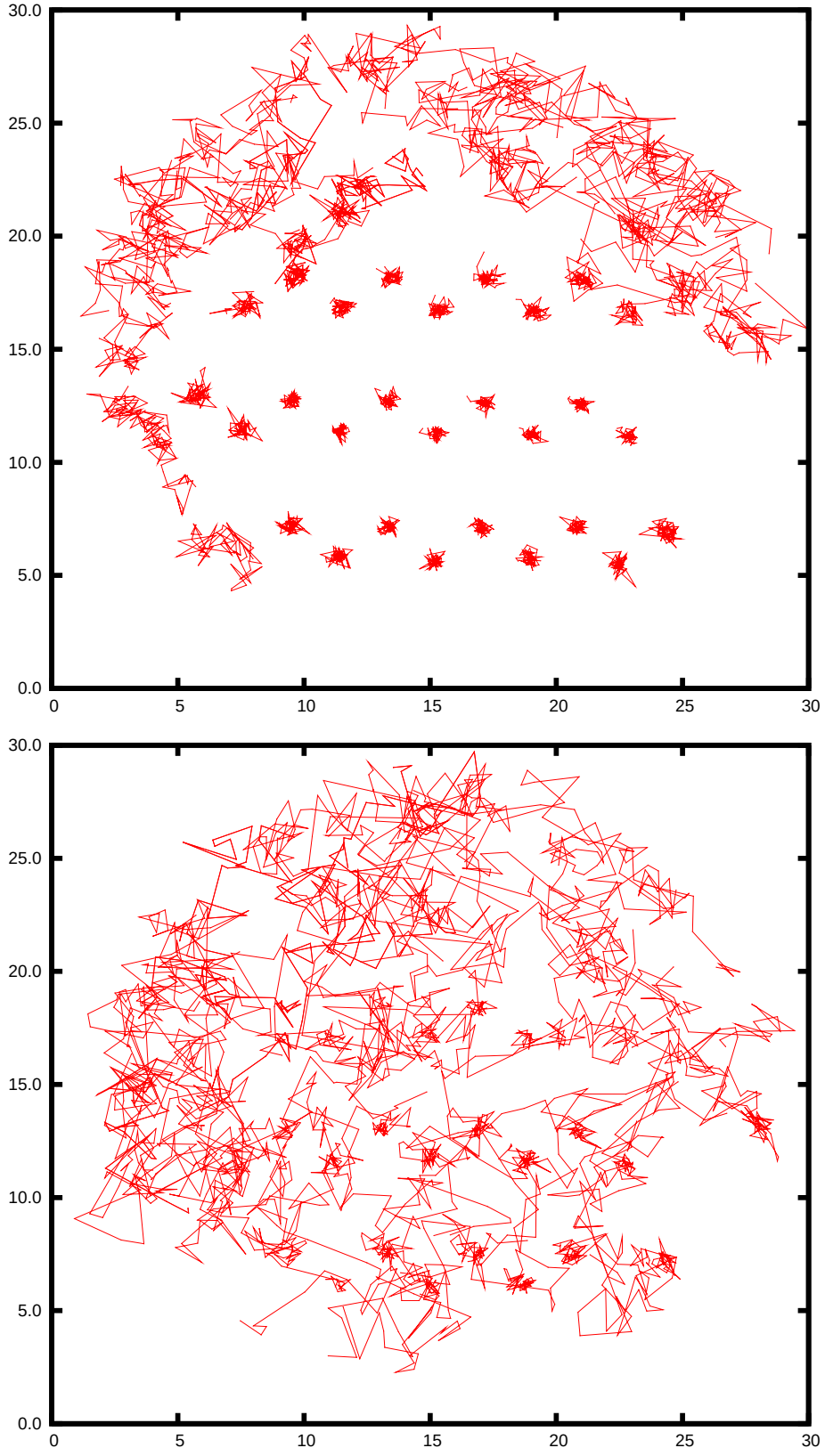

Figure 5.10: Trajectory of one layer of the 2.5 nm nanowire at T = 1480, seen in the XY plane between t = 740 ps and t = 800 ps (top panel) and between 800 ps and 860 ps (lower panel).

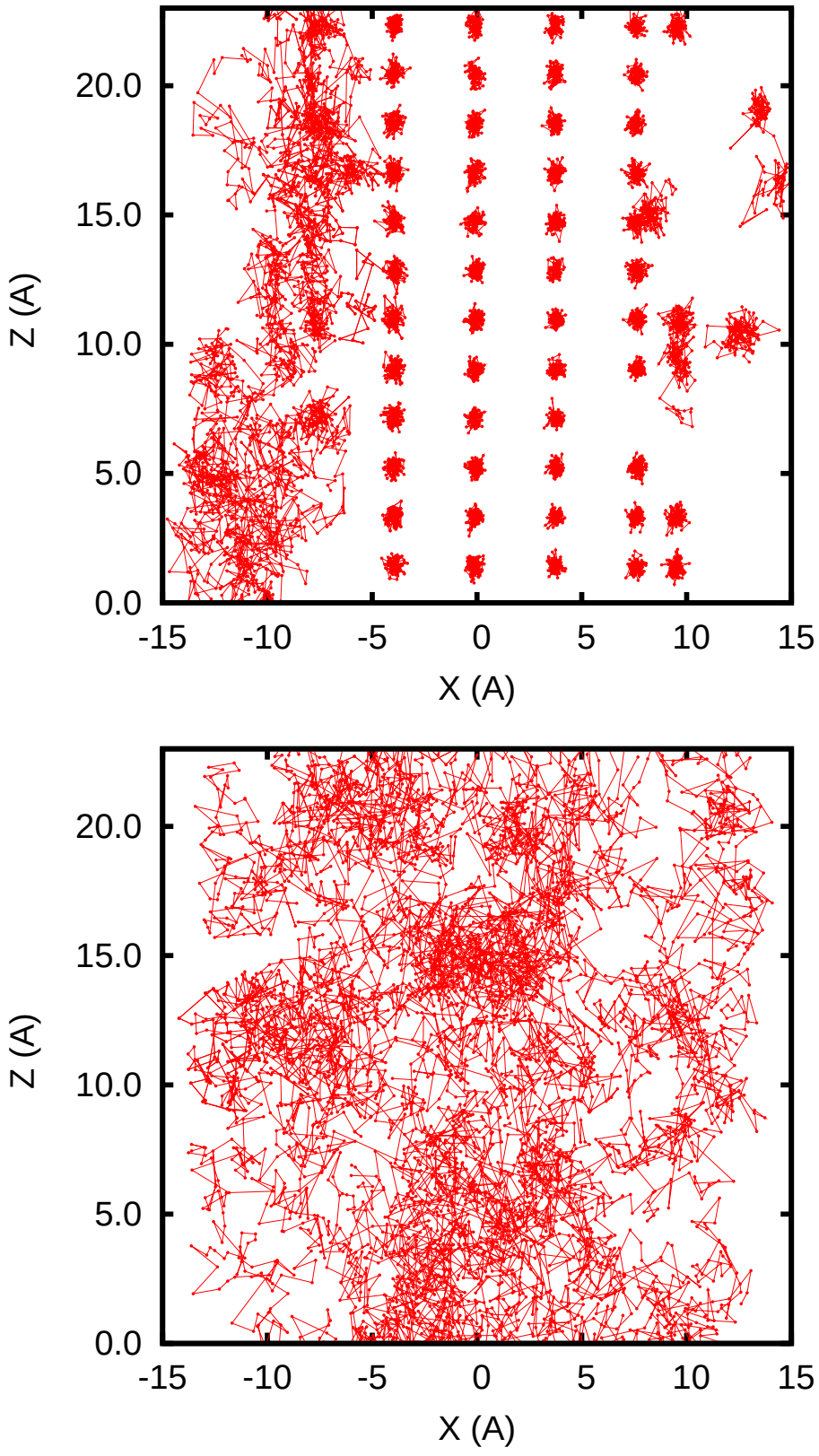

Figure 5.11: Trajectory of one layer of the 2.5 nm nanowire at T = 1480, seen in the XZ plane between t = 740 ps and t = 800 ps (top panel) and between 800 ps and 860 ps (lower panel).

the melting of silicon nanowire were fitted with the function $T_m = T_\infty - \delta/d$ where d is the nanowire diameter in Å and δ is a constant. We found T_∞, δ to be respectively 1791 K and 884.7 K.nm for nanowire in the (111) direction and 1804K and 748 K.nm for nanowire in the (110) direction (Figure 5.12 top panel). The bulk melting temperature extrapolated from these results is higher than the experimental melting temperature that is 1687 K and the 1660 K theoretical value obtained by Luedtke and Landman [94] as well as the 1683 K obtained by Broughton [97]. Looking at the values of δ, one sees that they are similar to those found for metal nanowires which were 857 K.nm for nickel nanowire and 876.7 K.nm for palladium nanowires [86, 87] . In order to see how good this fitting is, one can compute the correlation coefficient r^2 for the linear curve between T_m and $-1/d$. A value of 0.998 was found for nanowires in the (111) direction. For nanowires in the [110] direction, a correlation coefficient of 0.979 was obtained. We see that these values show a good linear relationship. We also tried to fit our functions using a power function $T_m = T_\infty - a * d^{-n}$, where n is the power. The value of n was found to be 1.09 for nanowire in the (111) direction and 1.20 for nanowire in the (110). We see again that the curve in the (111) direction has a the best fit.

Another supposedly more general model was suggested by Zhang *et al.* [106] and is given by $T_m(r) = T_m(\infty)exp[-(\alpha-1)/(r/r_0-1)]$, where $T_m(\infty)$ is the bulk melting temperature, α is the ratio of the mean square displacement (msd) of atoms on the surface and interior of the crystal, r and r_o are respectively the nanowire diameter and the diameter of a nanowire with all the atoms at the surface. In this model, the value of α determines the trend of the melting curve. If ($\alpha > 1$) then $T_m(r)$ decreases as r increases. This is normally the case for nanowires where atoms at a boundary move easily because of their low coordination. The problem with this model is that one cannot determine the mean squared displacement around the melting temperature since diffusion dominates at that moment and the mean squared displacement is time

dependent. Nevertheless, we did an exponential fit with our data. The value of r_o was set to 5 Å for both nanowires. The fitting for these nanowires is reported by Figure 5.12 (bottom panel). The value of α was found to be 1.388 and 1.313, respectively for nanowires in (111) and (110) direction. Also, the bulk melting temperature was found to be 1753 K and 1767 K for nanowires in the (110) and (111) direction. These values are still high. Looking at Figure 5.12, we see that the two models look the same and could both be legitimate fit.

5.10 Conclusion

We computed the melting temperature of silicon nanowires in the [110] and [111] directions using the Stillinger-Weber potential. We confirmed that the melting temperature increases with nanowire diameter. The increase shows a good linear relation with the inverse of the nanowire diameter. The coefficients of the least squared fit are closer to those obtained for other metallic nanowire simulations. An exponential fit was also tried but it looks like the linear fit. This shows that the two models are both valid. It also was found that nanowires in the [111] direction have a melting temperature lower than their counterparts in the [110] direction and a good linear fit that the (110) nanowires. During the melting process, we observed a jump in the average potential energy per atom. The increase is fast in the beginning and plateaus at temperatures near the bulk melting temperature. As in the bulk, this increase is due to the increase in the three-body term and a decrease in the two-body term. The increase in the potential energy was first a result of a change in the nearest neighbors distance and coordination number and thus decreasing the two-body potential energy. Moreover, a spread in the angular distribution increased the three-body term. At the same time, we saw an increase an the self-diffusion coefficients. At melting, the atomic density becomes uniform with no breaking of nanowire as is sometimes reported. Therefore, melting starts at the surface and quickly spreads inside the

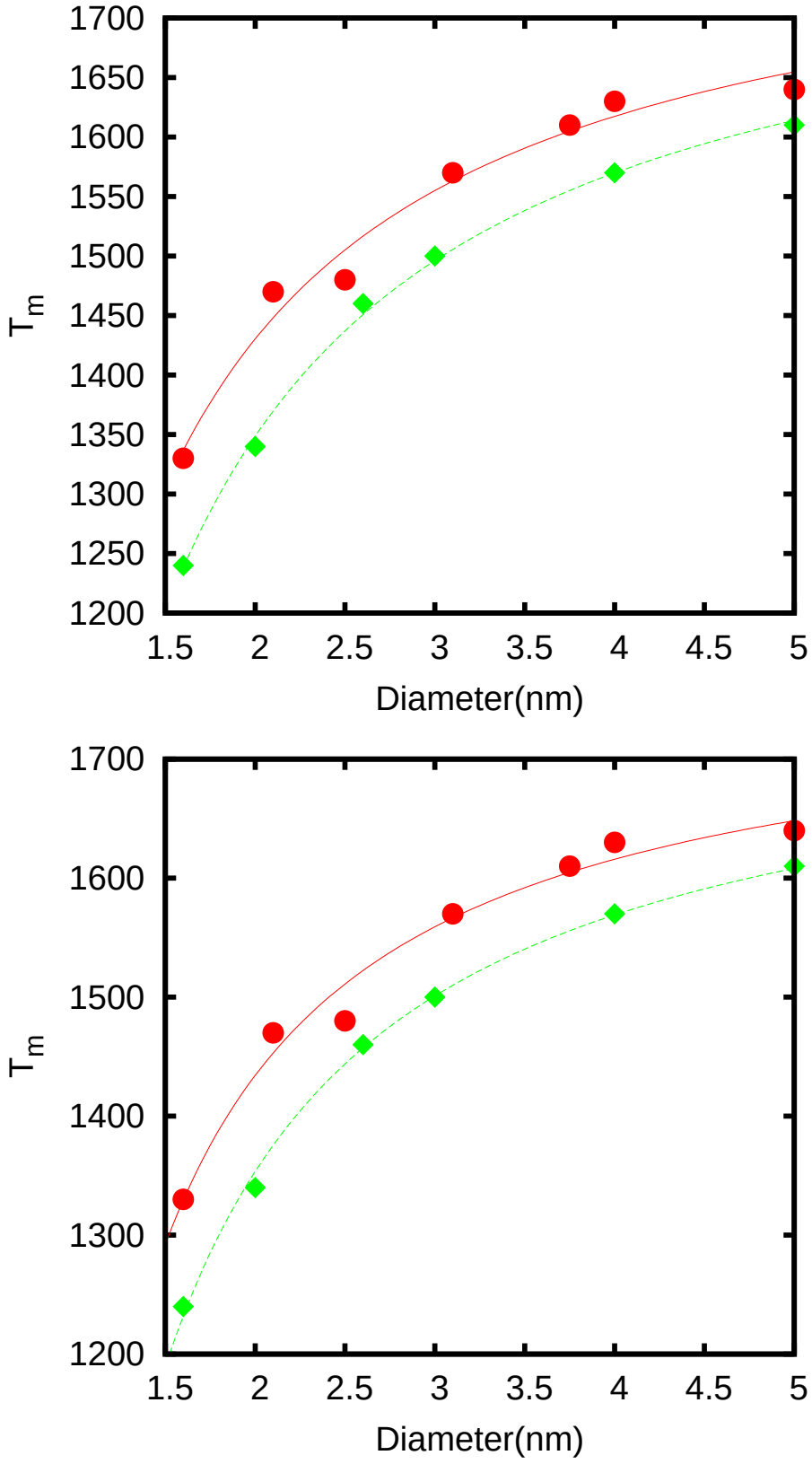

Figure 5.12: Melting temperature of silicon nanowire fitted to the inverse of the diameter (top panel) or with an exponential function (bottom panel). For each panel, the curve with circles is for the [110] direction while the one with diamonds is for the (111) direction.

nanowire in an asymmetric fashion. Before melting, atoms at the surface diffuse in the nanowire direction thus erasing atomic layers.

CHAPTER VI

SUMMARY

In this dissertation, many nanowires properties are investigated. First, we computed the electronic properties of germanium nanowires. The emphasis is in computing the size dependence and the orientation dependence of the bandgap. We used the density functional theory in the local density approximation (LDA). Since LDA undurestimates the band gap, we did a GW correction for the smallest nanowires in the [110] direction. The bulk band gap was found to be 0.1 eV. After including the GW correction, the band gap became 0.71 eV, which is close to the experimental value of 0.74 eV. Finally, we computed the band gap of nanowires with diameters between 1.1 nm to 4.4 nm. We concluded that the nanowires band gaps decrease with diameter. Nanowires with the [110] orientation have a lower band gap than those with of equal diameter but in the [111] orientation. The relationship between the band gap and the diameter was approximated best by a power function $E_g = E_b d^{-\alpha}$ where E_b is the bulk band gap. For both nanowire orientations, a value of 1.2 for α was found. Looking at the GW correction, it is worth mentionning that the correction is highly diameter dependent. We also calculated the susceptibility of the three smallest nanowires in each orientation. As expected, the peaks shift to higher energies as the diameter decreases.

We have studied the piezoelectric effect in wurtzite nanowires. In particular, we became interested in AlN and ZnO nanowires with the [001] orientation as found in experiments. Because of the cost of such a computation, we dealt only with nanowires of diameters between 0.4 nm and 0.7 nm. We used the Berry phase method and the density functional theory in the LDA approximation. We first computed the

band gap of the nanowires, both passivated and unpassivated. Both were found to be semiconducting. It was clear from the electronic calculation, that the unpassivated nanowires have surface states in the gap, making their band gap smaller than the passivated ones. While computing the piezoelectric coefficients for the bulk, we found values very close to the experimental results. This gave us the confidence to compute coefficients for nanowires. We found that passivated nanowires have lower piezoelectric coefficients than the bulk coefficients, while the unpassivated nanowire coefficients have higher than the bulk value. It is found that the difference is due to the electronic contribution and not the ionic contribution. Moreover, the sign of the electronic contribution or the ionic contribution never changed from bulk to passivated or unpassivated nanowires. Finally, we tested the effect of the piezoelectric field on the optical properties. In particular, it was known that when bulk ZnO (or other wurtzite materials) is compressed the imaginary part of the dielectric function shifts a little bit to higher energies. When calculations were made for passivated and unpassivated nanowires, we found that either shifts go to higher or lower energies depending on the frequencies.

The last part of this thesis studied the melting of silicon nanowires. We used the Stillinger-Weber classical potential in order to reduce the computation cost. We chose nanowires in the [110] and [111] orientations as it was the case for germanium nanowires. Before the melting calculation, we ran an annealing process, so as to get a lower energy structure. We computed the potential energy per atom and the temperature at which the discontinuity happened was set as the melting temperature. Other quantities were also obtained, such as the self-diffusion coefficients, the coordination number, etc., hence confirming the phase transition. We found that the liquid phase is dominated by a coordination number of $five$. In order to gauge whether there was a breaking of nanowires, we computed the particle density and found that the nanowire melt without breaking. By looking at the particles trajectories, we found

that nanowires melt from outside to inside. Finally, we investigated the size and the orientation depedence of the melting temperature. Looking at the results, we found that the melting temperature of nanowires in the [110] orientation was higher than those in the [110] orientation. We tried fitting models like $T_m = T_\infty - \delta/d$ and $T_m = T_m(\infty)Exp[-(\alpha-1)/(r/r_0-1)]$ where r_0 is the radius of the smallest nanowire in wich all atoms are at the boundary. We found that both models show a good correlation. The bulk melting temperature extrapolated from the data is between 1750K to 1800K, a little bit above the 1687K experimental value.

It is demonstrated that computation can find many properties of nanowires. Some of the computed properties are confirmed by experiments while others are yet to be measured. More properties will be computed with more accurate methods.

REFERENCES

[1] *2005 International technology Readmap for semiconductors. 2005 Edition* available online at http://www.itrs.net/

[2] W. Lu and C. M. Lieber, *J. Phys. D: Appl. Phys.* **39**, R387 (2006)

[3] Y. Li, Q. Fang, and C. M. Lieber, *Material Today* **9**, 18 (2006)

[4] Y. Wu, Y. Cui, L. Huynh, C. J. Barrelet, C. Bell, and C. M. Lieber, *Nano Letter* **4**, 433 (2004)

[5] Y. Cui, X. Duan, J. Hu, and C. M. Lieber, *J. Phys. Chem. B* **104**, 5213 (20000)

[6] A. B. Greytek, L. J. Lauhon, M. S. Gudiksen, and C. M. Lieber, *Appl. Phys. Lett.* **84**, 4176 (2004)

[7] Y. Huang, X. Duan, Y. Cui, and C. M. Lieber, *Nano Letter* **2**, 101 (2002)

[8] H. Lu, J. Li, R. A. Loomis, L. M. Wang, and W. E Buhro, *Nat. Mater.* 2, 517 (2003)

[9] J. Schiotz and K. W. Jacobsen, *Science* 301, 1357 (2003)

[10] Y. Wu and P. Yang, *Adv. Mater.* **13**, 520 (2001)

[11] G. Grosso, G. P. Parravicini, *Solid State Physics*, Academic Press (1999)

[12] R. G. Parr and W. Yang, *Density-Functional Theory of Atoms and Molecules*, Oxford Science Publications (1989)

[13] P. Hohenberg, and W. Kohn, *Phys. Rev.* **136**, B864, (19 64).

[14] A. P. Sutton, *Electronic Structure of materials*, Oxford Science Publications (1993)

[15] P. Perdew and W. Yue, *Phys. Rev. B* **33**, 8800 (1986)

[16] C . Pisani , *Quantum-Mechanical Ab-Initio Calculation of the Properties of Crystalline Materials* , Springer (1994)

[17] R. R. Martin, *Electronic Structure, basic theory and practical methods*, Cambridge University Press (2004)

[18] R. D. King-Smith and D. Vanderbilt, *Phys. Rev. B* **47**, 1651 (1993)

[19] R. Resta, *Rev. Mod. Phys.* **66**, 899 (1994)

[20] R. Resta, *Berry Phase in Electronic Wavefunction*, (Lecture Notes) 1999

[21] D. Vanderbilt, *Phys. Rev. B* **41**, 7892 (1990).

[22] P. E. Blöchl, *Phys. Rev. B* **50**, 17953 (1994)

[23] N. Troullier, and J. L. Martins, *Phys. Rev. B* **43**, 1993 (1991).

[24] M. C. Payne, M. P. Teter, D. C. Allan, T. A. Arias and J. D. Joannopouos, *Rev. Mod. Phys.* **64**, 1045 (1992)

[25] M. P. Allen and D. J. Tildesley, *Computer Simulation of Liquid*, Clarendon press (1987)

[26] J. E Lennard-Jones, *Proc. Camb. Phil. Soc.* **27**, 469 (1931)

[27] F. H. Stillinger and T. Weber, *Phys. Rev. B* **31**, 5262 (1985)

[28] J. Tersoff, *Phys. Rev. B* **37**, 6991 (1988).

[29] I. Ponomareva, D. Srivastava and M. Menon, *Nano Letters* **7**, 1155 (2007)

[30] L. Verlet, *Phys. Rev.* **159**, 98 (1967)

[31] L. Verlet, *Phys. Rev.* **165**, 201 (1967)

[32] D. Beeman, *J. Comp. Phys.***20**, 130 (1976)

[33] G. W. Gear, *Numerical Initial value problems in ordinary differential equations*, Prentice-Hall, Englewook Cliffs, USA (1971)

[34] J. Grotendorst, D. Marx, A. Muramatsu (Eds.), *Quantum Simulations of Complex Many-Body Systems: From Theory to Algorithms*, Lecture Notes, John von Neumann Institute for Computing, Julich, NIC Series, **10**, 211-254, (2002).

[35] H. Ch. Weissker, J. Furthmüller, and F. Bechstedt, *Phys. Rev. B* **65**, 155327 (2002).

[36] D. Erts, B. Polyakov, B. Daly, M. A. Morris, S. Ellingboes, J. Boland, J. D Holmes, *J. Phys. Chem. B* **110**, 820 (2006)

[37] L. Pizzagalli, G. Giulia, J. E. Klepeis, and F. Gygi, *Phys. Rev. B* **63**, 165324 (2001).

[38] T. V. Torchynska, G. Polupan, J. P. Gomez and A.V. Kolobov, *Microelectronics Journal* **34**, 541 (2003).

[39] Andrew B. Greytak, L. J. Lauhon, M. S. Gudisken, and L. M. Lieber, *Appl. Phys. Lett.* **84**, 4176 (2004).

[40] D. Wang, Q. Wang, A. Javey, R. Tu, H. Dai, H. Kim, P.C. McIntyre, T. Krishnamohan, and K. C. Saraswat, *Appl. Phys. Lett.* **83**, 2432 (2003).

[41] A. M. Morales and C. M. Lieber, *Science* **279**, 208 (1998).

[42] G. Gu, M. Burghard, G. T. Kim, G. S Düsberg, P. W. Chiu and V. Krstic, *J. Appl. Phys.* **90**, 5747 (2001).

[43] X. Wu and Y. Tao, *Material Research Bulletin* **37**, 2179 (2002).

[44] A. N. Kholod, V. L. Shaposhnikov, N. Sobolev, V. E. Borisenko, F. A. D'Avitaya, and S. Ossivini, *Phys. Rev. B* **70**, 035317 (2004).

[45] M. Bruno, M. Palummo, A. Marini, R. D. Sole, V. Olevano, A. N. Kholod and S. Ossicini, *Phys. Rev. B* **72**,153310 (2005).

[46] T. Muller, K. H. Heinig and B. Schmidth, *Nucl. Instrum. Methods Phys. Res. B* **175-177**, 468 (2001).

[47] X. Zhao, C. M. Wei, L. Yang, and M. Y. Chou, *Phys. Rev. Lett.* **92**, 236805 (2004).

[48] D. Vanderbilt, *Phys. Rev. B* **41**, 7892 (1990).

[49] G. Kresse and D. Joubert, *Phys. Rev. B* **59**, 1758 (1999).

[50] N. Troullier and J. L. Martins, *Phys. Rev. B* **43**, 1993 (1991).

[51] H. J. Xiang, J. Yang, J. G. Hou and Q. Zhu, *Appl. Phys. Lett.* **89**, 223111 (2006)

[52] H. J. Fan, W. Lee, M. Alexe, R. Scholz, K. Nielsch, M. Zacharias, R. Hauschild, H. Kalt, A. Dadgar and A. Krosti, *Small* **2**, 561, (2006)

[53] D. A. Scrmygenour, *J. Appl. Phys* **101**, 014316 (2007)

[54] F. Liu, P. J. Cao, H. R. Zhang, C. M. Shen, Z. Wang, J. Q. Li and H. J. Gao , *Journal of Crystal Growth* **274**, 126 (2005).

[55] J. Park, H. Choi, K. Siebein and R. K. Singh, *Journal of Crystal Growth* **258**, 342 (2003).

[56] Y. Zhang, J. Liu, R. He, Q. Zhang, X. Zhang, and J. Zhu, *Chem. Mater.* **13**, 3899 (2001)

[57] R. D. King-Smith and D. Vanderbilt, *Phys. Rev. B* **47**, 1651 (1993)

[58] R. Resta, *Rev. Mod. Phys.* **66**, 899 (1994)

[59] G. Kresse, J. Hafner, *Phys. Rev. B* **48**, 115 (1993)

[60] P. Schröer, P. Krüger, and J. Pollmann , *Phys. Rev. B* **47**, 6971 (1993)

[61] W. Y. Ching, B. N. Harmon, *Phys. Rev. B* **34**, 5305 (1986)

[62] A. Filippetti ,V. Fiorentini,G. Cappellini and A. Bosin, *Phys. Rev. B.* **59**, 8026 (1999).

[63] F. Decremps, F. Datchi, A. M. Saitta, A. Polian, S. Pascarelli, A. Di Cicco, J. P. Iti and F. Baudelet, *Phys. Rev. B.* **68**, 104101 (2003)

[64] F. Bernardini, V. Fiorentini and D. Vanderbilt, *Phys. Rev. B* **63**, 193201 (2001)

[65] D. J. Cooke, A. Marmier and S. C. Parker, *J. Phys. Chem. B*, **110**, 7985, (2006)

[66] B. Meyer and D. Marx *Phys. Rev. B* **67**, 035403 (2003).

[67] J. G. Gualtieri, J. A. Kosinski and A. Ballato, *IEEE trans. ultra. Ferroelectr. Freq. Control* **41**, 53 (1994)

[68] S. W. Lepkowski and J. A. Majewski, *Mat. Res. Soc. symposium procedings*, **831**, 653 (2004)

[69] D. Zhang and R. Q. Zhang, *Chem. Phys. Lett.* **371**, 426 (2003).

[70] K. Doi, N. Higashimaki, Y. Kawakami, K. Nakamura and A. Tachibana, *Physica Status Solidi B* **241**, 2806 (2004)

[71] V. N. Tondare, C. Balasubramanian, S. V. Shende, D. S. Joag, V. P. Godbole, S. V. Bhoraskar and M. Bhadbhade, *Appl. Phys. Lett.* **80**, 4813 (2002)

[72] R. Rurali, *Phys. Rev. B*, **71**, 205405 (2005)

[73] R. Rurali and N. Lorente, *Phys. Rev. Lett* **94**, 026805 (2005)

[74] T. M. Parker, N. G. Condon, R. Lindsay, F. M. Leibsle, G. Thornton, *Surface Science* **415**, L1046 (1998).

[75] A. Wander and N. M. Harrison, *Surf. Sc.* **457**, L.342 (2000).

[76] R. Pandey and P. Zapol, *Phys. Rev. B* **55**, R16009 (1997)

[77] F. Bernardini, V. Fiorentini *Phys. Rev. B* **56**, R10024 (1997)

[78] J. A. Christman, R. R. Woolcott jr, A. I. Kingon,R. J. Namanich, *Appl. Phys. Lett.* **73**, 3851 (1998)

[79] M. H. Zhao, Z.L. Wang and S.X. Mao *Nano. Lett.* **4**, 587 (2004)

[80] J. Sun, H. Wang, J. He and Y. Tian, *Phys. Rev. B* **71**, 125132 (2005)

[81] G. Chen and A. Shakouri, *Journal of Heat Transfer*, **124**, 242 (2002)

[82] X. Y. Zhang, X. Zhao, C. W. Lai, J. Wang, X. G. Tang, and J. Y. Dai, *Appl. Phys. Lett.* **85**, 4196 (2004)

[83] Y. Wen, Z. Zhu, R. Zhu and G. Shao, *Physica E* **25**, 47 (2004)

[84] L. Miao, V. R. Bhethanabotha and B. Joseph, *Phys. Rev. B* **72**, 134109 (2005)

[85] W. H. Moon, H. J. Kim, and C. H. Choi, *Scripta Materialia* **56**, 345 (2007)

[86] L. Hui, F. Pederiva, B. L. Wang, J. L. Wang and G. H. Wang, *Appl. Phys. Lett.* **86**, 011913 (2005)

[87] L. Hui, B. L. Wang, J. L. Wang and G. H. Wang, *J. Chem. Phys.* **120**, 3431 (2004)

[88] S. H. Yang, and R. J. Berry, *Mat. Res.Soc. Symp. Proc.* **769**, H6.15 (2003)

[89] I. Ponomareva, M. Menon, D. Srivastava, and A. N. Andriotis, *Phys. Rev. Lett.* **95**, 265502 (2005)

[90] K. Fang, and C. Weng, *Nanotechnology* **16**, 250 (2005)

[91] F. H. Stillinger and T. Weber, *Phys. Rev. B* **31**, 5262 (1985)

[92] Y. Zhou, M. Karplus, K. D. Ball and R. S. Berry, *J. Chem. Phys.* **116**, 2323 (2002)

[93] E. Blaisten-Barojas, and D. Levesque, *Phys. Rev. B* **34**, 3910 (1986)

[94] W. D. Luedtke and U. Landman, *Phys. Rev. B* **37**, 4656 (1988)

[95] A. P. Horsfield and P. Clancy, *Mod. Simul. Mater. Sci. Eng. 2*, **2**, 277 (1994)

[96] O. Sugino and R. Car, *Phys. Rev. B* **74**, 1823 (1995)

[97] J. Q. Broughton and X. P. Li *Phys. Rev. B* **35**, 9120 (1987)

[98] F. F. Abraham and J. Q. Broughton, *Phys. Rev. lett* **56**,734 (1986)

[99] P. C. L. Stephenson, M. W. Radny and P. V, Smith, *Surf. Sci.* **366**, 177 (1996)

[100] O. Gülseren, F. Ercolessi and E. Tosatti, *Phys. Rev. lett.* **80**, 3775 (1998)

[101] M. Menon, D. Srivatava, I. Ponomareva and L. A. Chernozatonskii, *Phys. Rev. B* **70**, 125313 (2004)

[102] C. S. Moura, L. Amaral, *Nuclear Instruments and Methods in Physics Research B* **228**, 37 (2005)

[103] L. Nurminem, F. Tavazza, D. P. Landau, A. Kuronen and K. Kaski, *Phys. Rev. B* **67**, 035405 (2003)

[104] X. P. Xie, M. H. Liang, Z. M. Choo and S. Li, *Surf. Rev. Lett.* **8**, 471 (2001)

[105] S. Yoo, X. C Zeng and J. R. Morris, *J. Chem. Phys.* **120**, 1654 (2004)

[106] Z. Zhang, J. C. Li and Q. Jiang, *J. Phys. D: Appl. Phys.* **33**, 2653 (2000)

VITA

Alexis Nduwimana was born in Burundi on April 20, 1970. He received his B.S in 1997 from the University of Bujumbura. He recieved his M.S in Physics from Clark Atlanta University in 2001 and came to Georgia Institute of Technology in September 2001.